

EXPLORATION OF INTERFACIAL THERMAL CONDUCTANCE OF GOLD  
NANOPARTICLES USING MOLECULAR DYNAMICS

A Dissertation

Submitted to the Graduate School  
of the University of Notre Dame  
in Partial Fulfillment of the Requirements  
for the Degree of

Doctor of Philosophy

by  
Suzanne M. Neidhart

---

J. Daniel Gezelter, Director

Graduate Program in Chemistry and Biochemistry

Notre Dame, Indiana

November 2018

EXPLORATION OF INTERFACIAL THERMAL CONDUCTANCE OF GOLD  
NANOPARTICLES USING MOLECULAR DYNAMICS

Abstract

by

Suzanne M. Neidhart

In this dissertation I present work on elucidating factors important to heat transport in gold nanostructures, particularly nanoparticles, examining the effect of particle size, ligand layer rigidity, and surface gold vibrational freedom. The interfacial thermal conductance of various particles, as well as the thermal conductivity of nanoarrays that are of interest to see trends in heat transport. Direct simulations of interfacial thermal conductance of solvated gold nanoparticles using molecular dynamics were calculated. All particle simulations used the Langevin Hull method for non-periodic systems.

Experimental nanoparticles contain a moiety, or ligand layer, at the surface of each particle that prevents aggregation and is a result of the method used in the formation of the particles. This moiety is essential in controlling movement of heat from a particle to the surrounding media. In particular, the following study looks closely at how the rigidity of this ligand layer and the length of the ligand change thermal transport at the interface of the particle. This allows for further insight into the important factors for ligand and solvent interactions to optimize heat flow. Proposed mechanisms for heat transfer rely on two effects: the vibrational overlap of the materials at the interface and the density overlap of the same materials.

After finding no direct relationship for particle size with the ligand layer and the

thermal transport, a simpler system was examined: bare nanoparticles in solvent. The particles consist of nanospheres, icosahedra, and cuboctahedra. The latter two display facets that are common in many nanostructures due to their stability. The interfacial thermal conductivity ( $G$ ) of the particles was examined based on radius and particle type. The coordination of gold atoms at the particle surface, giving information about the vibrational freedom, displayed a slight correlation with  $G$ . This supports the proposed important factors for heat transport found in the ligand layer work.

Finally, the ideas from both prior works are combined to study  $Au_{144}PET_{60}$  particles in isolation and in an array. These small particles ( $r \approx 10 \text{ \AA}$ ) have highly undercoordinated gold atoms within the ligand layer. The thermal conductivity of the composite material is predicted using the Hasselman and Johnson equation using components of the material and compared to preliminary results for the simulated nanoarrays. In the predicted conductivity, the nanoarray thermal conductivity is highly dependent on the geometric feature,  $v_p$ , the particle volume fraction.

## CONTENTS

FIGURES . . . . .	iv
TABLES . . . . .	ix
CHAPTER 1: INTRODUCTION . . . . .	1
1.1 Heat Transport . . . . .	2
1.1.1 Heat Transfer at Interfaces . . . . .	3
1.1.2 Acoustic Mismatch Model . . . . .	3
1.1.3 Diffuse Mismatch Model . . . . .	5
1.2 Molecular Dynamics . . . . .	7
1.2.1 Representations of Atoms . . . . .	11
1.2.2 Boundary Conditions . . . . .	12
1.3 Transport Coefficients . . . . .	14
1.3.1 Equilibrium Molecular Dynamics . . . . .	17
1.3.2 Non-Equilibrium Molecular Dynamics . . . . .	19
1.3.3 Reverse Non-Equilibrium Molecular Dynamics . . . . .	19
1.4 Systems of Interest . . . . .	20
CHAPTER 2: INTERFACIAL THERMAL CONDUCTANCE OF THIOLATE-PROTECTED GOLD NANOSPHERES . . . . .	22
2.1 Introduction . . . . .	22
2.2 Interfacial Thermal Conductance of Metallic Nanoparticles . . . . .	24
2.2.1 Structures of Self-Assembled Monolayers on Nanoparticles . . . . .	24
2.3 Computational Details . . . . .	25
2.3.1 Creating a thermal flux between particles and solvent . . . . .	25
2.3.2 Interfacial Thermal Conductance . . . . .	28
2.3.3 Force Fields . . . . .	28
2.3.4 Simulation Protocol . . . . .	35
2.4 Results . . . . .	38
2.4.1 Corrugation of the Particle Surface . . . . .	40
2.4.2 Orientation of Ligand Chains . . . . .	44
2.4.3 Orientation of Interfacial Solvent . . . . .	46
2.4.4 Solvent Penetration of Ligand Layer . . . . .	48
2.4.5 Ligand-mediated Vibrational Overlap . . . . .	51
2.5 Discussion . . . . .	52

CHAPTER 3: THERMAL TRANSPORT IS INFLUENCE BY NANOPARTICLE SHAPE . . . . .	55
3.1 Introduction . . . . .	55
3.1.1 Size- and temperature-dependent particle morphologies . . . . .	57
3.1.2 Theory . . . . .	57
3.2 Computational Details . . . . .	60
3.2.1 System Composition . . . . .	60
3.2.2 Force Fields . . . . .	60
3.2.3 Simulation Protocol . . . . .	64
3.3 Results and Discussion . . . . .	65
3.3.1 Hexane Density . . . . .	67
3.3.2 Surface Atom Undercoordination . . . . .	67
3.3.3 Phonon Spectra . . . . .	75
3.3.4 A Brief Aside on Local Orientational Ordering . . . . .	76
3.3.5 A Simple Model for Bare Nanoparticle Conductance . . . . .	81
3.4 Conclusions . . . . .	83
 CHAPTER 4: A PREDICTION OF THE THERMAL CONDUCTIVITY OF Au <sub>144</sub> PET <sub>60</sub> NANOARRAYS . . . . .	86
4.1 Introduction . . . . .	86
4.1.1 Theory . . . . .	88
4.2 Computational Details . . . . .	89
4.2.1 Force Fields . . . . .	89
4.2.2 Simulation Protocol . . . . .	93
4.2.3 Calculating thermal conductivity . . . . .	100
4.3 Results and Discussion . . . . .	102
4.3.1 Bulk Solvent and Bulk Gold Conductivity . . . . .	102
4.3.2 Interfacial Thermal Conductivity . . . . .	105
4.3.3 Prediction of Array Thermal Conductivity . . . . .	105
4.3.4 Simulations of Array . . . . .	106
4.4 Conclusions . . . . .	107
 CHAPTER 5: CONCLUSION . . . . .	108
 BIBLIOGRAPHY . . . . .	111

## FIGURES

- |     |   |    |
|-----|---|----|
| 1.1 | Here an incoming phonon in material A is approaching the interface of materials A and B. The wave has a polarization ( $p$ ) and frequency ( $\omega$ ) and approaches the interface at an angle ( $\theta$ ) relative to the normal of the interface. The phonon, under the DMM, has two options at the interface: scatter through to material B or scatter back through material A. The probability of transmission is given by $\tau_{ab}$ . Due to detailed balance, the scattering back to material A is $1 - \tau_{ab}$ . . . . . | 4  |
| 1.2 | The initial positions, $r$ , and velocities, $v$ , are established in a system and from the potential energy, forces on the atoms is found. From the forces, positions can be changed then the velocities can be updated. The time can be moved forward and the process repeated at the calculated forces step until the desired time is reached. . . . .   | 8  |
| 1.3 | This figure is an example of periodic boundaries in two dimensions. Here the middle cell (colored square) is the system and each surrounding cell is an ‘image’ of the original. As can be seen in the relation between particle A and C, sometimes the image particle provides the closest interaction or minimum image and would be within the cutoff radius when calculating interactions. . . . .   | 13 |
| 1.4 | Visualization of a gold particle solvated in water within the Langevin Hull taken from Vardeman <i>et. al.</i> [1]. The temperature and pressure bath interact with only the outer most atoms on the hull, the grey translucent surface. At each time step the hull is computed to ensure the atoms are interacting in the correct classifications, as edge atoms or as interior atoms. . . . .   | 15 |
| 2.1 | Topologies of the thiolate capping agents and solvent utilized in the simulations. The chemically-distinct sites (S, $\text{CH}_2$ , $\text{CH}_3$ , CHe, CHa and $\text{CH}_2$ a) are treated as united atoms. Most parameters are taken from references [2], [3] [4]. Cross-interactions with the Au atoms were adapted from references [5], [6], and [7]. . . . .  | 26 |
| 2.2 | A 25 Å radius gold nanoparticle protected with a half-monolayer of TraPPE-UA dodecanethiolate ( $\text{C}_{12}$ ) ligands and solvated in TraPPE-UA hexane. The interfacial thermal conductance is computed by applying a kinetic energy flux between the nanoparticle and an outer shell of solvent. . . . .   | 36 |

2.3	Radial temperature profile for a 25 Å radius particle protected with a 50% coverage of TraPPE-UA butanethiolate ( $C_4$ ) ligands and solvated in TraPPE-UA hexane. A kinetic energy flux is applied between RNEMD region A and RNEMD region B. The size of the temperature discontinuity at the interface is governed by the interfacial thermal conductance. . . . .	37
2.4	Interfacial thermal conductance ( $G$ ) values for 4 sizes of solvated nanoparticles that are bare or protected with a 50% coverage of $C_4$ , $C_8$ , or $C_{12}$ thiolate ligands. Ligands of different flexibility are shown in separate panels. The middle panel indicates ligands which have a single carbon-carbon double bond in the penultimate position. . . . .	39
2.5	Fraction of gold atoms with fcc ordering as a function of radius for a 10 Å radius nanoparticle. The decreased fraction of fcc-ordered atoms in ligand-protected nanoparticles relative to bare particles indicates restructuring of the nanoparticle surface by the thiolate sulfur atoms. . . . .	42
2.6	Computed corrugation values for 4 sizes of solvated nanoparticles that are bare or protected with a 50% coverage of $C_4$ , $C_8$ , or $C_{12}$ thiolate ligands. The smallest (10 Å) particles show significant disruption to their crystal structures, and the length and stiffness of the ligands is a contributing factor to the surface disruption. . . . .	43
2.7	The two extreme cases of ligand orientation relative to the nanoparticle surface: the ligand completely outstretched ( $\cos(\theta) = -1$ ) and the ligand fully lying down on the particle surface ( $\cos(\theta) = 0$ ). . . . .	45
2.8	Computed ligand and interfacial solvent orientational $P_2$ values for 4 sizes of solvated nanoparticles that are bare or protected with a 50% coverage of $C_4$ , $C_8$ , or $C_{12}$ alkanethiolate ligands. Increasing stiffness of the ligand orients these molecules normal to the particle surface, while the length of the ligand chains works to prevent solvent from lying flat on the surface. . . . .	47
2.9	Radial density profiles for 25 Å radius nanoparticles with no ligands (circles), $C_4$ ligands (squares), $C_8$ ligands (diamonds), and $C_{12}$ ligands (triangles). Ligand density is indicated with filled symbols, solvent (hexane) density is indicated with open symbols. As ligand chain length increases, the nearby solvent is excluded from the ligand layer. The conjugated ligands (upper panel) can create a separated solvent shell within the ligand layer and also allow significantly more solvent to penetrate close to the particle. . . . .	49
2.10	Density overlap parameters ( $O_{l-s}$ ) for solvated nanoparticles protected by thiolate ligands. In general, the rigidity of the fully-conjugated ligands provides the easiest route for solvent to enter the interfacial region. Additionally, shorter chains allow a greater degree of solvent penetration of the ligand layer. . . . .	50

2.11 The low frequency portion of the vibrational density of states for three chemical components (gold nanoparticles, C <sub>12</sub> ligands, and hexane solvent). These densities of states were computed using the velocity autocorrelation functions for atoms in the interfacial region, constructed with velocities projected onto a direction normal to the interface. . . . .	53
3.1 Interfacial thermal conductance, $G$ , for bare gold nanospheres, cuboctahedra, and icosahedra in contact with hexane solvent. Conductances for flat Au(111), Au(100), and Au(110) interfaces are indicated with dashed horizontal lines. A fit using the model of Tascini <i>et al.</i> is shown along with the predicted value of $G(\infty)$ , the infinite particle limit. . . . .	66
3.2 Hexane density as a function of distance from the interfacial gold for the (111), (110), and (100) facets. The solvent in the (111) and (100) systems display nearly identical density profiles. Because the lowest-coordinated gold atoms on the (110) facet have a relatively low surface density, the hexane molecules are able to get closer to these undercoordinated atoms. . . . .	68
3.3 Locations of undercoordinated atoms on common gold facets. The dark gold atoms indicate atoms of a particular coordination number, cyan atoms denote the first nearest neighbors of these atoms, and the partially transparent lattice illustrates the location of the atoms in the larger gold structure. (111) surfaces (lower left) display atoms with CN=9, while (100) surfaces (upper left) display atoms with CN=8, and (110) surfaces present surface atoms with CN=7 and buried atoms with CN=11. . . . .	71
3.4 The normalized low frequency density of states (DOS) of the surface atoms with the coordination number of 6, 7, 8, 9 and 11, corresponding to the vertices of the icosahedra, Au(110), Au(100), Au(111) and sub-surface Au(110), respectively. Note that CN=11 atoms near a surface are found adjacent to atoms with lower coordination (e.g. CN=7), so the high frequency peak at 138 cm <sup>-1</sup> is present for both CN=11 and CN=7. Low frequency contributions at $\sim 70$ cm <sup>-1</sup> are enhanced for surface atoms with CN=7, 8, and 9. . . . .	73
3.5 The coordination number of surface atoms as a function of particle size. Filled data points are sampled from simulations, while the dashed lines correspond to ideal icosahedral and cuboctahedral solids. In the spherical case, the large radius limits are shown with open symbols. The large radius limit for the spheres approaches a constant density for all undercoordinated sites, while for the icosahedra, the 9-coordinated (111) facet dominates. In larger cuboctahedra, the relative fraction of 8- and 9-coordinated surface atoms is largely independent of particle size. . . . .	74

3.6	The fraction of FCC-like local environments as a function of radius from the center of 40 Å nanoparticles. The spheres and cuboctahedra are originally cut from a FCC lattice, so the local ordering persists even close to the surface. Icosahedra are constructed as shells surrounding a perfectly icosahedral central core of 13 atoms. Non-FCC ordering persists throughout these simulations. . . . .	78
3.7	The projected vibrational density of states (Eq. 3.4) for individual layers in the largest gold nanoparticles (top: spheres, middle: icosahedra, bottom: cuboctahedra). In all systems, the surface layer (green) is significantly enhanced at low frequencies and is shifted down by $\sim 20 \text{ cm}^{-1}$ . The Au (bulk) curve shown for comparison is from a perfect FCC lattice in periodic boundary conditions. . . . .	79
3.8	The projected vibrational density of states for all gold atoms (top panel) shows that the phonons in FCC-like nanoparticles (spheres, cuboctahedra) have similar frequency representation, while the non-FCC structures (icosahedra) have significantly altered “bulk” spectra. For surface atoms (bottom panel), the differences in surface undercoordination appear at higher frequencies. These spectra were computed for the largest particles in each of the different morphologies. . . . .	80
3.9	The normalized low frequency density of states (DOS) of the interfacial solvent and the gold particle for the icosahedral and spherical systems. . . . .	82
3.10	Structurally-predicted thermal conductance values from Eq. (3.18) compared with the simulated thermal conductance values. Error bars indicate the standard error computed using five replica simulations. . . . .	84
4.1	A single $\text{Au}_{144}\text{PET}_{60}$ cluster with the icosahedral core atoms rendered as spheres. All atoms in the ligand staple motif are displayed as stick like structures for clarity of the particle structure. . . . .	90
4.2	The Au and S atoms in the staple motif are depicted with spheres, while the PET R groups are shown as stick like structures for clarity of the staple structure. The $\text{Au}_{\text{surf}}$ atoms sit directly on the icosahedral core of the nanocluster, while the $\text{Au}_{\text{lig}}$ atom is slightly out from the gold surface and bonded to the sulfur atoms in two PET ligands. . . . .	91
4.3	A single $\text{Au}_{144}\text{PET}_{60}$ cluster in a solvent cloud of dichloromethane. . . . .	96
4.4	This figure is an example of the thermal gradient that develops in a bulk solvent system with a moderate flux. The red region is the “hot” bin and the two blue regions are the “cold” bins. The slope, $m$ , that measures the temperature gradient is related to the thermal conductivity of the material, $\lambda$ . . . . .	101
4.5	Parameters to Eq. 4.4 for bulk simulations of dichloromethane (green circles), toluene (black squares), and liquid gold (yellow diamonds). The y-axis, $\lambda$ is in units of $\text{W}/\text{mK}$ . The x-axis, $L$ is in Å. . . . .	103



## TABLES

1.1	Constitutive and balance equations related to the transport coefficients of diffusivity, $D$ , thermal conductivity, $\lambda$ , and shear viscosity, $\eta$ . . . . .	16
2.1	Non-bonded interaction parameters (including cross interactions with Au atoms). . . . .	29
2.2	Bond parameters for the ligand molecules. . . . .	30
2.3	Bend angle parameters. The central atom in the bend is atom $j$ . . . . .	33
2.4	The central atoms for each torsion are atoms $j$ and $k$ , and wild-card atom types are denoted by “X”. All $c_n$ parameters have units of kcal/mol. The torsions around carbon-carbon double bonds are harmonic and assume a trans ( $180^\circ$ ) geometry. The force constant for this torsion is given in kcal mol $^{-1}$ degrees $^{-2}$ . . . . .	34
3.1	Composition of the solvated planar facet systems and the physical extent of the gold slabs ( $L_x$ , $L_y$ , and $L_z$ ). The hexane molecules occupy the remainder of a 100 Å box (length measured along the $z$ -axis). . . . .	61
3.2	Composition of the solvated nanosphere simulations. . . . .	61
3.3	Composition of the solvated icosahedral nanoparticle simulations. . . . .	62
3.4	Composition of the solvated cuboctahedral nanoparticle simulations. . . . .	63
3.5	Surface densities (Å $^{-2}$ ) of undercoordinated atoms in ideal geometries. $\ell$ (Å) is the lattice constant of the underlying FCC lattice. The spheres and cuboctahedra are calculated using a gold FCC lattice with $\ell = 4.08$ Å. For cuboctahedral particles, the radius ( $r$ ) is computed using Eq. (3.15). . . . .	69
3.6	The density of undercoordinated gold atoms at the surface of a facet. . . . .	75
3.7	Parameters of the Model in Eq. (3.18). . . . .	83
4.1	Composition of a single nanoparticle and non-bonded interactions parameters for the interaction with gold. . . . .	92
4.2	Harmonic bond parameters for different components in the simulated systems. The first part of the table are the atoms in the staple motif within the nanoparticle. The latter sections are the solvents: toluene and dichloromethane, respectively. . . . .	94

4.3	Bend angle parameters for a harmonic potential. The central atom in the bend is atom $j$ . The table is structured with the particle staple motif in the first section, followed by the solvents: toluene and dichloromethane. . . . .	95
4.4	Composition of the pure liquid simulations with box dimensions and average lambda values with standard error from 5 simulations. . . . .	98
4.5	Composition of solvated nanoparticles for interfacial thermal conductivity simulations. . . . .	99
4.6	Composition of nanoarray systems. . . . .	100
4.7	The Hasselman and Johnson prediction for thermal conductivity of the $\text{Au}_{144}\text{PET}_{60}$ array using the gold thermal conductivity at 1500 K and 300 K. The array prediction for dichloromethane and toluene using the bulk thermal conductivity of each solvent. . . . .	106

## CHAPTER 1

### INTRODUCTION

This chapter explores the basics of heat transfer and molecular dynamics. The challenges existing in the current methods of finding transport quantities using molecular dynamics are included. Finally, applications of molecular dynamics to finding thermal tranport in systems of interest are presented. The remaining chapters use the methods described here to examine systems of interest.

The first application, gold nanospheres of varying sizes and ligands, are presented in Chapter 2. There are three different variables to characterize these systems: particle size, ligand length, and ligand rigidity. Through looking at the vibrational density of states and the density profiles for the systems, two important factors for heat transport can be determined: the vibrational overlap of the material at the interface and the physical proximity/overlap of the material at the interface. This information gives relevant principles for ligand and particle design, while no clear trend for particle radius was established.

In an attempt to detangle the size and the ligand dependence, Chapter 3 takes a closer look at the particle surface and size dependence. The particles are left bare but have a range of sizes and three different geometries: spheres, icosahedra, and cuboctahedra. The three different morphologies give distinct vibrational spectra at the particle surface, allowing for different thermal conductivity. In addition to the particles, planar systems displaying the prominent facets of the particles were studied. This work suggests the need for a proximity factor contributing to a model of thermal transport. The vibrational overlap of the material at the interface matters, but so

does the amount of the material that is transferring heat. This is most clearly seen through the surface density of undercoordinated surface atoms in the planar systems.

Chapter 4 presents a combination of the concepts in the previous chapters through the study of small nanoparticles both in isolation and in a nanoarray. The  $\text{Au}_{144}\text{PET}_{60}$  particle are approximately 9 Å in radius and have a crystal structure found at very low temperatures which is an appropriate starting structure simulating heat transport in arrays. A unique aspect of these particles, and similar small structures, is that the ligand layer has gold atoms pulled away from the surface. This leads to lower coordination of the outer-most gold atoms, which now exhibit different vibrational spectra. These particles were simulated in two different solvents to observe solvent effects on the thermal conductivity of these particles.

Finally, Chapter 5 looks forward to potential applications of a new fluctuating charge embedded method to be applied to metal surfaces and particles in polarizable solvents. This new method would allow for the examination of charge effects on thermal transport and arrangement of solvent at the surface of the metal.

## 1.1 Heat Transport

The classical definition of temperature is a quantity that describes a thermal equilibration phenomena. At the macroscopic level, heat can be transferred in three ways: conduction, convection, and radiation. [8] Under the equipartition theorem, where the average kinetic energy of a particle is  $\frac{3k_B T}{2}$ , the temperature is a reporter of the kinetic energy of the system. [9] When the kinetic energy is distributed evenly among all independent parts of the system, the heavy atoms in a system would have a small average speed than the lighter atoms in the system.

On the microscopic level, heat moves through different paths depending on the composition of the system. [8] In a gas, heat is transferred primarily through collisions, while in semiconductors thermal energy moves through the propagation of vibrations

in the solid, ie. phonons. A phonon is a quantized lattice wave that traverses the material with a longitudinal or transverse polarization. [10] In metals, where the material has a solid lattice embedded in a sea of electrons, both phonon and electron heat transfer contribute. [10] Electrons in a metal system are typically treated as an electron gas. Electrons travel at velocities that are approximately three orders of magnitude larger than phonons, therefore the electron contribution dominates heat transfer in metals and is important when considering bulk thermal conductance of metals. At a metal/non-metal interface the thermal conductance through the non-metal is dominated by phonon scattering, rather than electronic contributions. [8, 11, 12]

### 1.1.1 Heat Transfer at Interfaces

Further examination of phonons as the only heat carriers can be done at the interface of two materials. If the phonon is traveling through material A and approaches material B with frequency  $\omega$ , with angles  $\phi$  and  $\theta$  normal to the interface; there is a transmission probability,  $\tau_{a \rightarrow b}(\omega)$ , that the wave will continue into material B (see Figure 1.1). [13] The transmission probability must satisfy detailed balance. There are two major models that make predictions for heat transfer at the interface: the acoustic mismatch model (AMM) and the diffuse mismatch model (DMM). [13]

### 1.1.2 Acoustic Mismatch Model

In the acoustic mismatch model, the transmission probability- the total fraction of energy transmitted across the interface- is dependent on the acoustic impedance of the material,  $Z_i$ . The AMM evaluates the transmission coefficient through a continuum approach. [14] This model uses the acoustic transmission and reflection between the two materials and ignores the granularity of the materials. Therefore the AMM would be most appropriate for low temperatures where the thermal spectrum is dominated

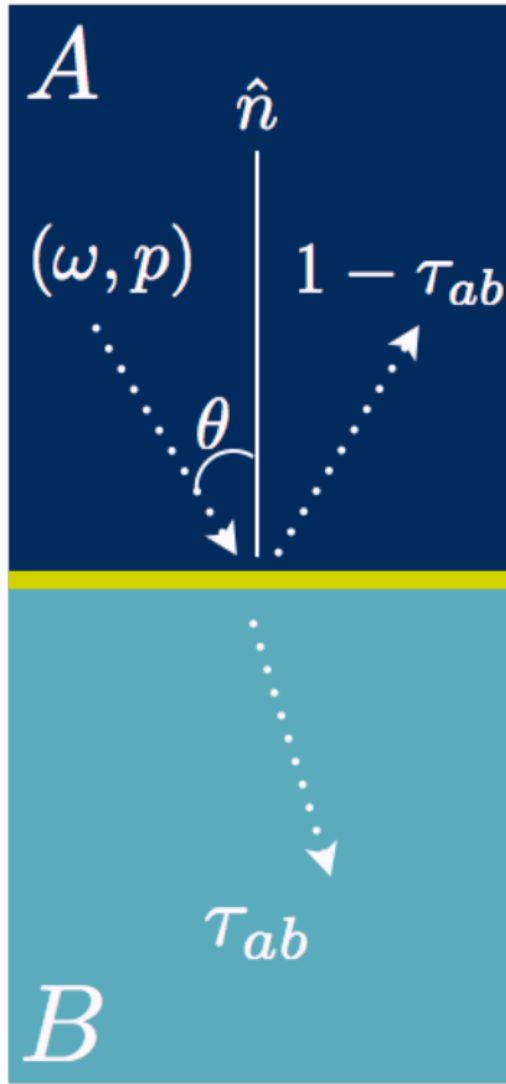


Figure 1.1. Here an incoming phonon in material A is approaching the interface of materials A and B. The wave has a polarization ( $p$ ) and frequency ( $\omega$ ) and approaches the interface at an angle ( $\theta$ ) relative to the normal of the interface. The phonon, under the DMM, has two options at the interface: scatter through to material B or scatter back through material A. The probability of transmission is given by  $\tau_{ab}$ . Due to detailed balance, the scattering back to material A is  $1 - \tau_{ab}$ .

by long wavelength phonons. [15]

Each transmitted phonon has three possible polarizations: one longitudinal and two transverse. Likewise, reflected phonons can be reflected in the same fashion, giving six different paths for a wave to interact with the interface. This problem is usually simplified using the acoustic analog of Snell's law where  $\theta$  is the angle relative to the normal of the interface and  $p$  is the polarization of the phonon:

$$\tau_{ab}(\theta, p) = \frac{4 \frac{p_2 \nu_{p,2}}{p_1 \nu_{p,1}} \frac{\cos \theta_{p,2}}{\cos \theta_{p,1}}}{\left( \frac{p_2 \nu_{p,2}}{p_1 \nu_{p,1}} + \frac{\cos \theta_{p,2}}{\cos \theta_{p,1}} \right)^2} \quad (1.1)$$

where  $\theta$  are related to the analog of Snell's law through the frequency:  $\frac{\sin \theta_1}{\nu_1} = \frac{\sin \theta_2}{\nu_2}$ .

Here  $\nu$  is the frequency of the phonon in each material.

Transmission can be simplified using acoustic impedances:

$$\tau_{ab}(\theta, p) = \frac{4 Z_a Z_b}{(Z_a + Z_b)^2} \quad (1.2)$$

where  $Z$  is the acoustic impedance of each material,  $Z_a = \rho_a v_a$ , which depends on,  $\rho$ , the density and  $v$ , the speed of sound in the material.

More complex treatments of the sound waves [16] and treatments accounting for the interfacial bonding [17] through the AMM have been studied. These modifications result in values that are lower than traditional AMM, therefore much below the experimental measurements of the systems. [12, 18]

### 1.1.3 Diffuse Mismatch Model

The diffuse mismatch model assumes that the phonon has two options when the wave meets the interface: the phonon can transfer into material B or be reflected back into material A (see Figure 1.1). It operates under the assumption that all phonons at the interface are scattered randomly, meaning that all memory of the direction

and polarization are lost. The phonon only keeps the frequency constant during the interaction of the two materials, hence all probability of the phonon to propagate into a material is dependent of the material's density of states.

Under the DMM, the thermal conductance at an interface between  $a$  and  $b$  can be approximated,

$$G_{ab} = \frac{1}{4\pi} \sum_p \int_{\omega} \int_{\theta} \int_{\phi} \hbar\omega \frac{\partial f}{\partial T} v_a \rho_a \tau_{ab} \cos \theta \sin \theta d\theta d\phi d\omega \quad (1.3)$$

where  $f$  is the Bose-Einstein distribution function,  $v_a(\omega, p)$  is the group velocity (on side  $a$ ) for a phonon characterized by frequency  $\omega$ , moving in direction  $(\theta, \phi)$  with polarization  $p$ . The relevant material properties are the density of phonon states,  $\rho_a(\omega, p)$ , and the transmission probability,  $\tau_{ab}(\omega, p)$ , at the interface. [13, 19, 20] The DMM also assumes that phonons scatter into states with the same frequency on either side, and that the scattering phonons lose memory of their incident angles. This requires a symmetry in the transmission probabilities,

$$\tau_{ab}(\omega) = 1 - \tau_{ba}(\omega) \quad (1.4)$$

The DMM has a number of significant issues, particularly when the Debye model does a poor job representing the density of states, or where there is a fictitious boundary between identical materials (where the DMM predicts a non-zero resistance). [13] There is also an assumption of detailed balance built-in to the model, [8] which requires the two sides to be at equilibrium. The DMM is more appropriate for modeling thermal transport at noncryogenic temperatures and at rough interfaces because the majority of acoustic phonons at  $\geq 300$  K have short wavelengths. The wavelengths at these temperatures are comparable to the interatomic spacing in the system.

While attempts to account for interfacial bonding have been made in the AMM, the DMM interfacial methods have not been developed. The interaction of the ma-

terials at the interface has been found to be of significant importance to thermal conductivity [21–23], but a factor to include this interaction has yet to be incorporated in the theory. Despite the DMM’s pitfalls, it has been the most commonly used model for the past 30 years. [11, 12, 18, 24]

## 1.2 Molecular Dynamics

Molecular dynamics is a computer simulation technique used to study structure and dynamics for atoms and molecules using classical mechanics. A simple algorithm of a molecular dynamics simulation can be described given atoms with initial positions and velocities, and forces (derived from potential energy surfaces described later) that are used to move the atoms. The time is incremented and the cycle repeats by calculating the forces (see Figure 1.2). The atomic motion follows from Newton’s equations of motion. The positions and velocities at each time step create a trajectory of the system that is time reversible.

Forces between each pair of atomic sites are computed from an interaction potential, where the forces are the gradient of the scalar potential:

$$\vec{F}(\vec{R}, t) = -\vec{\nabla} \cdot V(\vec{R}) \quad (1.5)$$

These potentials are approximated using intra and inter molecular forces in the system to make an approximate potential energy surface with respect to the nuclear coordinates of the system. [25]

$$V(\vec{R}) = V_{bonded} + V_{electrostatic} + V_{vdW} + V_{metallic} + V_{constraints} + V_{hb} \quad (1.6)$$

The simplest of these to start with is the intra-molecular forces  $V_{bonded}$ , composed of bonds, bends, and torsions. Typical bonding potentials take the form of either

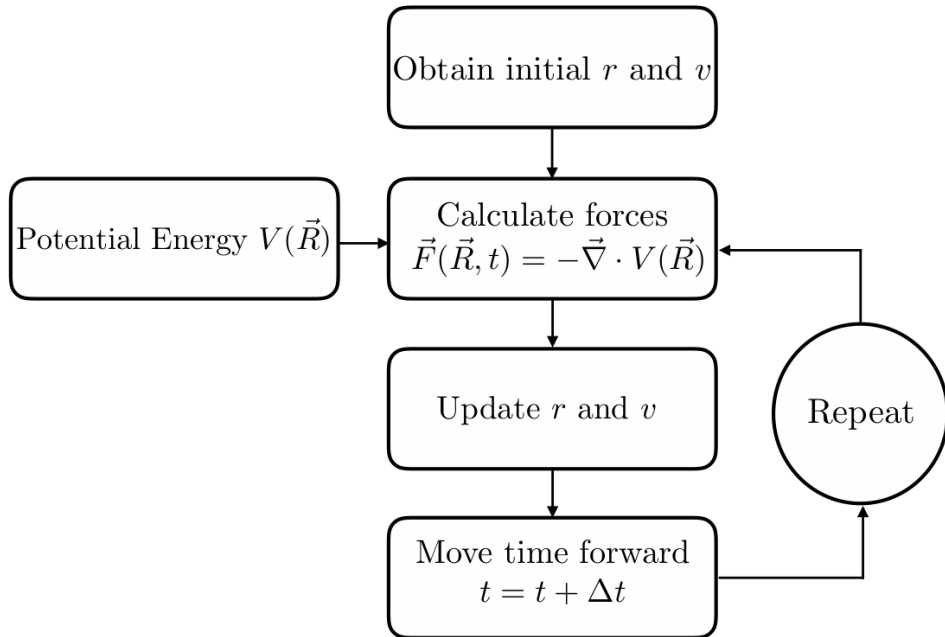


Figure 1.2. The initial positions,  $r$ , and velocities,  $v$ , are established in a system and from the potential energy, forces on the atoms is found. From the forces, positions can be changed then the velocities can be updated. The time can be moved forward and the process repeated at the calculated forces step until the desired time is reached.

harmonic bonds,

$$V_{bond}(r) = \frac{k_{ij}}{2} (r - r_{ij}^0)^2 \quad (1.7)$$

or Morse bonds,

$$V_{bond}(r) = D_{ij} [1 - \exp^{-\beta(r - r_{ij}^0)}]^2. \quad (1.8)$$

While other potential forms such as cubic and quartic can be used, the main form used in the following work will follow the harmonic form. In the harmonic form there are two variables that need to be provided:  $k_{ij}$  and  $r_{ij}^0$ . The former is the spring constant associated with how the bond behaves when stretched and contracted. The latter is the equilibrium bond distance between the two atoms.

Similar to the bonding potentials, the bending potentials may take many forms. In this work, the harmonic potential,

$$V_{bend}(\theta) = \frac{k_{ijk}}{2} (\theta - \theta_{ijk}^0)^2, \quad (1.9)$$

was used, where  $\theta$  is the angle between three connecting beads  $i$ ,  $j$ , and  $k$ .  $\theta_{ijk}^0$  is the equilibrium bend angle and  $k_{ijk}$  is the spring constant for the bend.

The potential due to torsions within a bonded system is from the rotation of the plane made from the  $i$ ,  $j$ , and  $k$  points relative to the  $l$  point:

$$V_{torsions}(\phi_{ijkl}) = c_1[1 + \cos \phi_{ijkl}] + c_2[1 + \cos 2\phi_{ijkl}] + c_3[1 + \cos 3\phi_{ijkl}] \quad (1.10)$$

where the angle  $\phi_{ijkl}$  is  $(\hat{r}_{ij} \times \hat{r}_{jk}) \cdot (\hat{r}_{jk} \times \hat{r}_{kl})$  and  $\hat{r}_{ab}$  is the unit vector between  $a$  and  $b$ .

Inter-molecular, or non-bonded interactions, are interactions between molecules which include the electrostatic interactions and van der Waals interactions, as well

as metallic interactions. The potential for electrostatic interactions

$$V_{electrostatic} = \frac{q_i q_j}{4\pi\epsilon_0 |r_{ij}|}, \quad (1.11)$$

describes the potential between two charged sites interacting via Coulomb's law. Van der Waals interactions in this work are described via the Lennard Jones potential,

$$V_{vdW} = 4\epsilon \left[ \left( \frac{\sigma}{|r|} \right)^{12} + \left( \frac{\sigma}{|r|} \right)^6 \right] \quad (1.12)$$

where  $\epsilon$  is the well depth when the distance between the two bodies is at the minimum and  $\sigma$  is the distance the well starts from zero. The  $\frac{1}{r^6}$  term is similar to dispersion and the  $\frac{1}{r^{12}}$  term is empirically added to approximate repulsion due to electron exchange correlation.

The last, and one of the most important terms for the work is  $V_{metallic}$ . Quantum Sutton-Chen(qSC) potential is the metallic potential used in all the following projects.[26] The potential is broken into two parts: a pair potential and the local density accounting for cohesion.

$$V_{metallic} = \sum_i \epsilon \left[ \sum_{j \neq i} V_{ij}^{pair}(r_{ij}) - c\sqrt{\rho_i} \right] \quad (1.13)$$

$$V_{ij}^{pair}(r) = \left( \frac{a_{ij}}{r_{ij}} \right)^{n_{ij}} \quad (1.14)$$

$$\rho_i = \sum_{i \neq j} \left( \frac{a_{ij}}{r_{ij}} \right)^{m_{ij}} \quad (1.15)$$

For gold, which is the only metal present in this work the following values are used:  $n = 11$ ,  $m = 8$ ,  $\epsilon = 7.8052 \times 10^{-3}$  eV,  $c = 53.582$ , and  $a = 4.0651$  Å. The *epsilon* value is the well depth of the metallic interact and  $a$  is the lattice parameter of the metal. The qSC potential is the quantum corrected form of the Sutton-Chen

potential. Other common potential for metal interactions are Lennard-Jones and Embedded Atom Method (EAM).[27]

The last two terms in the full potential equation,  $V_{constraints}$  and  $V_{hb}$ , hydrogen bonding, are not relevant to the simulations presented in this work.

### 1.2.1 Representations of Atoms

Molecular dynamics is a lower accuracy method than first principles methods. There are different levels of simplification of the treatment of molecules. [25] Chiefly, there are three ways of treating the molecules in a given system that will be discussed here. The first, all-atom, is representing each atom within the system as a bead. In a molecule, these beads share bonds with atoms they are covalently bonded with and experiences bends and torsions within the larger molecule.

The next is a simplified version of the all-atom representation, united-atom, which compresses the hydrogen atoms onto the larger atom to which they were bonded. The mass and atomic radius of this bead is increased according to the number of hydrogens added.

United-atom calculations are faster due to the decrease in N, the number of atoms. They also are a better representation of heat transport. The vibrations of the molecules are of paramount importance in thermal transport and bonds to hydrogen have a high vibrational frequency. In molecular dynamics, the vibrational modes are occupied equally due to equipartition of the energy, thus the vibrational spectrum of the molecule will have high frequency C–H, N–H, or O–H peaks. These high frequencies are irrelevant in most thermal transport calculations and thus all-atom simulations add expense and information that detracts from the low frequency picture of the system.

The last treatment discussed here is coarse-grained systems. These systems are further simplifications of the atoms present in the molecules. In coarse-grain systems,

beads from the united atom model would be grouped into a single bead that represents a small molecule. The granularity of the beads can be adjusted from system to system and depends on the property desired and the timescale of the simulation. In general, coarse-graining is used widely for biologically relevant systems (i.e. proteins, lipids, etc.).

### 1.2.2 Boundary Conditions

In many simulations the desired quantity is a bulk property. To simulate a full bulk system would require too many atoms and too much time than possible within the lifetime of a graduate student. Further, the large box would have effects from the edges of the box. So how can the surface effects be avoided and simulate a bulk-like simulation?

The above issues can be addressed with periodic boundary conditions. A simulation cell that has bulk-like density can reproduce bulk properties. Periodic boundary conditions are typically applied to orthorhombic simulation boxes, though any space filling geometry works. An ‘image’ copy of the the simulation box is replicated in every direction. For example, in two dimensions periodic boundaries are represented in Figure 1.3, where the simulation box has eight copies. In three dimensions, twenty-six images of the original box surround the simulation cell, for an orthorhombic box.

In a simulation, it is only necessary to track the particles in the central box. The particles’ images in neighboring cells are located at integer increments of the box dimension along each principal axis. So if the particle exits the right boundary of the cell, it will return in the box on the left boundary (from the neighboring simulation cell), which preserves the number density of the cell. In addition to periodic boundaries, the minimum image convention is used to make the simulation computationally tractable. A particle only interacts with the closest periodic image of another particle in the system. This convention requires a spherical cutoff, where a particle’s non-

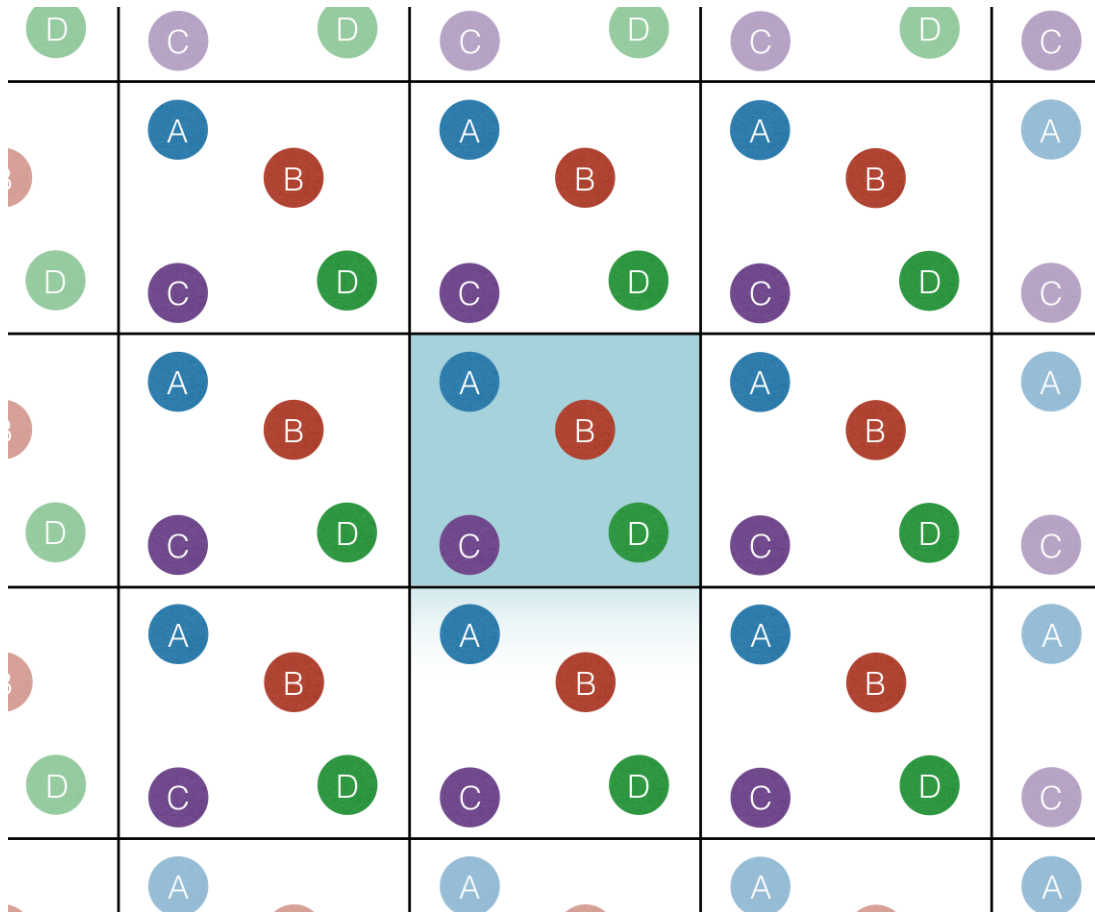


Figure 1.3. This figure is an example of periodic boundaries in two dimensions. Here the middle cell (colored square) is the system and each surrounding cell is an ‘image’ of the original. As can be seen in the relation between particle A and C, sometimes the image particle provides the closest interaction or minimum image and would be within the cutoff radius when calculating interactions.

bonded interactions with other particles end at a finite distance,  $r$ , from the particle which is less than half the length of the periodic box. This ensures that the particle sees one image of each particle and does not interacting with an image of itself.

Though periodic boundaries allows for bulk properties to be found, it creates artificial periodicity in the system and might require an unreasonable system size due to the box structure. Later in this work, simulations of isolated particles are utilized to get single particle properties. These isolated systems use the Langevin Hull method. While there are several non-periodic methods that allow for a constant pressure, the Langevin Hull can handle heterogeneous mixtures of materials with different compressibilities. [1] This method is a modified version of Kohanoff, Caro, and Finnis' method for constant pressure and temperature non-periodic simulations based on Langevin dynamics. [28, 29]

In the Langevin Hull method, the boundary of the system is a completely convex hull made of facets from points triangulated with the outermost atoms of the system. This hull interacts with a system bath that applies constant pressure and provides a thermal bath for the system through the facets of the hull. When looking at thermal properties of a system, the thermal coupling can be turned off to prevent artificial behavior due to the bath.

### 1.3 Transport Coefficients

Transport phenomena are controlled by the constitutive equations that describe how a material responds to various stimuli via transport. The processes that are at the center of transport phenomena concern the transfer of mass, heat, or momentum. The transport of any of those listed would create a measurable flux in the system. The conservation equations conserve the desired property of interest in the presence of a flux. The constitutive equations relate a transport property (diffusion, thermal conductivity, viscosity) to a flux via an empirical relationship. The flux, in all these

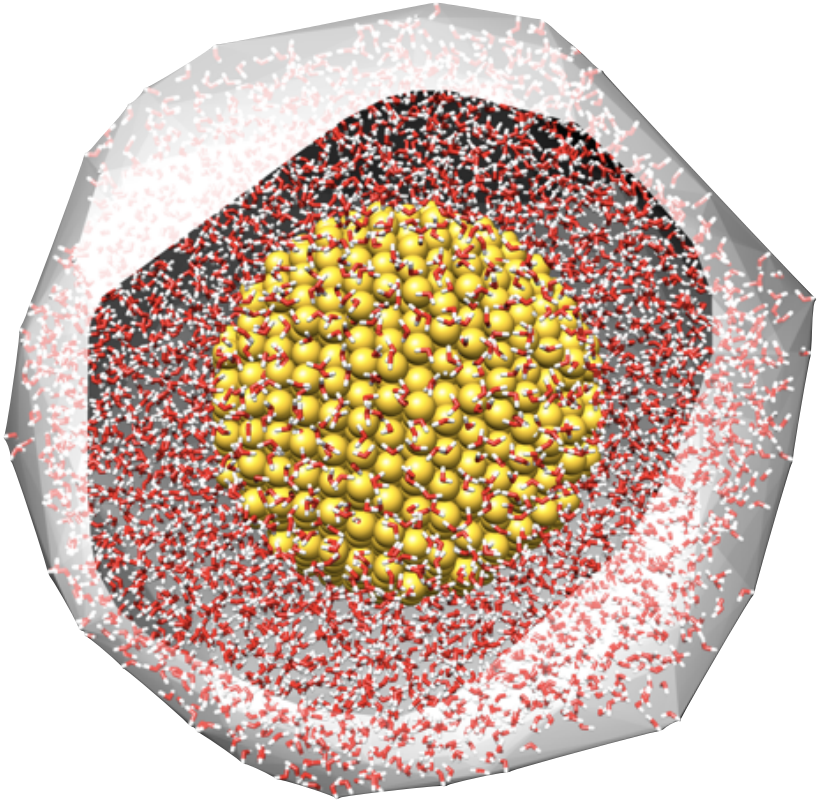


Figure 1.4. Visualization of a gold particle solvated in water within the Langevin Hull taken from Vardeman *et. al.* [1]. The temperature and pressure bath interact with only the outer most atoms on the hull, the grey translucent surface. At each time step the hull is computed to ensure the atoms are interacting in the correct classifications, as edge atoms or as interior atoms.

cases, is proportional to the gradient and a constant of proportionality.

TABLE 1.1

Constitutive and balance equations related to the transport coefficients of diffusivity,  $D$ , thermal conductivity,  $\lambda$ , and shear viscosity,  $\eta$ .

Transport coefficients	Constitutive equations	Balance equations
$D$	$\vec{j} = -D \cdot \vec{\nabla} c(\vec{r}, t)$	$\frac{\partial c(\vec{r}, t)}{\partial t} + \vec{\nabla} \cdot \vec{j} = 0$
$\lambda$	$\vec{q} = -\lambda \cdot \vec{\nabla} T(\vec{r}, t)$	$C_p \frac{\partial T(\vec{r}, t)}{\partial t} + \vec{\nabla} \cdot \vec{q} = 0$
$\eta$	$\sigma_{x,z} = -\eta \cdot \vec{\nabla}_z (\rho v_x)$	$\rho \frac{D \vec{v}(\vec{r}, t)}{Dt} + \vec{\nabla}_z \cdot \vec{\sigma} = 0$

- Diffusion (Fick's Law):  $\vec{j} = -D \cdot \vec{\nabla} c(\vec{r}, t)$

The diffusivity,  $D$ , or the diffusion coefficient is the proportionality between the concentration gradient of a species and the mass flux,  $j$ .

- Thermal Conductivity (Fourier's Law):  $\vec{q} = -\lambda \cdot \vec{\nabla} T(\vec{r}, t)$

The local heat flux density,  $q$ , is the product of the conductivity of the material,  $\lambda$ , and the temperature gradient through the material. Therefore,  $\lambda$  indicates the material's ability to conduct heat due to a temperature gradient.

- Viscosity (Newton's Law of Viscosity):  $\sigma_{x,z} = -\eta \cdot \vec{\nabla}_z (\rho v_x)$

The shear stress in the fluid,  $\sigma$ , is the product of the shear viscosity,  $\eta$ , and the perpendicular velocity gradient,  $\vec{\nabla}_z (\rho v_x)$ .

All the transport coefficients ( $D$ ,  $\lambda$ ,  $\eta$ ) describe how an instantaneous flux in a system relates to a corresponding gradient. Table 1.1 lists how the transport

coefficients are involved in constitutive equations, where  $\rho$  is the density and  $C$  is the heat capacity of a material.

Transport phenomena are utilized in many fields, such as chemistry, physics, chemical engineering, electrical engineering, and mechanical engineering; to obtain the transport coefficients that describe a mechanical or chemical system. Atomistic simulations can provide insight for tuning experimental design. The three main ways to calculate transport coefficients, with a focus on thermal conductivity, will be discussed in detail in the following sections.

### 1.3.1 Equilibrium Molecular Dynamics

Transport properties from classical molecular dynamics simulations can be found using many methods. Equilibrium Molecular Dynamics (EMD) simulations use the most straightforward method. Under linear response theory, the transport coefficient can often be found using a relevant time correlation function to the transport coefficient of interest. [30–35] In most cases either the Einstein relation or the Green-Kubo formulation are utilized to compute transport properties from the time correlation function in EMD.

The Einstein relation for thermal conductivity uses the Helfand moment,  $G^\lambda(t)$ , which is a centroid of the particle energies:

$$G^\lambda(t) = \sum_{a=1}^N r_a(E_a - \langle E_a \rangle) \quad (1.16)$$

where  $E_a$  is the energy of the particle  $a$ . Energy is given by the following:

$$E_a = \frac{p_a^2}{2m} + \frac{1}{2} \sum_{b \neq a} U(r_{ab}) \quad (1.17)$$

where  $p_a$  is the momentum of  $a$ ,  $m$  is the mass, and  $U(r_{ab})$  is the potential energy

due to the presence of  $a$ .

The Einstein relation can find the thermal conductivity using the fluctuations in the Helfand moment:

$$\lambda = \lim_{N,V,t \rightarrow \infty} \frac{1}{2k_B T^2 V t} \left\langle \left[ G^\lambda(t) - G^\lambda(0) \right]^2 \right\rangle \quad (1.18)$$

where  $k_B$  is the Boltzmann constant,  $T$  is the temperature,  $V$  is the volume, and  $t$  is the time.

The equivalent Green-Kubo relation for thermal conductance is

$$\lambda = \frac{1}{3V k_B T^2} \int_0^\infty dt \langle q(t) \cdot q(0) \rangle \quad (1.19)$$

where  $q$  is the heat current. The heat current can be found through

$$q(t) = \sum_{i=1}^N E_i \vec{v}_i + \frac{1}{2} \sum_{j \neq i} r_{ij}^\vec{\cdot} (f_{ij} \cdot \vec{v}_j). \quad (1.20)$$

The first term is a summation of the energy times the velocity of all particles. The second term contains the force on atom  $i$  due to atom  $j$ ,  $f_{ij}$ . In contrast to the Einstein relation where the mass, velocity, and potential are easily obtained from an equilibrium simulation, the heat current requires significantly more effort.

Both the Einstein and Green-Kubo relations for thermal conductivity rely on correlation functions, where the long-time tails are able to significantly contribute to the integrated area and need long simulation times to achieve convergence. The noise and poor convergence in the long-time tails give a poor estimation for the thermal conductivity and thus EMD simulations are not the best method for calculating this transport coefficient. Moreover, these calculations have further complications when the systems contain an interface or are non-homogeneous.

### 1.3.2 Non-Equilibrium Molecular Dynamics

Since EMD has limitations due to the noise in the correlation function, methods in non-equilibrium molecular dynamics, NEMD, were developed that introduce a gradient into the simulations. [36–39] Typically these methods are used to impose a temperature or velocity gradient on a system to measure the corresponding transport coefficient. [36–48] With linear response of a flux due to the applied gradient, the transport coefficient can be calculated using the constitutive equation:  $J_z = -\lambda \frac{\partial T}{\partial z}$ , where  $\frac{\partial T}{\partial z}$  is imposed and  $J_z$  is the resulting flux. In NEMD, the temperature gradient is imposed by choosing sections of the simulation box to have particular temperatures. For example, a center portion of the system will be set to high temperature and the edges set to a lower temperature to impose the gradient. The imposed thermal gradient must be relatively small to maintain a linear relationship between the flux and the gradient. The corresponding transport coefficient, thermal conductivity, can be found if linear response holds.

Accurately measuring the thermal flux from the imposed gradient is difficult. This method requires thermostats to maintain the thermal gradient which means that it does not ensure momentum or energy conservation and that simulations are restricted to the canonical ensemble. Additionally, in heterogeneous systems, particularly with interfaces, it can be difficult to know what the shape of the imposed gradient should be at the boundaries of materials.

### 1.3.3 Reverse Non-Equilibrium Molecular Dynamics

Reverse non-equilibrium molecular dynamics (RNEMD) methods impose an unphysical flux and measure the gradient that develops. [49–51] Imposed flux methods are preferable because the simulation imposes the difficult to measure quantity, the flux, causing the system to develop a gradient, which is easier to measure, between the regions where the flux is imposed. Since the measurement of a gradient is less

complex, the imposed flux methods will typically take less time to obtain converged results, therefore the simulations are less time intensive and less costly.

The original RNEMD formulation imposes an artificial momentum flux between parallel slabs of material separated in the simulation cell. The flux was created by periodically swapping the momentum between molecules in each of the slabs in a homogeneous system. [49] This method was modified to obtain other transport coefficients [50] and to handle heterogeneous systems. [52] An attractive feature of RNEMD is that the algorithm conserves total linear momentum and total energy. However, issues with large fluxes can result in non-linear gradients, where linear response can not be used to find the transport coefficient. [53]

This method has become widely used for thermal and mechanical properties of homogeneous and heterogeneous systems of solids and liquids [49, 50, 53], as well as, interfaces. [54–57] Gradients near interfaces exhibit distinct behavior at the boundaries of dissimilar materials.

Recent advances in RNEMD methodology have involved scaling particle velocities instead of swapping. The scaling method uses constraint equations that require the simulation to conserve total energy and total linear momentum. [51, 56] In addition, this RNEMD method has been extended to handle non-periodic heterogeneous systems. [58]

#### 1.4 Systems of Interest

The systems that are explored in this work contain a solvated gold substrate or particle with heat transport from the gold to the solvent. Thermal properties of gold particles have been of great experimental interest, with a particular interest in detangling the important factors for transport: particle size, [59–63] composition, [64, 65] surface modification, [60, 62, 65–70] surface supports, [71] exposed surface facets, [68] and the chemical details of the environment. [61, 65, 67, 69, 71, 72]

Three distinct studies examining interfacial thermal conductivity and heat transport will be explored with three different systems in this work. The first system contains nanospheres with a range of particle radii and ligands with different length and rigidity. [62] The second system strips away the ligand layer and looks at bare particles with the intention of finding the role of in particle morphology. [73] How exactly does the surface of the particle affect heat transport? The third system looks at a more complex problem: how does the particle size and the system solvent change thermal conductivity of a nanoarray? To simplify the atomistic models, we use a united-atom model for the ligand layer and solvent. All the non-periodic systems use the Langevin Hull [1] and RNEMD methods for calculating transport properties. [58]

## CHAPTER 2

### INTERFACIAL THERMAL CONDUCTANCE OF THIOLATE-PROTECTED GOLD NANOSPHERES

#### 2.1 Introduction

Heat transport across various nanostructured interfaces has been the subject of intense experimental interest,[55, 64, 74–79] and the interfacial thermal conductance,  $G$ , is the principal quantity of interest for understanding interfacial heat transport.[80] Because nanoparticles have a significant fraction of their atoms at the particle / solvent interface, the chemical details of these interfaces govern the thermal transport properties. Time-domain thermoreflectance (TDTR) measurements on planar self-assembled monolayer (SAM) junctions between quartz and gold films showed that surface chemistry, particularly the density of covalent bonds to the gold surface, can control energy transport between the two solids.[81] Experiments and simulations on three-dimensional nanocrystal arrays have similarly shown that surface-attached ligands mediate the thermal transport in these materials, placing particular importance on the overlap between the ligand and nanoparticle vibrational densities of states.[65, 67] Likewise, simulations of polymer-coated gold nanoparticles in water have shown that the surface coating introduces a dominant thermal transport channel to the surrounding solvent.[82]

For ligand-protected nanoparticles in a solvent, there may be three distinct heat transfer processes: (1) from the particles to the ligands, (2) vibrational energy transfer along the length of the ligand, followed by (3) heat transport from the ligand to the surrounding solvent.[83]

Heat transport at the gold-alkylthiolate-solvent interface has been previously explored both through molecular dynamics simulations and via TDTR.[56, 57, 84, 85] Most of these studies have found that alkylthiolates enhance the thermal conductance to the solvent, and that the vibrational overlap provided by the chemically-bound ligand species plays a role in this enhancement.

Reverse nonequilibrium molecular dynamics (RNEMD) methods [49] have been previously applied to calculate the thermal conductance at flat (111) metal / organic solvent interfaces that had been chemically protected by varying coverages of alkanethiolate groups.[56] These simulations suggested an explanation for the increased thermal conductivity at alkanethiol-capped metal surfaces compared with bare metal interfaces. Specifically, the chemical bond between the metal and the ligand introduces a vibrational overlap that is not present without the protecting group, and the overlap between the vibrational spectra (metal to ligand, ligand to solvent) provides a mechanism for rapid thermal transport across the interface. The simulations also suggested that this phenomenon is a non-monotonic function of the fractional coverage of the surface, as moderate coverages allow energy transfer to solvent molecules that come into close contact with the ligands.

Similarly, simulations of mixed-chain alkylthiolate surfaces showed that solvent trapped close to the interface can be efficient at moving thermal energy away from the surface.[57] Trapped solvent molecules that were orientationally aligned with nearby ligands were able to increase the thermal conductance of the interface. This indicates that the ligand-to-solvent vibrational energy transfer is a key feature for increasing particle-to-solvent thermal conductance.

RNEMD methods have been extended for use in non-periodic geometries by creating scaling/shearing moves between concentric regions of a simulation.[58] In this section, a non-periodic variant of RNEMD has been applied to investigate the role that curved nanoparticle surfaces play in heat and mass transport. On planar surfaces,

it has been seen that orientational ordering of surface protecting ligands had a large effect on the heat conduction from the metal to the solvent.[57] Smaller nanoparticles have high surface curvature that creates gaps in well-ordered self-assembled monolayers, and the effect of those gaps on the thermal conductance is unknown.

## 2.2 Interfacial Thermal Conductance of Metallic Nanoparticles

For a solvated nanoparticle, it is possible to define a critical value for the interfacial thermal conductance,

$$G_c = \frac{3C_s\lambda_s}{RC_p} \quad (2.1)$$

which depends on the solvent heat capacity,  $C_s$ , solvent thermal conductivity,  $\lambda_s$ , particle radius,  $R$ , and nanoparticle heat capacity,  $C_p$ .[64] In the limit of infinite interfacial thermal conductance,  $G \gg G_c$ , cooling of the nanoparticle is limited by the solvent properties,  $C_s$  and  $\lambda_s$ . In the opposite limit,  $G \ll G_c$ , the heat dissipation is controlled by the thermal conductance of the particle / fluid interface. It is this regime with which this study is concerned, where properties of ligands and the particle surface may be tuned to manipulate the rate of cooling for solvated nanoparticles. Based on estimates of  $G$  from previous simulations as well as experimental results for solvated nanostructures, gold nanoparticles solvated in hexane are in the  $G \ll G_c$  regime for radii smaller than 40 nm. The particles included in this study are more than an order of magnitude smaller than this critical radius, therefore the heat dissipation should be controlled entirely by the surface features of the particle / ligand / solvent interface.

### 2.2.1 Structures of Self-Assembled Monolayers on Nanoparticles

Though the ligand packing on planar surfaces has been characterized for many different ligands and surface facets, it is not obvious *a priori* how the same ligands

will behave on the highly curved surfaces of spherical nanoparticles. Thus, as new applications of ligand-stabilized nanostructures have been proposed, the structure and dynamics of ligands on metallic nanoparticles have been studied using molecular simulation,[86] NMR, XPS, FTIR, calorimetry, and surface microscopies.[87–91] Badia, *et al.* used transmission electron microscopy to determine that alkanethiol ligands on gold nanoparticles pack approximately 30% more densely than on planar Au(111) surfaces.[87] Subsequent experiments demonstrated that even at full coverages, surface curvature creates voids between linear ligand chains that can be filled via interdigitation of ligands on neighboring particles.[88] The molecular dynamics simulations of Henz, *et al.* indicate that at low coverages, the thiolate alkane chains will lie flat on the nanoparticle surface.[86] Above 90% coverage, the ligands stand upright and recover the rigidity and tilt angle displayed on planar facets. Their simulations also indicate a high degree of mixing between the thiolate sulfur atoms and surface gold atoms at high coverages.

In this work, thiolated gold nanospheres were modeled using a united atom force field and non-equilibrium molecular dynamics. Gold nanoparticles with radii ranging from 10 - 25 Å were created from a bulk fcc lattice. These particles were passivated with a 50% coverage (compared with the coverage densities reported by Badia *et al.*) of a selection of thiolates. Three straight-chain thiolates of varying chain lengths and rigidities were utilized. These are summarized in Figure 2.1. The passivated particles were then solvated in hexane. Details on the united atom force field are given below.

## 2.3 Computational Details

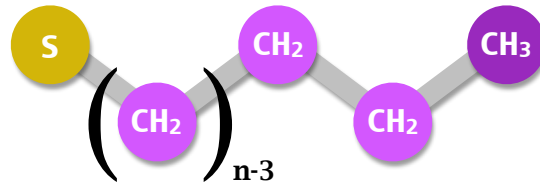
### 2.3.1 Creating a thermal flux between particles and solvent

The non-periodic variant of the velocity shearing and scaling RNEMD algorithm (VSS-RNEMD)[58] applies a series of velocity scaling and shearing moves at regular

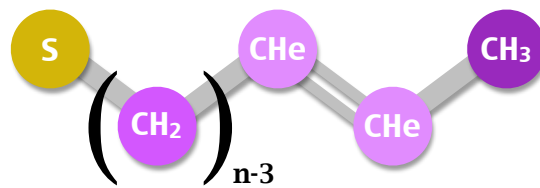
## **Species** **Structure**

---

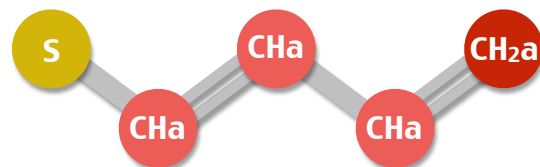
alkanethiolates  
 $n = 4, 8, 12$



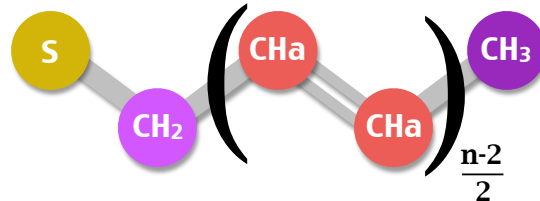
penultimate  
alkenethiolates  
 $n = 4, 8, 12$



conjugated  
alkenethiolates  
 $n = 4$



$n = 8, 12$



hexane

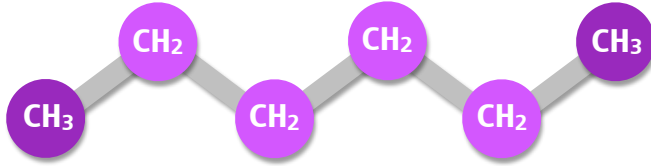


Figure 2.1. Topologies of the thiolate capping agents and solvent utilized in the simulations. The chemically-distinct sites (S,  $\text{CH}_2$ ,  $\text{CH}_3$ , CHe, CHa and  $\text{CH}_2\text{a}$ ) are treated as united atoms. Most parameters are taken from references [2], [3] [4]. Cross-interactions with the Au atoms were adapted from references [5], [6], and [7].

intervals to impose a flux between two concentric spherical regions. The scaling coefficients  $a$  and  $b$  are solved for to impose a thermal flux between the shells (without an accompanying angular shear)

$$a = \sqrt{1 - \frac{q_r \Delta t}{K_a - K_a^{\text{rot}}}} \quad (2.2)$$

$$b = \sqrt{1 + \frac{q_r \Delta t}{K_b - K_b^{\text{rot}}}} \quad (2.3)$$

at each time interval. These scaling coefficients conserve total kinetic energy and angular momentum subject to an imposed heat rate,  $q_r$ . The coefficients also depend on the instantaneous kinetic energy,  $K_{\{a,b\}}$ , and the total rotational kinetic energy of each shell,  $K_{\{a,b\}}^{\text{rot}} = \sum_i m_i (\mathbf{v}_i \times \mathbf{r}_i)^2 / 2$ .

The scaling coefficients are determined and the velocity changes are applied at regular intervals,

$$\mathbf{v}_i \leftarrow a (\mathbf{v}_i - \langle \omega_a \rangle \times \mathbf{r}_i) + \langle \omega_a \rangle \times \mathbf{r}_i \quad (2.4)$$

$$\mathbf{v}_j \leftarrow b (\mathbf{v}_j - \langle \omega_b \rangle \times \mathbf{r}_j) + \langle \omega_b \rangle \times \mathbf{r}_j. \quad (2.5)$$

Here  $\langle \omega_a \rangle \times \mathbf{r}_i$  is the contribution to the velocity of particle  $i$  due to the overall angular velocity of the  $a$  shell. In the absence of an angular momentum flux, the angular velocity  $\langle \omega_a \rangle$  of the shell is nearly 0 and the resultant particle velocity is a nearly linear scaling of the initial velocity by the coefficient  $a$  or  $b$ .

Repeated application of this thermal energy exchange yields a radial temperature profile for the solvated nanoparticles that depends linearly on the applied heat rate,  $q_r$ . Similar to the behavior in the slab geometries, the temperature profiles have discontinuities at the interfaces between dissimilar materials. The size of the discontinuity depends on the interfacial thermal conductance, which is the primary

quantity of interest.

### 2.3.2 Interfacial Thermal Conductance

The thermal conductance of each spherical shell may be defined as the inverse Kapitza resistance of the shell.[58] To describe the thermal conductance of an interface of considerable thickness – such as the ligand layers shown here – sum the individual thermal resistances of each concentric spherical shell to arrive at the inverse of the total interfacial thermal conductance. In concentric spherical shells, the intermediate temperatures and surface areas remain in the final sum, requiring the use of a series of individual resistance terms:

$$\frac{1}{G} = R_{\text{total}} = \frac{1}{q_r} \sum_i (T_{i+i} - T_i) 4\pi r_i^2. \quad (2.6)$$

The longest ligand considered here is in excess of 15 Å in length, and 10 concentric spherical shells are used to describe the total interfacial thermal conductance of the ligand layer.

### 2.3.3 Force Fields

Throughout this work, gold – gold interactions are described by the quantum Sutton-Chen (QSC) model.[26] Previous work[56] has demonstrated that the electronic contributions to heat conduction (which are missing from the QSC model) across heterogeneous metal / non-metal interfaces are negligible compared to phonon excitation, which is captured by the classical model. The hexane solvent is described by the TraPPE united atom model,[2] where sites are located at the carbon centers for alkyl groups. The TraPPE-UA model for hexane provides both computational efficiency and reasonable accuracy for bulk thermal conductivity values. Bonding interactions were used for intra-molecular sites closer than 3 bonds. Effective Lennard-

Jones potentials were used for non-bonded interactions.

TABLE 2.1

Non-bonded interaction parameters (including cross interactions with Au atoms).

Site	mass (amu)	$\sigma_{ii}$ (Å)	$\epsilon_{ii}$ (kcal/mol)	$\sigma_{\text{Au}-i}$ (Å)	$\epsilon_{\text{Au}-i}$ (kcal/mol)	source
CH <sub>3</sub>	15.04	3.75	0.1947	3.54	0.2146	Refs. [2], [6] and [5]
CH <sub>2</sub>	14.03	3.95	0.09141	3.54	0.1749	Refs. [2], [6] and [5]
CHene	13.02	3.73	0.09340	3.4625	0.1680	Refs. [3], [6] and [5]
S	32.0655	4.45	0.2504	2.40	8.465	Refs. [5] ( $\sigma$ ) and [6] ( $\epsilon$ )
Char	13.02	3.695	0.1004	3.4625	0.1680	Refs. [3] and [6]
CH <sub>2</sub> ar	14.03	3.695	0.1004	3.4625	0.1680	Refs. [3] and [6]

The TraPPE-UA force field includes parameters for thiol molecules[4] as well as unsaturated and aromatic carbon sites.[3] These were used for the thiolate molecules

in the following simulations, and missing parameters for the ligands were supplemented using fits described below. Bonds are rigid in TraPPE-UA, so although equilibrium bond distances were taken from this force field, flexible bonds were implemented using bond stretching spring constants adapted from the OPLS-AA force field.[92]

TABLE 2.2

Bond parameters for the ligand molecules.

<i>i</i>	<i>j</i>	<i>r</i> <sub>0</sub> (Å)	<i>k</i> <sub>bond</sub> ( kcal/mole/Å <sup>2</sup> )	source
CH <sub>3</sub>	CH <sub>3</sub>	1.540	536	Refs. [2] and [92]
CH <sub>3</sub>	CH <sub>2</sub>	1.540	536	Refs. [2] and [92]
CH <sub>2</sub>	CH <sub>2</sub>	1.540	536	Refs. [2] and [92]
CHene	CHene	1.330	1098	Refs. [3] and [92]
CH <sub>3</sub>	CHene	1.540	634	Refs. [3] and [92]
CH <sub>2</sub>	CHene	1.540	634	Refs. [3] and [92]
S	CH <sub>2</sub>	1.820	444	Refs. [4] and [92]
Char	Char	1.40	938	Refs. [3] and [92]
Char	CH <sub>2</sub>	1.540	536	Refs. [3] and [92]
Char	CH <sub>3</sub>	1.540	536	Refs. [3] and [92]
CH <sub>2</sub> ar	Char	1.40	938	Refs. [3] and [92]
S	Char	1.80384	527.951	This Work

Parameters not found in the TraPPE-UA force field for the intramolecular interactions of the conjugated and the penultimate alkenethiolate ligands were calculated using constrained geometry scans using the B3LYP functional [93, 94] and the 6-31G(d,p) basis set. Structures were scanned starting at the minimum energy gas phase structure for small ( $C_4$ ) ligands. Only one degree of freedom was constrained for any given scan – all other atoms were allowed to minimize subject to that constraint. The resulting potential energy surfaces were fit to a harmonic potential for the bond stretching,

$$V_{\text{bond}} = \frac{k_{\text{bond}}}{2} (r - r_0)^2, \quad (2.7)$$

and angle bending potentials,

$$V_{\text{bend}} = \frac{k_{\text{bend}}}{2} (\theta - \theta_0)^2. \quad (2.8)$$

Torsional potentials were fit to the TraPPE torsional function,

$$V_{\text{tor}} = c_0 + c_1 (1 + \cos \phi) + c_2 (1 - \cos 2\phi) + c_3 (1 + \cos 3\phi). \quad (2.9)$$

For the penultimate thiolate ligands, the model molecule used was 2-Butene-1-thiol, for which one bend angle (S–CH<sub>2</sub>–CHene) was scanned to fit an equilibrium angle and force constant, as well as one torsion (S–CH<sub>2</sub>–CHene–CHene). The parameters for these two potentials also served as model for the longer conjugated thiolate ligands which require bend angle parameters for (S–CH<sub>2</sub>–CChar) and torsion parameters for (S–CH<sub>2</sub>–CChar–CChar).

For the  $C_4$  conjugated thiolate ligands, the model molecule for the quantum mechanical calculations was 1,3-Butadiene-1-thiol. This ligand required fitting one bond (S–CChar), and one bend angle (S–CChar–CChar).

The geometries of the model molecules were optimized prior to performing the

constrained angle scans, and the fit values for the bond, bend, and torsional parameters were in relatively good agreement with similar parameters already present in TraPPE.

To derive suitable parameters for the thiolates adsorbed on Au(111) surfaces, the S parameters from Luedtke and Landman[5] were adopted and modified the parameters for the CTS atom to maintain charge neutrality in the molecule.

Other interactions between metal (Au) and non-metal atoms were adapted from an adsorption study of alkyl thiols on gold surfaces by Vlugt, *et al.*[6] They fit an effective pair-wise Lennard-Jones form of potential parameters for the interaction between Au and pseudo-atoms  $\text{CH}_x$  and S based on a well-established and widely-used effective potential of Hautman and Klein for the Au(111) surface.[7] All simulations were carried out with the open source molecular dynamics package, OpenMD.[95, 96]

TABLE 2.3

Bend angle parameters. The central atom in the bend is atom  $j$ .

$i$	$j$	$k$	$\theta_0$ (°)	$k_{\text{bend}}$ (kcal/mol/rad $^2$ )	source
CH <sub>2</sub>	CH <sub>2</sub>	S	114.0	124.20	Ref. [4]
CH <sub>3</sub>	CH <sub>2</sub>	CH <sub>2</sub>	114.0	124.20	Ref. [4]
CH <sub>2</sub>	CH <sub>2</sub>	CH <sub>2</sub>	114.0	124.20	Ref. [4]
CHene	CHene	CH <sub>3</sub>	119.7	139.94	Ref. [3]
CHene	CHene	CH <sub>2</sub>	119.7	139.94	Ref. [3]
CH <sub>2</sub>	CH <sub>2</sub>	CHene	114.0	124.20	Ref. [3]
Char	Char	Char	120.0	126.0	Refs. [3] and [92]
Char	Char	CH <sub>2</sub>	120.0	140.0	Refs. [3] and [92]
Char	Char	CH <sub>3</sub>	120.0	140.0	Refs. [3] and [92]
Char	Char	CH <sub>2</sub> ar	120.0	126.0	Refs. [3] and [92]
S	CH <sub>2</sub>	CHene	109.97	127.37	This work
S	CH <sub>2</sub>	Char	109.97	127.37	This work
S	Char	Char	123.911	138.093	This work

TABLE 2.4

The central atoms for each torsion are atoms  $j$  and  $k$ , and wildcard atom types are denoted by “X”. All  $c_n$  parameters have units of kcal/mol. The torsions around carbon-carbon double bonds are harmonic and assume a trans ( $180^\circ$ ) geometry. The force constant for this torsion is given in

$$\text{kcal mol}^{-1}\text{degrees}^{-2}.$$

$i$	$j$	$k$	$l$	$c_0$	$c_1$	$c_2$	$c_3$	source
CH <sub>3</sub>	CH <sub>2</sub>	CH <sub>2</sub>	CH <sub>2</sub>	0.0	0.7055	-0.13551	1.5725	Ref. [2]
CH <sub>2</sub>	CH <sub>2</sub>	CH <sub>2</sub>	CH <sub>2</sub>	0.0	0.7055	-0.13551	1.5725	Ref. [2]
CH <sub>2</sub>	CH <sub>2</sub>	CH <sub>2</sub>	S	0.0	0.7055	-0.13551	1.5725	Ref. [4]
X	CHene	CHene	X	$V = \frac{0.008112}{2}(\phi - 180.0)^2$				Ref. [3]
X	Char	Char	X					
CH <sub>2</sub>	CH <sub>2</sub>	CHene	CHene	1.368	0.1716	-0.2181	-0.56081	Ref. [3]
CH <sub>2</sub>	CH <sub>2</sub>	CH <sub>2</sub>	CHene	0.0	0.7055	-0.13551	1.5725	Ref. [3]
CHene	CHene	CH <sub>2</sub>	S	3.20753	0.207417	-0.912929	-0.958538	This work
Char	Char	CH <sub>2</sub>	S	3.20753	0.207417	-0.912929	-0.958538	This work

### 2.3.4 Simulation Protocol

Gold nanospheres with radii ranging from 10 - 25 Å were created from a bulk fcc lattice and were thermally equilibrated prior to the addition of ligands. A 50% coverage of ligands (based on coverages reported by Badia, *et al.*[87]) was placed on the surface of the equilibrated nanoparticles using Packmol[97]. Three lengths for the straight-chain ligands,  $C_4$ ,  $C_8$ , and  $C_{12}$ , differentiated by the number of carbons in the chains are used in this study. Additionally, to explore the effects of ligand flexibility, three levels of ligand “stiffness” are examined. The most flexible chain is a fully saturated alkanethiolate, while moderate rigidity is introduced using an alkene thiolate with one double bond in the penultimate (solvent-facing) carbon-carbon location. The most rigid ligands are fully-conjugated chains where all of the carbons are represented with conjugated (aryl) united-atom carbon atoms (CHar or terminal  $\text{CH}_2\text{ar}$ ).

The nanoparticle / ligand complexes were thermally equilibrated to allow for ligand conformational flexibility. Packmol was then used to solvate the structures inside a spherical droplet of hexane. The thickness of the solvent layer was chosen to be at least  $1.5 \times$  the combined radius of the nanoparticle / ligand structure. The fully solvated system was equilibrated for at least 1 ns using the “Langevin Hull” algorithm to apply 50 atm of pressure and a target temperature of 250 K.[1] Typical system sizes ranged from 18,310 united atom sites for the 10 Å particles with  $C_4$  ligands to 89,490 sites for the 25 Å particles with  $C_{12}$  ligands. Figure 2.2 shows one of the solvated 25 Å nanoparticles passivated with the  $C_{12}$  alkane thiolate ligands.

Once equilibrated, thermal fluxes were applied for 1 ns, until stable temperature gradients had developed (see Figure 2.3). Systems were run under moderate pressure (50 atm) with an average temperature (250K) that maintained a compact solvent cluster and avoided formation of a vapor layer near the heated metal surface. Pressure was applied to the system via the non-periodic “Langevin Hull” algorithm.[1]

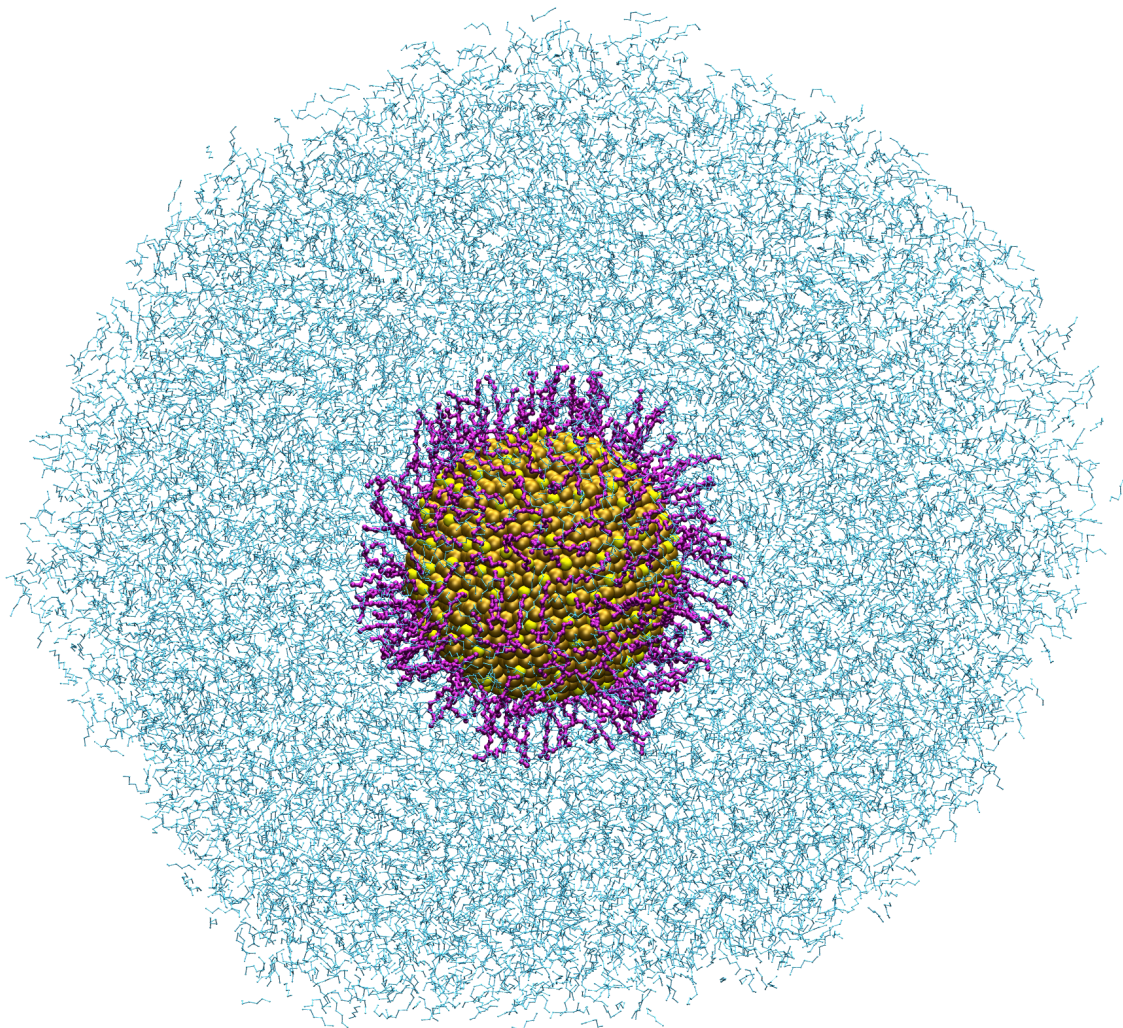


Figure 2.2. A  $25 \text{ \AA}$  radius gold nanoparticle protected with a half-monolayer of TraPPE-UA dodecanethiolate ( $\text{C}_{12}$ ) ligands and solvated in TraPPE-UA hexane. The interfacial thermal conductance is computed by applying a kinetic energy flux between the nanoparticle and an outer shell of solvent.

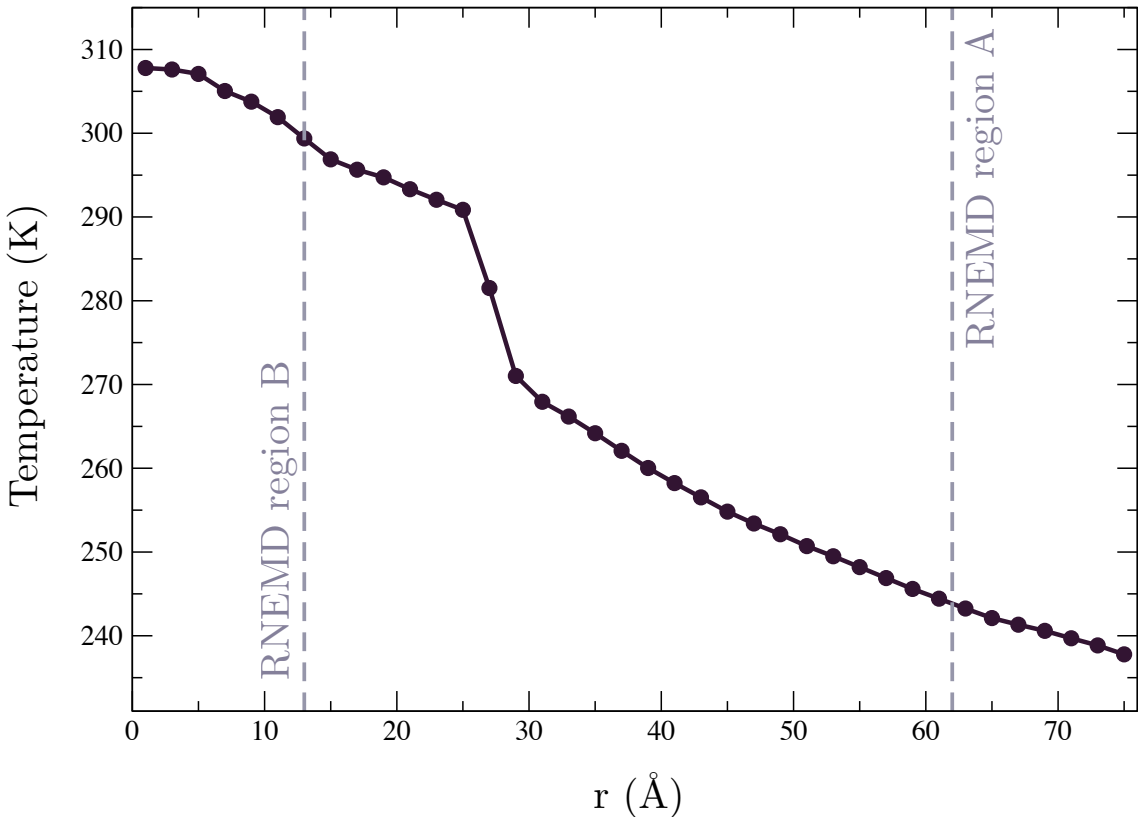


Figure 2.3. Radial temperature profile for a 25 Å radius particle protected with a 50% coverage of TraPPE-UA butanethiolate ( $C_4$ ) ligands and solvated in TraPPE-UA hexane. A kinetic energy flux is applied between RNEMD region A and RNEMD region B. The size of the temperature discontinuity at the interface is governed by the interfacial thermal conductance.

However, thermal coupling to the external temperature bath was removed to avoid interference with the imposed RNEMD flux.

Although the VSS-RNEMD moves conserve *total* angular momentum and energy, systems which contain a metal nanoparticle embedded in a significant volume of solvent will still experience nanoparticle diffusion inside the solvent droplet. To aid in measuring an accurate temperature profile for these systems, a single gold atom at the origin of the coordinate system was assigned a mass  $10,000 \times$  its original mass. The bonded and nonbonded interactions for this atom remain unchanged and the heavy

atom is excluded from the RNEMD velocity scaling. The only effect of this gold atom is to effectively pin the nanoparticle at the origin of the coordinate system, thereby preventing translational diffusion of the nanoparticle due to Brownian motion.

To provide statistical independence, five separate configurations were simulated for each particle radius and ligand. The structures were unique, starting at the point of ligand placement, in order to sample multiple surface-ligand configurations.

## 2.4 Results

Four sizes of nanoparticles ( $R = 10, 15, 20,$  and  $25 \text{ \AA}$ ) were modelled. The smallest particle size produces the lowest interfacial thermal conductance values for most of the protecting groups (Figure 2.4). Between the other three sizes of nanoparticles, there is no systematic dependence of the interfacial thermal conductance on the nanoparticle size. It is likely that the differences in local curvature of the nanoparticle sizes studied here do not disrupt the ligand packing and behavior in drastically different ways.

Unlike a previous study of varying thiolate ligand chain lengths on planar Au(111) surfaces, the interfacial thermal conductance of ligand-protected nanospheres exhibits a distinct dependence on the ligand identity.[57] A half-monolayer coverage of ligands yields interfacial conductance that is strongly dependent on both ligand length and flexibility.

There are many factors that could be playing a role in the ligand-dependent conductance. The sulfur-gold interaction is particularly strong, and the presence of the ligands can easily disrupt the crystalline structure of the gold at the surface of the particles, providing more efficient scattering of phonons into the ligand / solvent layer. This effect would be particularly important at small particle sizes.

In previous studies of mixed-length ligand layers with full coverage, Stocker *et al.* observed that ligand-solvent alignment was an important factor for heat transfer

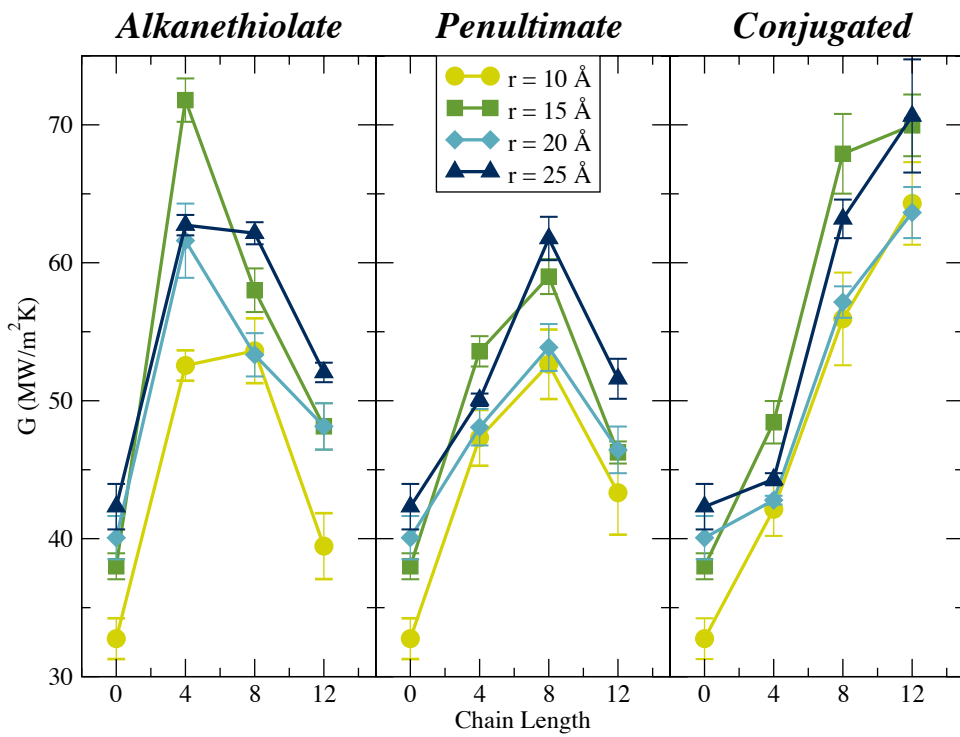


Figure 2.4. Interfacial thermal conductance ( $G$ ) values for 4 sizes of solvated nanoparticles that are bare or protected with a 50% coverage of C<sub>4</sub>, C<sub>8</sub>, or C<sub>12</sub> thiolate ligands. Ligands of different flexibility are shown in separate panels. The middle panel indicates ligands which have a single carbon-carbon double bond in the penultimate position.

into the solvent.[57] With high surface curvature and lower effective coverages, ligand behavior also becomes more complex. Some chains may be lying down on the surface, and solvent may not be penetrating the ligand layer to the same degree as in the planar surfaces.

Additionally, the ligand flexibility directly alters the vibrational density of states for the layer that mediates the transfer of phonons between the metal and the solvent. This could be a partial explanation for the observed differences between the fully conjugated and more flexible ligands.

The following sections provide details on how surface corrugation, solvent-ligand interpenetration, and ordering of the solvent and ligand at the surfaces of the nanospheres are measured. This is followed by an investigation of the overlap between vibrational densities of states for the various ligands.

#### 2.4.1 Corrugation of the Particle Surface

The bonding sites for thiols on gold surfaces have been studied extensively and include configurations beyond the traditional atop, bridge, and hollow sites found on planar surfaces. In particular, the deep potential well between the gold atoms and the thiolate sulfur atoms leads to insertion of the sulfur into the gold lattice and displacement of interfacial gold atoms. The degree of ligand-induced surface restructuring may have an impact on the interfacial thermal conductance and is an important phenomenon to quantify.

Henz, *et al.*[86] used the metal density as a function of radius to measure the degree of mixing between the thiol sulfurs and surface gold atoms at the edge of a nanoparticle. Although metal density is important, disruption of the local crystalline ordering would also have a large effect on the phonon spectrum in the particles. To measure this effect, the fraction of gold atoms exhibiting local fcc ordering as a function of radius to describe the ligand-induced disruption of the nanoparticle

surface is used.

The local bond orientational order can be described using the method of Steinhardt *et al.*[98] The local bonding environment,  $\bar{q}_{\ell m}$ , for each atom in the system is determined by averaging over the spherical harmonics between that atom and each of its neighbors,

$$\bar{q}_{\ell m} = \sum_i Y_{\ell}^m(\theta_i, \phi_i) \quad (2.10)$$

where  $\theta_i$  and  $\phi_i$  are the relative angular coordinates of neighbor  $i$  in the laboratory frame. A global average orientational bond order parameter,  $\bar{Q}_{\ell m}$ , is the average over each  $\bar{q}_{\ell m}$  for all atoms in the system. To remove the dependence on the laboratory coordinate frame, the third order rotationally invariant combination of  $\bar{Q}_{\ell m}$ ,  $\hat{w}_{\ell}$ , is utilized here.[98, 99]

For  $\ell = 4$ , the ideal face-centered cubic (fcc), body-centered cubic (bcc), hexagonally close-packed (hcp), and simple cubic (sc) local structures exhibit  $\hat{w}_4$  values of -0.159, 0.134, 0.159, and 0.159, respectively. Because  $\hat{w}_4$  exhibits an extreme value for fcc structures, it is ideal for measuring local fcc ordering. The spatial distribution of  $\hat{w}_4$  local bond orientational order parameters,  $p(\hat{w}_4, r)$ , can provide information about the location of individual atoms that are central to local fcc ordering.

The fraction of fcc-ordered gold atoms at a given radius in the nanoparticle,

$$f_{\text{fcc}}(r) = \int_{-\infty}^{w_c} p(\hat{w}_4, r) d\hat{w}_4 \quad (2.11)$$

is described by the distribution of the local bond orientational order parameters,  $p(\hat{w}_4, r)$ , and  $w_c$ , a cutoff for the peak  $\hat{w}_4$  value displayed by fcc structures. A  $w_c$  value of -0.12 was chosen to isolate the fcc peak in  $\hat{w}_4$ .

As illustrated in Figure 2.5, the presence of ligands decreases the fcc ordering of the gold atoms at the nanoparticle surface. For the smaller nanoparticles, this disruption extends into the core of the nanoparticle, indicating widespread disruption

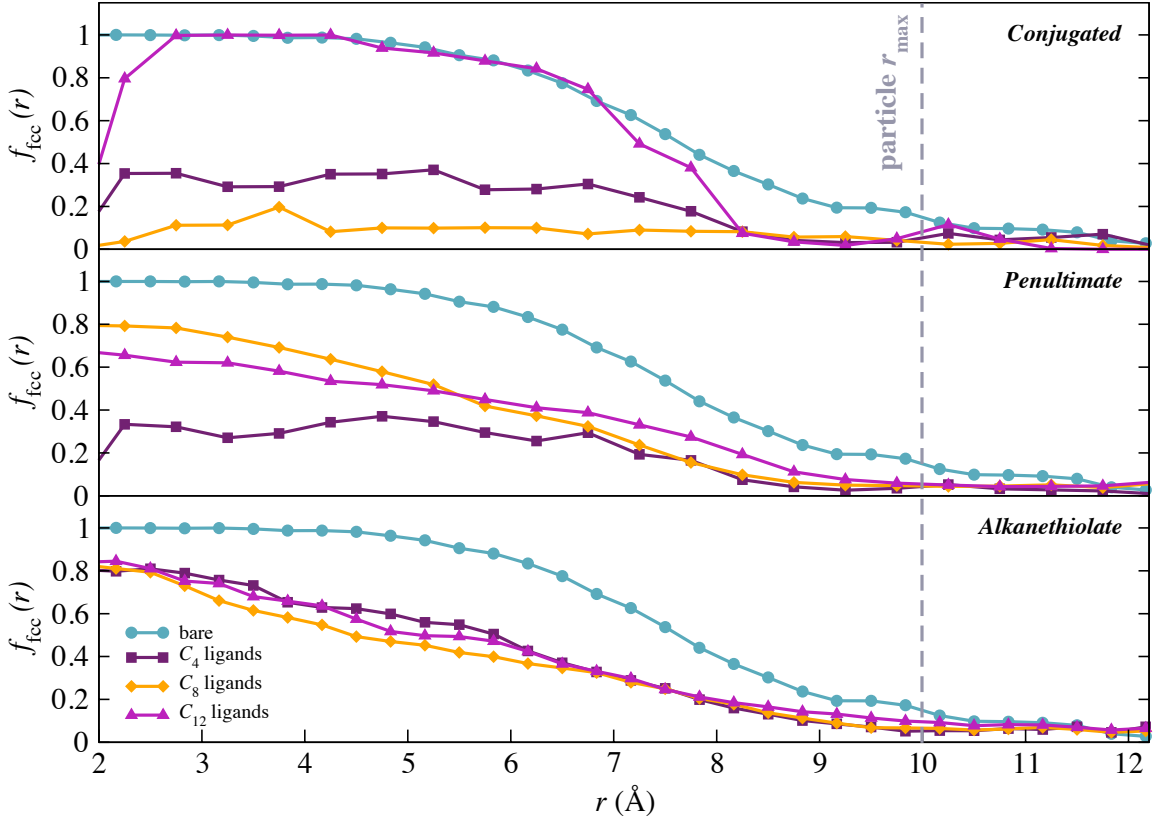


Figure 2.5. Fraction of gold atoms with fcc ordering as a function of radius for a 10 Å radius nanoparticle. The decreased fraction of fcc-ordered atoms in ligand-protected nanoparticles relative to bare particles indicates restructuring of the nanoparticle surface by the thiolate sulfur atoms.

of the lattice.

The thickness of the disrupted nanoparticle surface can be described by defining a corrugation factor,  $c$ , as the ratio of the radius at which the fraction of gold atoms with fcc ordering is 0.9 and the radius at which the fraction is 0.5.

$$c = 1 - \frac{r(f_{\text{fcc}} = 0.9)}{r(f_{\text{fcc}} = 0.5)} \quad (2.12)$$

A sharp interface will have a steep drop in  $f_{\text{fcc}}$  at the edge of the particle ( $c \rightarrow 0$ ). In the opposite limit where the entire nanoparticle surface is restructured by ligands, the radius at which there is a high probability of fcc ordering moves dramatically

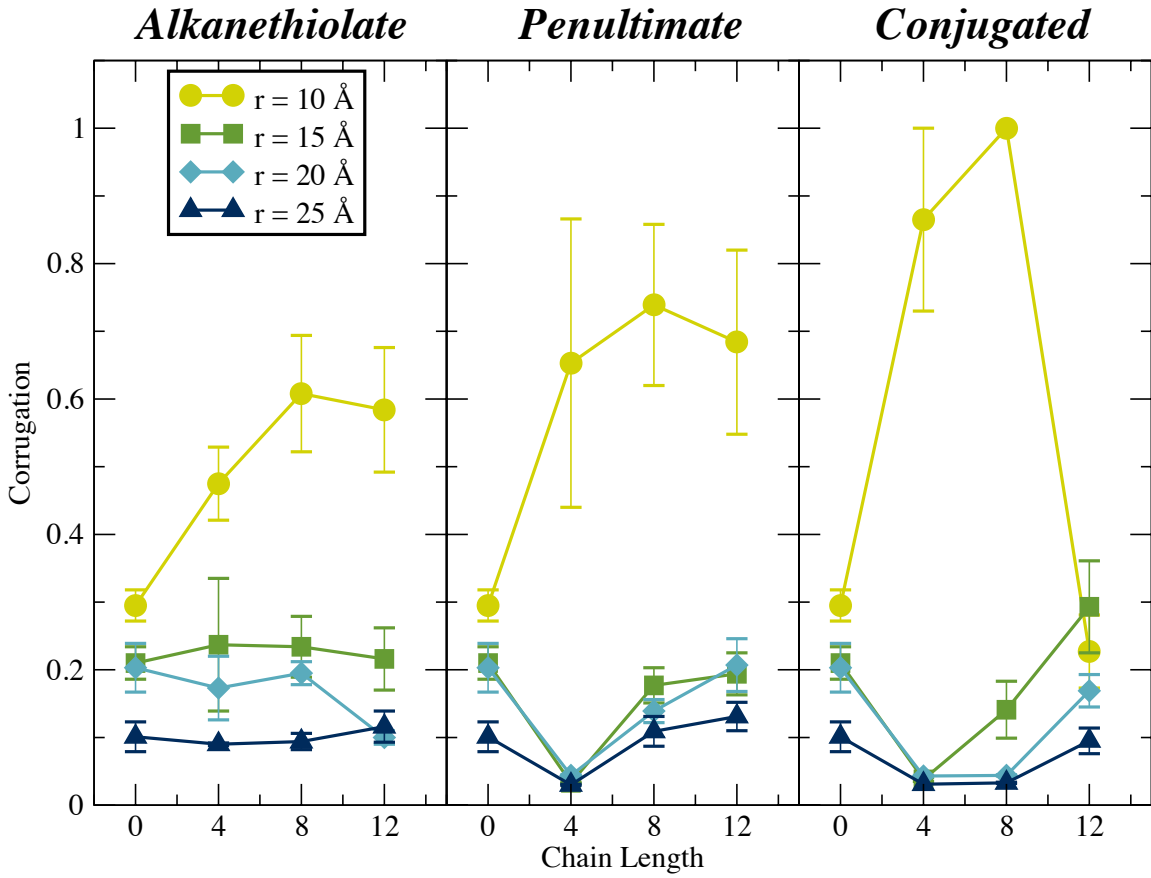


Figure 2.6. Computed corrugation values for 4 sizes of solvated nanoparticles that are bare or protected with a 50% coverage of C<sub>4</sub>, C<sub>8</sub>, or C<sub>12</sub> thiolate ligands. The smallest (10 Å) particles show significant disruption to their crystal structures, and the length and stiffness of the ligands is a contributing factor to the surface disruption.

inward ( $c \rightarrow 1$ ).

The computed corrugation factors are shown in Figure 2.6 for bare nanoparticles and for ligand-protected particles as a function of ligand chain length. The largest nanoparticles are only slightly restructured by the presence of ligands on the surface, while the smallest particle ( $r = 10\text{ \AA}$ ) exhibits significant disruption of the original fcc ordering when covered with a half-monolayer of thiol ligands.

Since the thiolate ligands do not significantly alter the larger particle crystallinity, the surface corrugation does not seem to be a likely candidate to explain the large

increase in thermal conductance at the interface when ligands are added.

#### 2.4.2 Orientation of Ligand Chains

Previous theoretical work on heat conduction through alkane chains has shown that short chains are dominated by harmonic interactions, where the energy is carried ballistically through the chain.[100] As the saturated ligand chain length increases in length, it exhibits significantly more conformational flexibility. Thus, different lengths of ligands should favor different chain orientations on the surface of the nanoparticle, and can localize the ligand vibrational density of states close to the particle, lowering the effectiveness of the heat conduction.[100] To determine the distribution of ligand orientations relative to the particle surface the probability of finding a ligand with a particular orientation relative to the surface normal of the nanoparticle is examined,

$$\cos(\theta) = \frac{\vec{r}_i \cdot \hat{u}_i}{|\vec{r}_i| |\hat{u}_i|} \quad (2.13)$$

where  $\vec{r}_i$  is the vector between the cluster center of mass and the sulfur atom on ligand molecule  $i$ , and  $\hat{u}_i$  is the vector between the sulfur atom and  $\text{CH}_3$  pseudo-atom on ligand molecule  $i$ . As depicted in Figure 2.7,  $\theta \rightarrow 180^\circ$  for a ligand chain standing upright on the particle ( $\cos(\theta) \rightarrow -1$ ) and  $\theta \rightarrow 90^\circ$  for a ligand chain lying down on the surface ( $\cos(\theta) \rightarrow 0$ ). As the thiolate alkane chain increases in length and becomes more flexible, the ligands are more willing to lie down on the nanoparticle surface and exhibit increased population at  $\cos(\theta) = 0$ .

An order parameter describing the average ligand chain orientation relative to the nanoparticle surface is available using the second order Legendre parameter,

$$P_2 = \left\langle \frac{1}{2} (3 \cos^2(\theta) - 1) \right\rangle. \quad (2.14)$$

Ligand populations that are perpendicular to the particle surface have  $P_2$  values

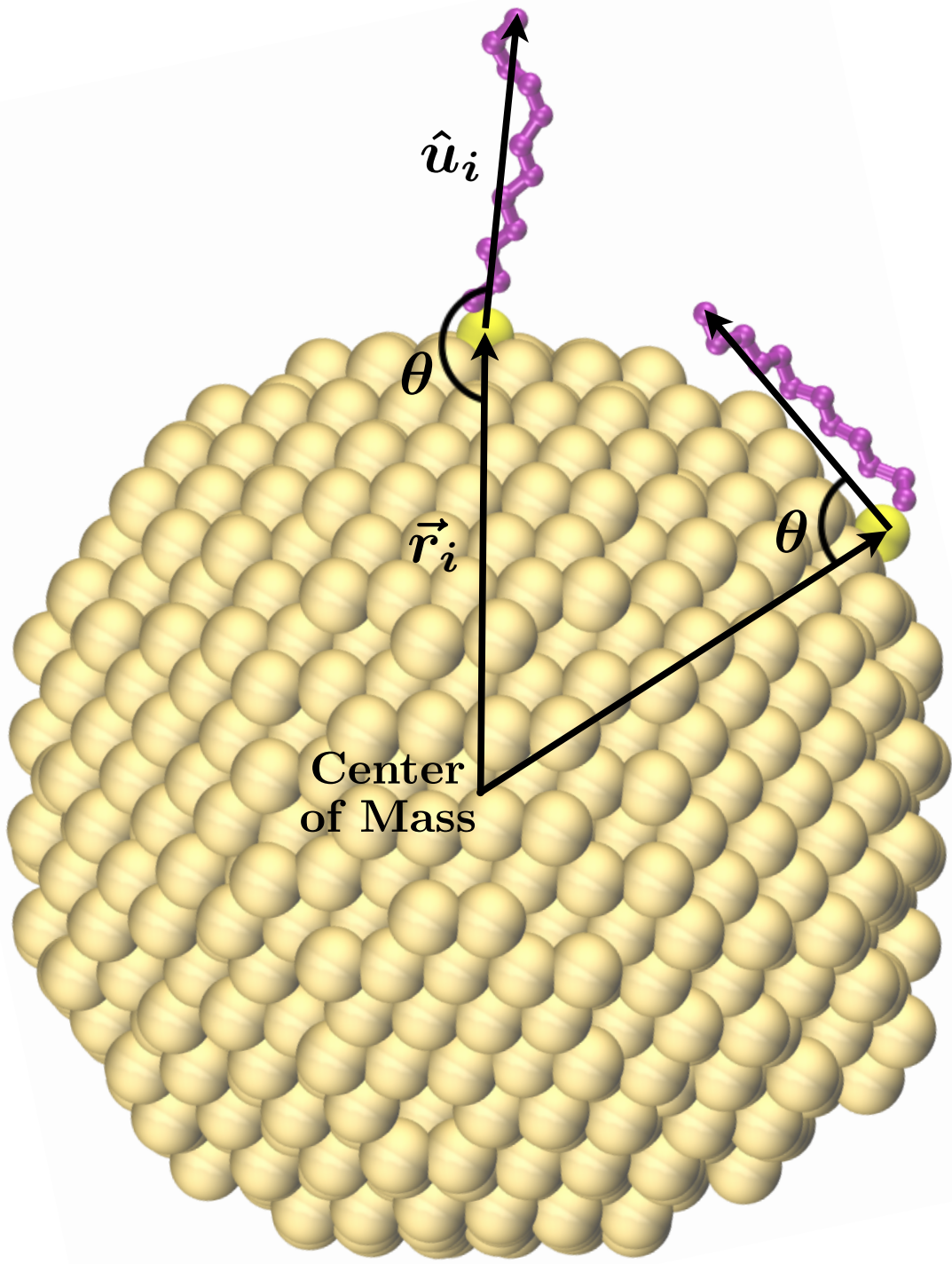


Figure 2.7. The two extreme cases of ligand orientation relative to the nanoparticle surface: the ligand completely outstretched ( $\cos(\theta) = -1$ ) and the ligand fully lying down on the particle surface ( $\cos(\theta) = 0$ ).

of 1, while ligand populations lying flat on the nanoparticle surface have  $P_2$  values of  $-0.5$ . Disordered ligand layers will exhibit mean  $P_2$  values of 0. As shown in Figure 2.8 the ligand  $P_2$  values approaches 0 as ligand chain length – and ligand flexibility – increases.

#### 2.4.3 Orientation of Interfacial Solvent

Similarly, the distribution of *hexane* molecule orientations relative to the particle surface using the same angular analysis utilized for the ligand chain orientations was examined. In this case,  $\vec{r}_i$  is the vector between the particle center of mass and one of the  $\text{CH}_2$  pseudo-atoms in the middle of hexane molecule  $i$  and  $\hat{u}_i$  is the vector between the two  $\text{CH}_3$  pseudo-atoms on molecule  $i$ . Since only the orientation of solvent molecules near the ligand layer is of interest, only the hexane molecules that reside between the edge of the particle and the end of the ligand chains are selected. A large population of hexane molecules with  $\cos(\theta) \sim \pm 1$  would indicate interdigitation of the solvent molecules between the upright ligand chains. A more random distribution of  $\cos(\theta)$  values indicates a disordered arrangement of solvent molecules near the particle surface. Again,  $P_2$  order parameter values provide a population analysis for the solvent that is close to the particle surface.

The average orientation of the interfacial solvent molecules is notably flat on the *bare* nanoparticle surfaces. This blanket of hexane molecules on the particle surface may act as an insulating layer, increasing the interfacial thermal resistance. As the length (and flexibility) of the ligand increases, the average interfacial solvent  $P_2$  value approaches 0, indicating a more random orientation of the ligand chains. The average orientation of solvent within the  $C_8$  and  $C_{12}$  ligand layers is essentially random. Solvent molecules in the interfacial region of  $C_4$  ligand-protected nanoparticles do not lie as flat on the surface as in the case of the bare particles, but are not as randomly oriented as the longer ligand lengths.

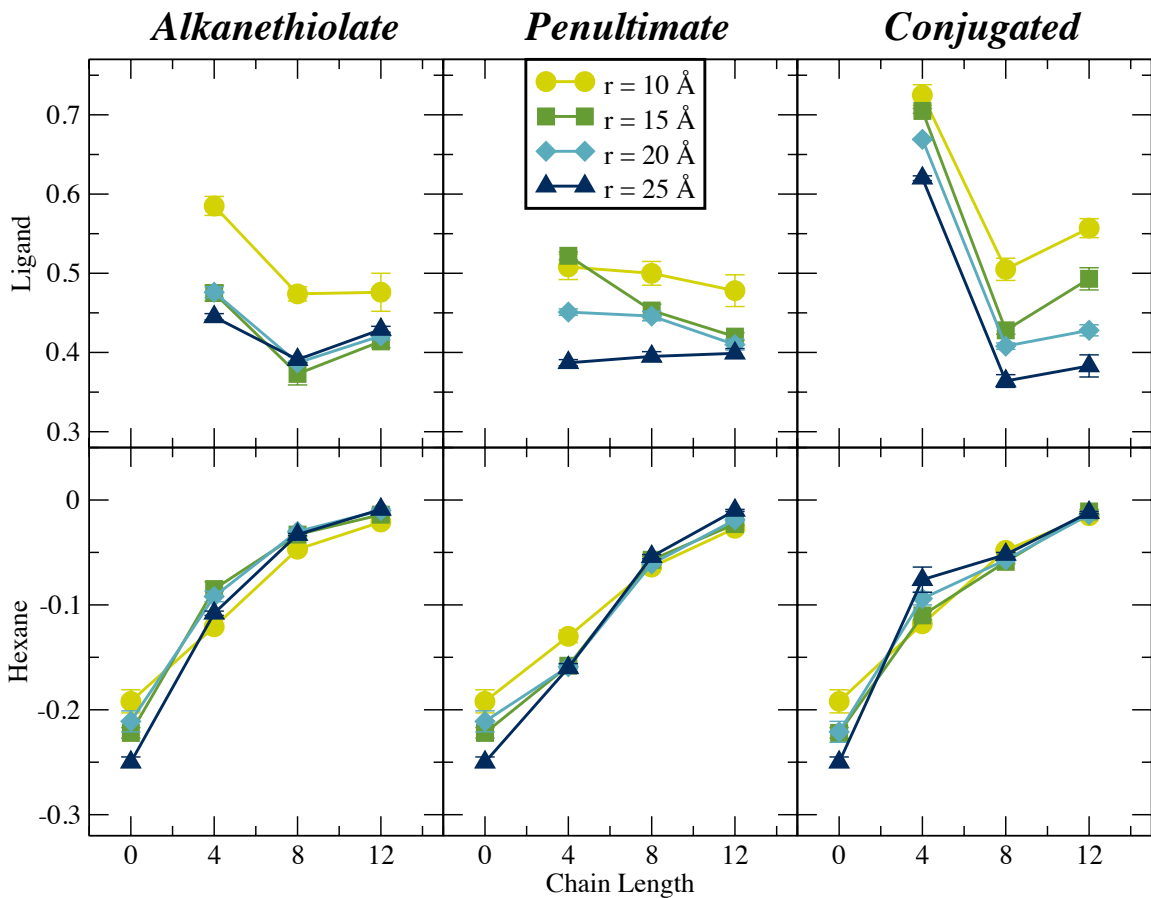


Figure 2.8. Computed ligand and interfacial solvent orientational  $P_2$  values for 4 sizes of solvated nanoparticles that are bare or protected with a 50% coverage of  $C_4$ ,  $C_8$ , or  $C_{12}$  alkanethiolate ligands. Increasing stiffness of the ligand orients these molecules normal to the particle surface, while the length of the ligand chains works to prevent solvent from lying flat on the surface.

These results are particularly interesting in light of previous work by Stocker *et al*[57], where solvent molecules readily filled the vertical gaps between neighboring ligand chains and there was a strong correlation between ligand and solvent molecular orientations. It appears that the introduction of surface curvature and a lower ligand packing density creates a disordered ligand layer that lacks well-formed channels for the solvent molecules to occupy.

#### 2.4.4 Solvent Penetration of Ligand Layer

The extent of ligand – solvent interaction is also determined by the degree to which these components occupy the same region of space adjacent to the nanoparticle. The radial density profiles of these components help determine this degree of interaction. Figure 2.9 shows representative density profiles for solvated 25 Å radius nanoparticles with no ligands, and with a 50% coverage of C<sub>4</sub>, C<sub>8</sub>, and C<sub>12</sub> thiolates.

The differences between the radii at which the hexane surrounding the ligand-covered particles reaches bulk density correspond nearly exactly to the differences between the lengths of the ligand chains. Beyond the edge of the ligand layer, the solvent reaches its bulk density within a few angstroms. The differing shapes of the density curves indicate that the solvent is increasingly excluded from the ligand layer as the chain length increases.

The conjugated ligands create a distinct solvent shell within the ligand layer and also allow significantly more solvent to penetrate close to the particle. A density overlap parameter can be defined,

$$O_{l-s} = \frac{1}{V} \int_0^{r_{\max}} 4\pi r^2 \frac{4\rho_l(r)\rho_s(r)}{(\rho_l(r) + \rho_s(r))^2} dr \quad (2.15)$$

where  $\rho_l(r)$  and  $\rho_s(r)$  are the ligand and solvent densities at a radius  $r$ , and  $V$  is the total integration volume ( $V = 4\pi r_{\max}^3/3$ ). The fraction in the integrand is a

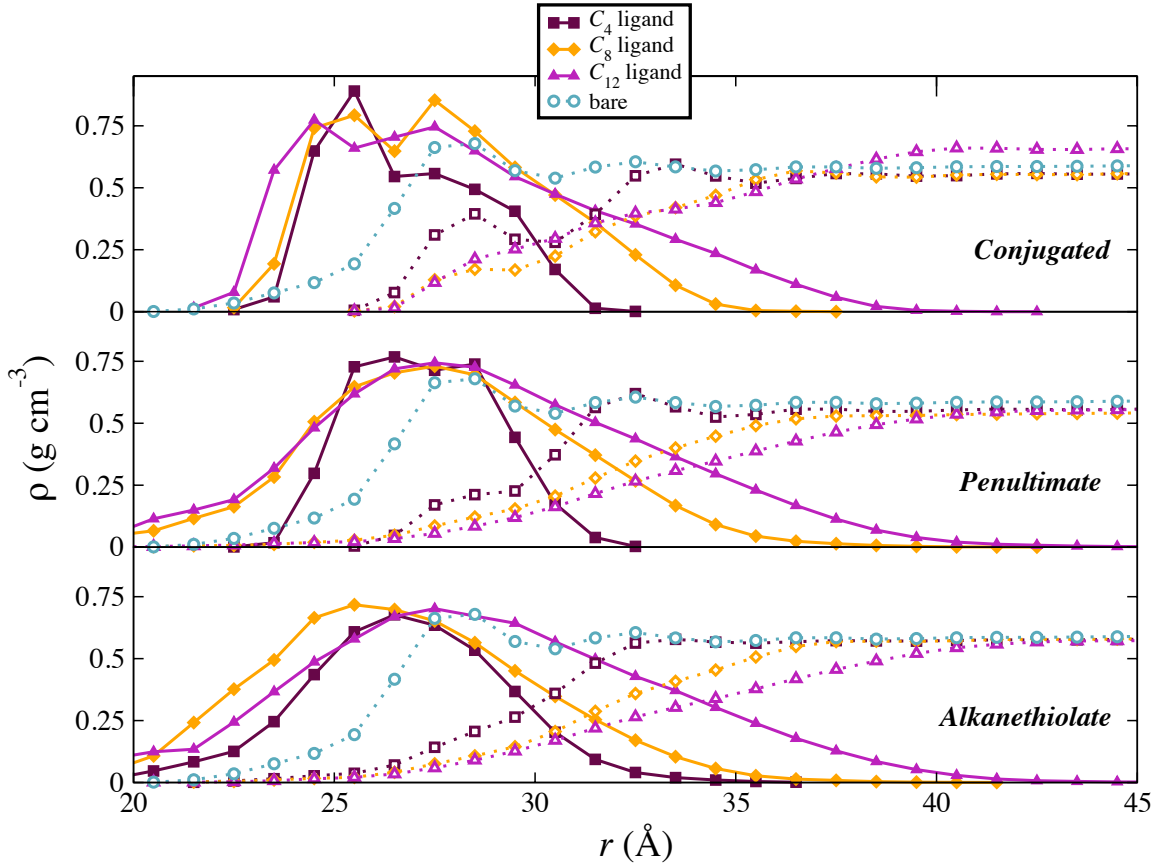


Figure 2.9. Radial density profiles for 25 Å radius nanoparticles with no ligands (circles),  $C_4$  ligands (squares),  $C_8$  ligands (diamonds), and  $C_{12}$  ligands (triangles). Ligand density is indicated with filled symbols, solvent (hexane) density is indicated with open symbols. As ligand chain length increases, the nearby solvent is excluded from the ligand layer. The conjugated ligands (upper panel) can create a separated solvent shell within the ligand layer and also allow significantly more solvent to penetrate close to the particle.

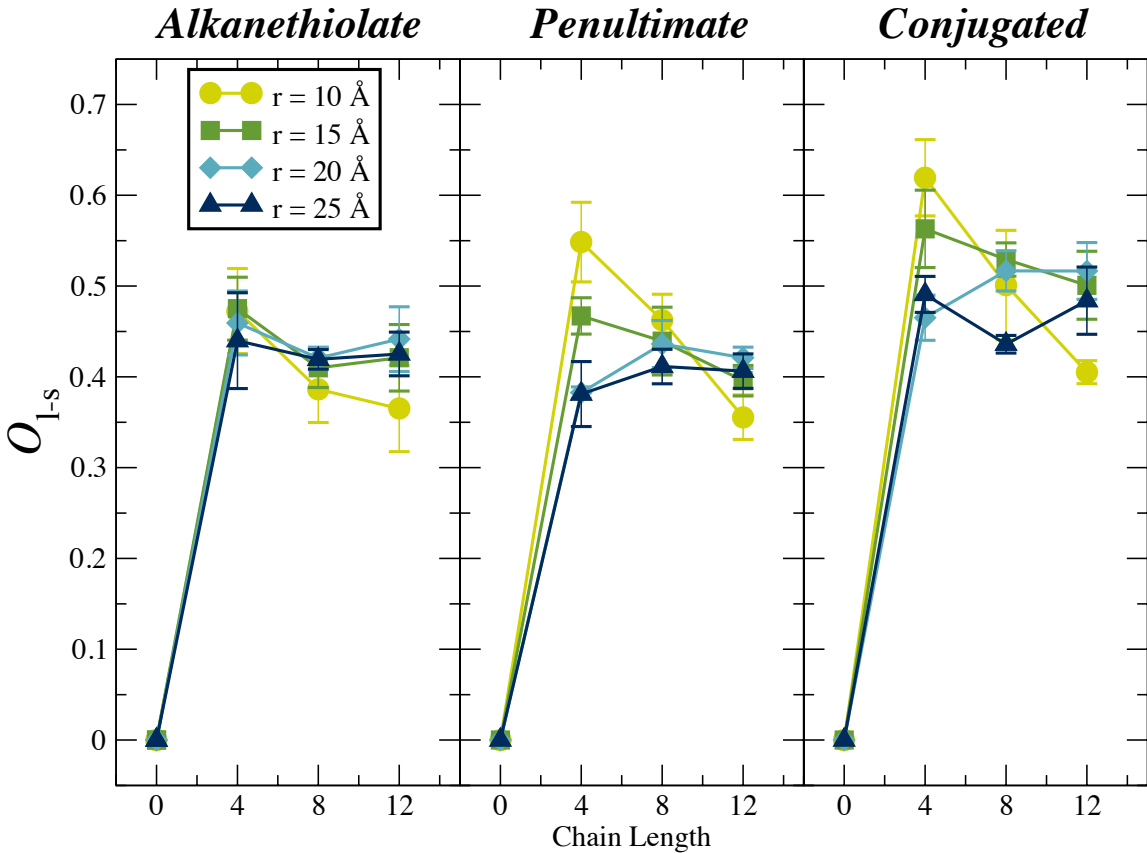


Figure 2.10. Density overlap parameters ( $O_{l-s}$ ) for solvated nanoparticles protected by thiolate ligands. In general, the rigidity of the fully-conjugated ligands provides the easiest route for solvent to enter the interfacial region. Additionally, shorter chains allow a greater degree of solvent penetration of the ligand layer.

dimensionless quantity that is unity when ligand and solvent densities are identical at radius  $r$ , but falls to zero when either of the two components are excluded from that region.

The density overlap parameters are shown in Figure 2.10. The calculated overlap parameters indicate that the conjugated ligand allows for the most solvent penetration close to the particle, and that shorter chains generally permit greater solvent penetration in the interfacial region. Increasing overlap can certainly allow for enhanced thermal transport, but this is clearly not the only contributing factor. Even

when the solvent and ligand are in close physical contact, there must also be good vibrational overlap between the phonon densities of states in the ligand and solvent to transmit vibrational energy between the two materials.

#### 2.4.5 Ligand-mediated Vibrational Overlap

In phonon scattering models for interfacial thermal conductance,[19, 20, 80, 101, 102] the frequency-dependent transmission probability ( $t_{a \rightarrow b}(\omega)$ ) predicts phonon transfer between materials  $a$  and  $b$ . Many of the models for interfacial phonon transmission estimate this quantity using the phonon density of states and group velocity, and make use of a Debye model for the density of states in the solid.

A consensus picture is that in order to transfer the energy carried by an incoming phonon of frequency  $\omega$  on the  $a$  side, the phonon density of states on the  $b$  side must have a phonon of the same frequency. The overlap of the phonon densities of states, particularly at low frequencies, therefore contributes to the transfer of heat. Phonon scattering must be done in a direction perpendicular to the interface. In the geometries described here, there are two interfaces (particle  $\rightarrow$  ligand, and ligand  $\rightarrow$  solvent), and the vibrational overlap between the ligand and the other two components is relevant to heat transfer.

To estimate the relevant densities of states, the velocity of each atom  $i$  in the region of the interface is projected onto a direction normal to the interface. For the nanosphere geometries studied here, the normal direction depends on the instantaneous position of the atom relative to the center of mass of the particle.

$$v_{\perp}(t) = \mathbf{v}(t) \cdot \frac{\mathbf{r}(t)}{|\mathbf{r}(t)|} \quad (2.16)$$

The quantity  $v_{\perp}(t)$  measures the instantaneous velocity of an atom in a direction perpendicular to the nanoparticle interface. In the interfacial region, the autocorrelation

function of these velocities,

$$C_{\perp}(t) = \langle v_{\perp}(t) \cdot v_{\perp}(0) \rangle, \quad (2.17)$$

will include contributions from all of the phonon modes present at the interface. The Fourier transform of the time-symmetrized autocorrelation function provides an estimate of the vibrational density of states,[103]

$$\rho(\omega) = \frac{1}{\tau} \int_{-\tau/2}^{\tau/2} C_{\perp}(t) e^{-i\omega t} dt. \quad (2.18)$$

Here  $\tau$  is the total observation time for the autocorrelation function. In Figure 2.11 shows the low-frequency region of the normalized vibrational densities of states for the three chemical components (gold nanoparticle,  $C_{12}$  ligands, and interfacial solvent). The double bond in the penultimate location is a small perturbation on ligands of this size, and that is reflected in relatively similar spectra in the lower panels. The fully conjugated ligand, however, shifts the peak in the lowest frequency band from  $\sim 29\text{cm}^{-1}$  to  $\sim 55\text{cm}^{-1}$ , yielding significant overlap with the density of states in the nanoparticle. This ligand increases the overlap with the solvent density of states in a band between 280 and 380  $\text{cm}^{-1}$ . This provides some physical basis for the high interfacial conductance observed for the fully conjugated  $C_8$  and  $C_{12}$  ligands.

The similarity between the density of states for the alkanethiolate and penultimate ligands explains why the interfacial conductance is nearly the same for these two ligands, particularly at longer chain lengths.

## 2.5 Discussion

The chemical bond between the metal and the ligand introduces vibrational overlap that is not present between the bare metal surface and solvent. Thus, regardless

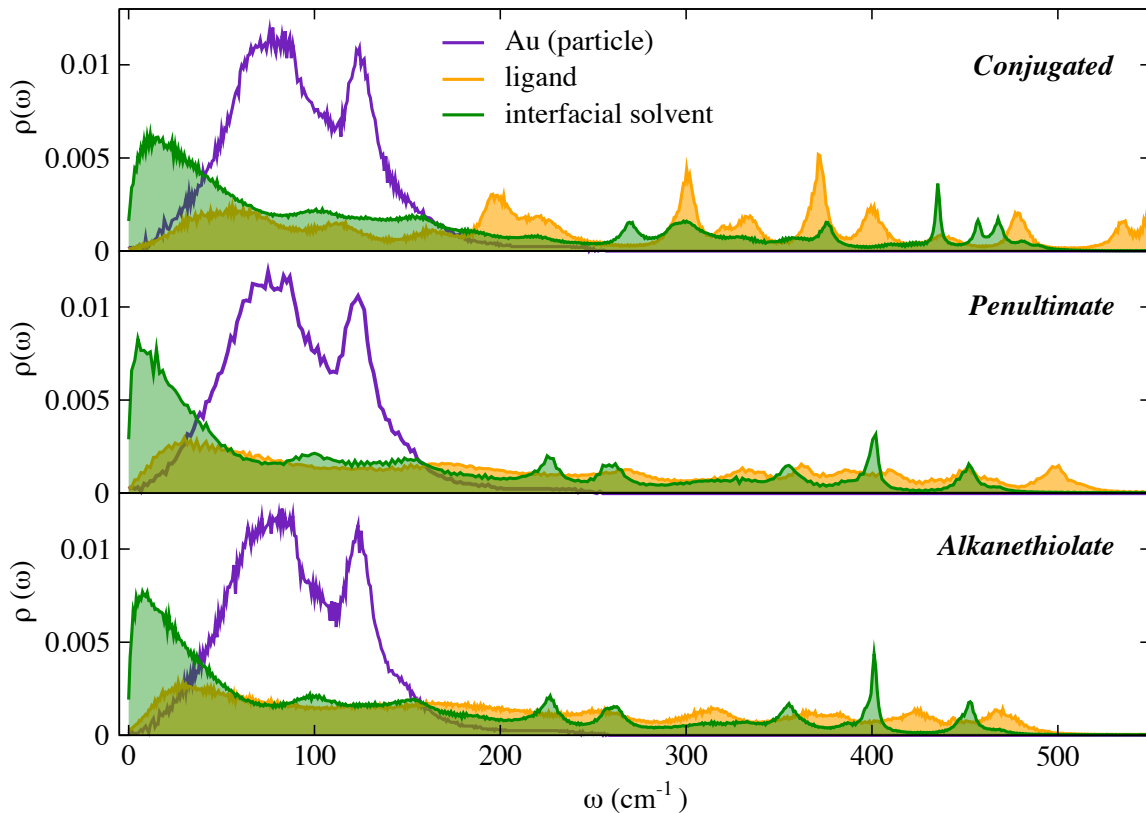


Figure 2.11. The low frequency portion of the vibrational density of states for three chemical components (gold nanoparticles,  $\text{C}_{12}$  ligands, and hexane solvent). These densities of states were computed using the velocity autocorrelation functions for atoms in the interfacial region, constructed with velocities projected onto a direction normal to the interface.

of ligand identity or chain length, the presence of a half-monolayer ligand coverage yields a higher interfacial thermal conductance value than the bare nanoparticle. The mechanism for the varying conductance for the different ligands is somewhat less clear. Ligand-based alterations to vibrational density of states is a major contributor, but some of the ligands can disrupt the crystalline structure of the smaller nanospheres, while others can re-order the interfacial solvent and alter the interpenetration profile between ligand and solvent chains. Further work to separate the effects of ligand-solvent interpenetration and surface reconstruction is clearly needed for a complete picture of the heat transport in these systems.

## CHAPTER 3

### THERMAL TRANSPORT IS INFLUENCE BY NANOPARTICLE SHAPE

#### 3.1 Introduction

Thermal transport between nanoparticles and their surrounding environments depends on many factors, including particle size,[59–63] composition,[64, 65, 74] surface modification,[60, 62, 65–70, 74, 104] surface supports,[71, 105] exposed surface facets,[68, 106, 107] and the chemical details of the environment.[61, 65, 67, 69, 71, 72, 105, 108–110] Particle morphology may also play a role in heat transfer out of nanostructures. This is the central question of this chapter – all other things being equal, will different particle morphologies yield different heat transfer properties to the solvent?

Tascini *et al.*[63] studied the curvature dependence of the interfacial thermal conductance for partially solvated nanospheres. They found an empirical relationship,

$$G(r) = G(\infty) + \frac{\delta}{r} \quad (3.1)$$

where  $G(r)$  is the conductance out of a sphere of radius  $r$ ,  $G(\infty)$  is a parameter describing the infinite-radius limit of the conductance, and  $\delta$  describes the approach to the infinite size limit. Notably, the Tascini *et al.* simulations predict a positive  $\delta$ , where smaller particles exhibit high interfacial thermal conductance and approach an infinite surface limit that has lower thermal conductance to the solvent. This makes intuitive sense – one might expect the large particle limit to approach the behavior of flat interfaces.

To test this hypothesis, heat transfer out of gold nanospheres that were in direct contact with a molecular solvent have been computed. The spheres were cut out of an infinite FCC lattice and spanned a range of sizes. The spheres expose many surface facets including patches of the (111), (100), and (110) facets, due to the cuts in the underlying FCC lattice. The interfacial thermal conductance out of similarly-sized icosahedral particles that exhibit only (111) facets and cuboctahedral particles that display only (111) and (100) facets have been compared to the spheres. Additionally, the interfacial thermal conductance to flat interfaces that match the facets exposed on the surfaces of the spheres are presented for comparison.

One possible explanation for an empirical relationship like Eq. (3.1) is that there is a significant contribution to interfacial thermal conductance that depends on the surface area to volume ratio, suggesting a large role for the surface atoms. In Chapter 2, the thermal conductance out of chemically-modified gold surfaces was examined via reverse nonequilibrium molecular dynamics (RNEMD). [58, 62, 66] In that chapter, surfactants attached to the gold surfaces contained a strong gold – sulfur interaction that acted as a bridge for vibrational energy to travel to the ligand. Although the presence and density of the ligand layer has a large effect on the interfacial conductance, no clear trend was established regarding the size and curvature of the underlying nanoparticles. Previous studies from Tascini *et al.*[63] and Ong *et al.*[67] predict a decrease in the interfacial thermal conductance as the particle radius increases, although Ong *et al.*[67] and Zanjani *et al.*[59] predict higher thermal conductivity with increasing core diameter in nanocrystal arrays. However, if surface modifications dominate conductance, the presence of a moderate density of ligands will obscure the effects of particle curvature.

### 3.1.1 Size- and temperature-dependent particle morphologies

The nanoparticles simulated for this work ranged in size from 309 atoms to 14,993 atoms. Ercolelli *et al.*[111] annealed at temperatures from 400K to 1400K and found the dominant structures for different sizes of gold particles ( $N = 100\text{-}900$  atoms). For  $N = 100\text{-}200$ , the structures were dominated by glassy clusters while for  $N = 200\text{-}900$ , the structures were predominantly cuboctahedral. Similarly, Myshlyavtsev and Stishenko found, when comparing gold nanostructures, a transition from a fully (111) icosahedral structure to a (100)-terminated cuboctahedral structures between 561 to 1,415 atoms, depending on the potential energy function.[112] Distinct vibrational densities of states have also been observed for the cuboctahedral clusters relative to icosahedra.[113]

In a study of the thermal stability of gold icosahedra, Wang *et al.*[114] found that softening of the vertex and edge atoms occurs at  $\approx 800\text{K}$ . During this process they saw enhanced surface atom diffusion due to the mobility of the vertex and edge atoms.

The size range ( $N = 300\text{-}15,000$ ) and temperatures (250K) for the calculations described here exhibit stable icosahedra with relatively low surface atom mobility, except for the smallest ( $r = 18\text{-}22 \text{\AA}$ ) particles, which may be metastable relative to cuboctahedra.

### 3.1.2 Theory

Under the diffuse mismatch model (DMM), the thermal conductance at an interface between  $a$  and  $b$  can be approximated,

$$G_{ab} = \frac{1}{4\pi} \sum_p \int_{\omega} \int_{\theta} \int_{\phi} \hbar\omega \frac{\partial f}{\partial T} v_a \rho_a \tau_{ab} \cos \theta \sin \theta d\theta d\phi d\omega \quad (3.2)$$

where  $f$  is the Bose-Einstein distribution function,  $v_a(\omega, p)$  is the group velocity (on side  $a$ ) for a phonon characterized by frequency  $\omega$ , moving in direction  $(\theta, \phi)$  with polarization  $p$ . The relevant material properties are the density of phonon states,  $\rho_a(\omega, p)$  and the transmission probability,  $\tau_{ab}(\omega, p)$ , at the interface.[13, 19, 20]

The diffuse mismatch model has a number of significant issues, particularly when the Debye model is a poor representation of the density of states, or where there is a fictitious boundary between identical materials (where the DMM predicts a non-zero resistance).[13] There is also an assumption of detailed balance built-in to the model,[8] which requires the two sides to be at equilibrium. This assumption is violated under non-equilibrium conditions, as in the RNEMD simulations used here. Although the DMM is not quantitative, it does suggest a role for frequency-dependent phonon transmission at the interface and that isolating the frequencies of the phonons moving towards the interface could aid in understanding interfacial conductance.

Using atomic velocities projected in a direction normal to the interface,

$$v_i^\perp(t) = \mathbf{v}_i(t) \cdot \hat{\mathbf{n}}, \quad (3.3)$$

it is straightforward to compute vibrational power spectra,

$$\rho^\perp(\omega) = \frac{1}{\tau} \int_{-\tau/2}^{\tau/2} \langle v^\perp(t) \cdot v^\perp(0) \rangle e^{-i\omega t} dt \quad (3.4)$$

which have been averaged over direction and polarization, where  $\tau$  is the total observation time for the autocorrelation function. This can be used to approximate the density of phonon states of the two materials near the interface, which can provide a clearer picture of vibrational communication between the two materials. By further restricting the density of states calculation to specific atoms at the metallic side of the interface, it might provide a mechanism for heat flow from the solid and into the surrounding liquid.

To compute interfacial thermal conductance values directly, reverse non-equilibrium molecular dynamics (RNEMD) simulations are utilized.[49, 51] RNEMD imposes an unphysical kinetic energy exchange between the center of the particle and a spherical shell of solvent that is well-separated from the interface. The system responds by creating a thermal gradient in the metal and solvent regions, and a temperature discontinuity at the interface between the particle and the solvent. The Kapitza resistance of the interface,

$$R_K = \frac{1}{G} = \frac{1}{q_r} \sum_i (T_{i+i} - T_i) 4\pi r_i^2, \quad (3.5)$$

is estimated by summing the individual thermal resistances of concentric spherical shells as the radius increases.[58] Here,  $T_i$  is the temperature of a shell with radius  $r_i$ , and  $q_r$  is the heat rate (the relevant measure of thermal transport in spherical geometries). The heat rate is the surface area of the particle times that of the imposed flux. The interfacial thermal conductance of the interface,  $G$  is the inverse of the net Kapitza resistance. For interfaces of appreciable width, the relevant shells for measuring interfacial resistance are the largest shell that is unambiguously in the particle and the smallest shell that is unambiguously in the solvent.

For planar or periodic geometries, the interfacial thermal conductance can be similarly computed by imposing a non-physical flux between two separated slabs in the simulation cell. In this case, the Kapitza resistance,

$$R_K = \frac{1}{G} = \frac{\Delta T}{J_z}, \quad (3.6)$$

depends on the imposed kinetic energy flux,  $J_z$ , in a direction normal to the interface ( $z$ ), and the steady-state temperature drop,  $\Delta T$ , across the interface.[51]

### 3.2 Computational Details

Solvated gold nanoparticles ranging in diameter from 20-80 Å were simulated using reverse non-equilibrium molecular dynamics (RNEMD) in a spherical shell of hexane. Similar planar systems, displaying (111), (110), and (100) facets with hexane solvent were also prepared. The following sections describe the system composition, the potentials used to calculate the interactions in the system, as well as the simulation protocol.

#### 3.2.1 System Composition

Both the nanoparticle and planar systems contain only gold atoms and hexane molecules. The composition of the planar systems can be found in Table 3.1 and the nanoparticle system details can be found in Tables 3.2, 3.3, and 3.4.

Planar systems were constructed with the exposed ( $hkl$ ) facets directed normal to the positive and negative  $z$ -axis. The simulation cell dimensions were set by the facet, and the simulation box was enlarged along the  $z$  dimension to a fixed size of 100 Å. The remaining space was filled with hexane molecules to a density of 0.6548 g cm<sup>-3</sup>.

#### 3.2.2 Force Fields

For this work, gold – gold interactions are calculated using the quantum Sutton-Chen (QSC) model.[26] The hexane solvent is described by the TraPPE united atom (UA) model.[2] The bonds in TraPPE-UA are rigid, but here the bonds are made flexible using harmonic force constants borrowed from OPLS-AA for intra-molecular sites closer than 3 bonds.[115] The interactions between Au atoms and atoms on the

TABLE 3.1

Composition of the solvated planar facet systems and the physical extent of the gold slabs ( $L_x$ ,  $L_y$ , and  $L_z$ ). The hexane molecules occupy the remainder of a 100 Å box (length measured along the  $z$ -axis).

Facet	Au atoms	$L_x$ (Å)	$L_y$ (Å)	$L_z$ (Å)	Hexane Molecules
(111)	972	25.915	29.888	18.952	284
(110)	1800	40.131	34.089	20.280	498
(100)	1008	24.322	24.382	26.422	200

TABLE 3.2

Composition of the solvated nanosphere simulations.

Particle Radius (Å)	Components	
	Au atoms	Hexane Molecules
9.20 ± 0.28	249	2894
14.30 ± 0.31	887	6304
19.07 ± 0.28	1985	8555
24.09 ± 0.32	3925	11576
29.03 ± 0.29	6699	15376
34.01 ± 0.32	10641	9235
38.88 ± 0.31	15707	8056

TABLE 3.3

Composition of the solvated icosahedral nanoparticle simulations.

<i>n</i> shells	radius (Å)	Components	
		Au atoms	Hexane Molecules
4	9.45 ± 0.15	309	2894
5	11.75 ± 0.17	561	4320
6	14.07 ± 0.19	923	6304
7	16.39 ± 0.21	1415	7414
8	18.71 ± 0.25	2057	8555
9	21.04 ± 0.27	2869	8555
10	23.36 ± 0.30	3871	11576
11	25.69 ± 0.32	5083	11576
12	28.02 ± 0.35	6525	11576
13	30.35 ± 0.38	8217	7741
14	32.67 ± 0.41	10178	9235
15	35.00 ± 0.43	12430	10911
16	37.33 ± 0.66	14993	11576

TABLE 3.4

Composition of the solvated cuboctahedral nanoparticle simulations.

radius(Å)	Components	
	Au atoms	Hexane Molecules
7.41 ± 0.35	147	11360
10.16 ± 0.53	309	3387
12.15 ± 0.50	561	5888
14.98 ± 0.69	923	7414
16.93 ± 0.65	1415	9440
19.80 ± 0.85	2057	9380
21.73 ± 0.82	2869	10317
24.13 ± 0.90	3871	14185
26.53 ± 0.99	5083	19585
31.34 ± 1.15	8217	12626
36.15 ± 1.32	12431	17457

hexane molecules were fit to a pairwise Lennard-Jones potentials based on a study by Hautman and Klein for Au(111) surfaces.[7] Details of the interaction potentials are identical to previous work and the previous chapter on heat transport for thiolate-protected gold nanospheres.[62]

### 3.2.3 Simulation Protocol

The gold nanospheres were prepared by cutting a FCC lattice with radii ranging 10 - 40 Å. Icosahedral particles were constructed in nested shell structures, built around an ideal icosahedral core. Cuboctahedral particles were built by cutting (111) and (100) facets from a FCC lattice. All particles were thermally equilibrated before being solvated with thermally equilibrated hexane using packmol.[97] Once solvated, the systems were equilibrated for a minimum of 1 ns using the Langevin Hull integrator with an external bath characterized by 50 atm of pressure and a temperature bath at 250K.[1] Random seeds were used in both the packing of the solvent and the equilibration process to ensure independent samples.

Planar interfaces displaying the Au(111), Au(110), and Au(100) facets were prepared as slabs  $\sim$  20 Å thick with the relevant facets rotated normal to the  $z$ -axis. Surface stress was removed by relaxing the systems for 1 ns at 250 K in a constant surface tension ( $N\gamma T$ ) ensemble with zero applied surface tension, followed by 1 ns in the microcanonical (NVE) ensemble. Hexane molecules were packed into the remaining box volume with a density of 0.6548 g/cm<sup>3</sup>. The solvated systems were then equilibrated using the canonical (NVT) ensemble at 250 K for 1 ns followed by further relaxation in the microcanonical ensemble for 1 ns.

Following equilibration, the relevant thermal flux was applied for 1 ns for the nanoparticle systems and 3 ns for the planar systems, allowing for a steady-state temperature gradients to develop. Mean temperatures of the system remained at 250K, preserving the solvent cluster around the nanoparticles and preventing the

formation of a vapor layer. Thermal coupling to the external temperature bath was removed to avoid interference with the imposed flux. The metal particles equilibrated rapidly, and were typically found with elevated temperatures ( $\sim$ 300K) relative to the bulk. Because the solvent volume is large relative to the particles, the solvent finds a steady state temperature just below 250K throughout most of the volume. Adjacent to the surface of the particles, solvent temperatures are typically close to 260K. The TraPPE-UA hexane model boils at  $\sim$  330K, so the simulation conditions are reasonable for maintaining liquid surroundings for the particles. All simulations were carried out with the open source molecular dynamics package, OpenMD.[95, 96]

Five separate configurations for each system size were simulated to provide statistical independence of the hexane packing. For the non-periodic systems, thermal conductance was calculated using the same methods found in Stocker *et al.*[62] and in the previous chapter. Planar systems follow Eq. 3.6, where the temperature difference across the interface is taken from the outermost gold layer and the first layer of solvent.

### 3.3 Results and Discussion

The interfacial thermal conductance ( $G$ ) for hexane-solvated spherical, icosahedral, and cuboctahedral Au nanoparticles was computed using RNEMD simulations, and was compared with the same quantity for a series of planar gold interfaces, including the Au(111), Au(100), and Au(110) interfaces. These surfaces are all exhibited as microfacets on the surfaces of the nanospheres, and the Au(111) facet is the primary facet displayed by the icosahedra, where the cuboctahedra display Au(111) and Au(100).

Computed interfacial thermal conductance values for the icosahedra, cuboctahedra, nanospheres, and flat facets are shown in Fig. 3.1. The nanospheres have a pronounced dependence on the particle radius,  $r$ , while the icosahedral conductance

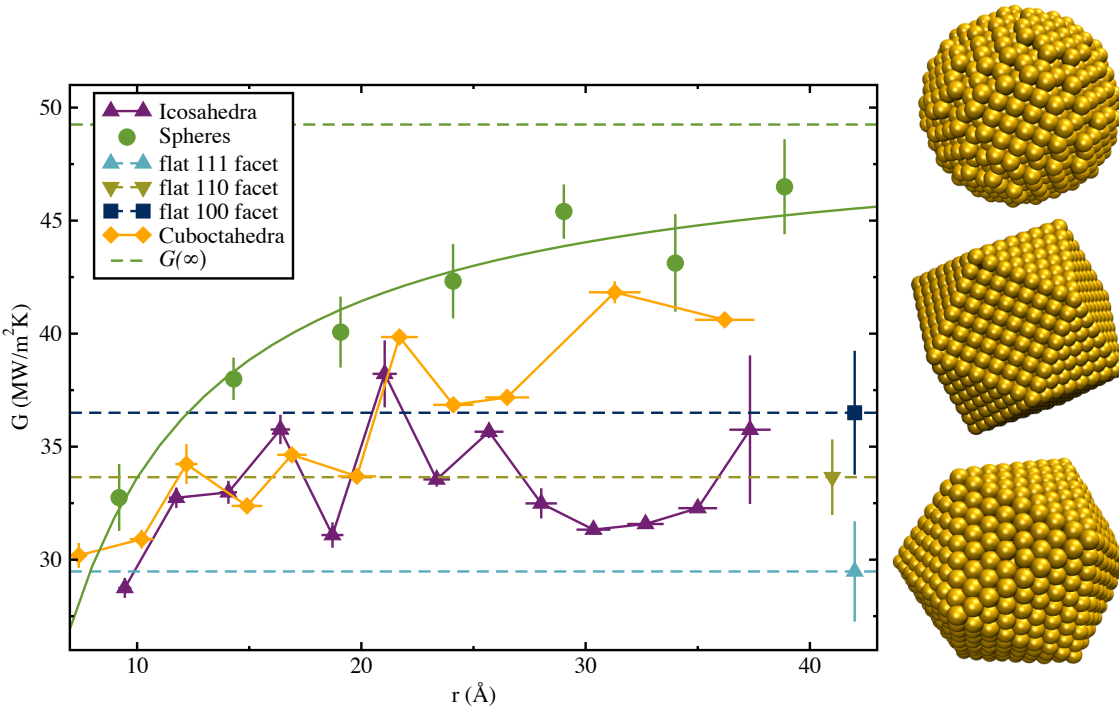


Figure 3.1. Interfacial thermal conductance,  $G$ , for bare gold nanospheres, cuboctahedra, and icosahedra in contact with hexane solvent.

Conductances for flat Au(111), Au(100), and Au(110) interfaces are indicated with dashed horizontal lines. A fit using the model of Tascini *et al.* is shown along with the predicted value of  $G(\infty)$ , the infinite particle limit.

stays relatively close to the value obtained for the Au(110) facet. Thermal transport out of the cuboctahedral particles show a mostly linear dependence on particle radius. The smooth line going through the conductance values for the spheres is a fit using the Tascini *et al.*[63] model (Eq. (3.1)) with  $G(\infty) = 49.25 \text{ MW m}^{-2} \text{ K}^{-1}$ , and  $\delta = -156.25 \text{ MW } \text{\AA}^{-2} \text{ K}^{-1}$ . Notably, the simulations presented here project a value for the interfacial conductance of the infinite spheres that is significantly *higher* than many of the flat facets. To explain this observation, the surface density of undercoordinated atoms and the vibrational densities of states of these undercoordinated atoms are discussed in the following sections.

The spherical particles display all three of the planar facets (as well as small

regions of higher index facets), and for most of the size range simulated, they also exhibit a significantly higher interfacial thermal conductance than the low-index facets.

For icosahedral particles, there is no clear dependence of  $G$  on the particle size, and the larger particles exhibit thermal conductance values slightly above the expected (111) conductance for particles with  $r \approx 35 \text{ \AA}$ . There is some instability in the values of  $G$  in the range of  $r = 18 - 22 \text{ \AA}$ , which is near the transition from stable icosahedra to cuboctahedra.[112]

### 3.3.1 Hexane Density

The hexane density as function of distance from the gold at the interface of the planar facets is provided in Fig. 3.2. The solvent in the (111) and (100) systems display similar behavior, while the solvent near the (110) interface comes closer to the surface atoms. In the (110) system, the first layer of hexane is spread out over a thicker slab in comparison to the other two systems and allows solvent to come closer to the interfacial atoms. This is likely due to the ridges present on this interface. Within 5  $\text{\AA}$  of the interfacial gold layer, the three systems have the same amount of hexane.

### 3.3.2 Surface Atom Undercoordination

For the three flat facets, the primary feature that differentiates the facets is the coordination number (CN) of the atoms that are exposed to the solvent. In bulk Au, the coordination number of the atoms is twelve; six neighbors in plane, three below the atom, and three above the atom. Any atom with a coordination number below twelve would exhibit more vibrational freedom and is considered an undercoordinated site. The Au(111) surface presents gold atoms with nine surrounding metallic atoms ( $\text{CN} = 9$ ) to the solvent, while the Au(100) facet surface exposes atoms with  $\text{CN} = 8$ . Au(110) displays a corrugated surface where the two outer layers of atoms have

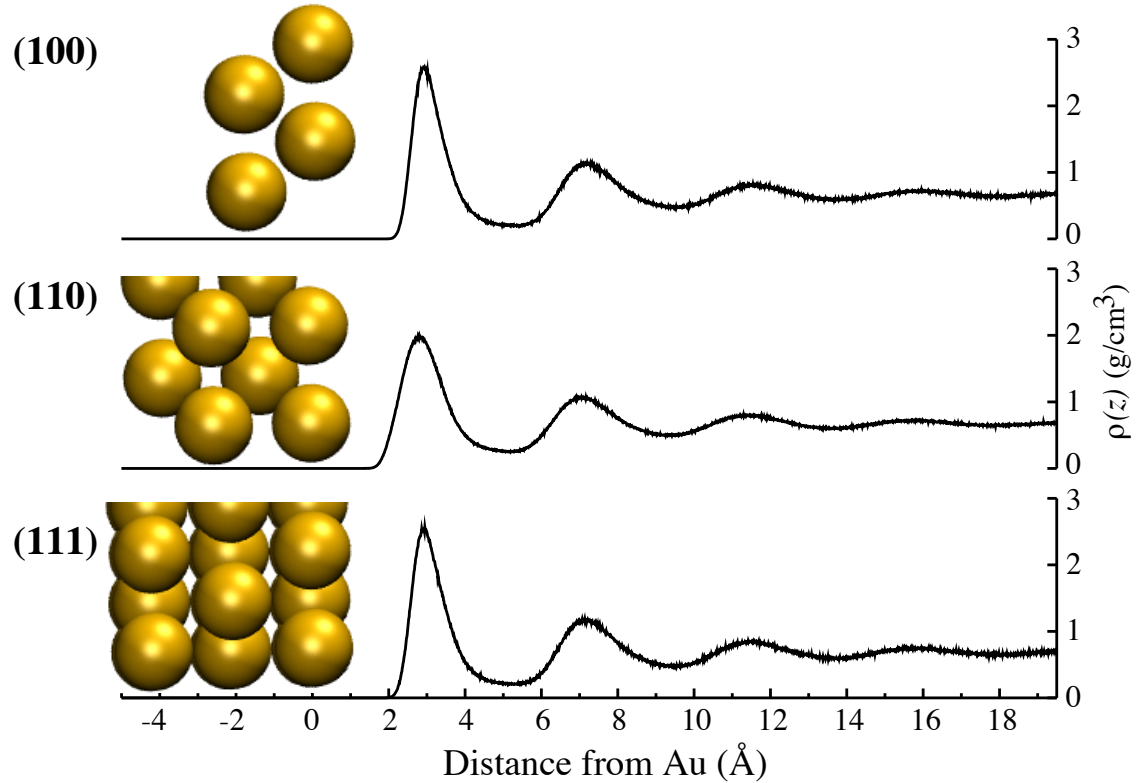


Figure 3.2. Hexane density as a function of distance from the interfacial gold for the (111), (110), and (100) facets. The solvent in the (111) and (100) systems display nearly identical density profiles. Because the lowest-coordinated gold atoms on the (110) facet have a relatively low surface density, the hexane molecules are able to get closer to these undercoordinated atoms.

TABLE 3.5

Surface densities ( $\text{\AA}^{-2}$ ) of undercoordinated atoms in ideal geometries.  $\ell$  ( $\text{\AA}$ ) is the lattice constant of the underlying FCC lattice. The spheres and cuboctahedra are calculated using a gold FCC lattice with  $\ell = 4.08 \text{ \AA}$ . For cuboctahedral particles, the radius ( $r$ ) is computed using Eq. (3.15).

surface	Coordination Number			
	6	7	8	9
(111)	0	0	0	$\frac{4\sqrt{3}}{3\ell^2}$
(100)	0	0	$\frac{2}{\ell^2}$	0
(110)	0	$\frac{\sqrt{2}}{\ell^2}$	0	0
Spheres (large $r$ limit)	0.021	0.025	0.021	0.032
Icosahedra ( $n$ shells)	$\frac{8\sqrt{3}}{5\ell^2 n^2}$	0	$\frac{4\sqrt{3}(n-1)}{\ell^2 n^2}$	$\frac{4(n-1)}{\sqrt{3}\ell^2 n}$
Cuboctahedra	0	$\frac{1}{r\ell} \left( \frac{3\sqrt{2}+2\sqrt{6}}{3+\sqrt{3}} \right)$	$\frac{6}{(3+\sqrt{3})\ell^2}$	$\frac{4}{(3+\sqrt{3})\ell^2}$

$\text{CN} = 7$  and  $\text{CN} = 11$ , respectively (displayed in Fig. 3.3). Both of the (110) surface atoms coordination environments approach the surface close enough to interact with the solvent atoms.

In Table 3.5, the surface density of undercoordinated atoms for a set of ideal geometries are provided. The population density for the spherical systems in the large radius limit are taken by averaging the surface densities for ideal gold nanospheres with radii of 95–100  $\text{\AA}$ . For other FCC-based nanoparticles, it is relatively simple to

convert these surface densities using the lattice constant of gold,  $\ell = 4.08 \text{ \AA}$ .

Planar facets have a fixed population density based on the number of exposed undercoordinated atoms and the physical dimensions of the exposed facet area in terms of the lattice constant. In an ideal icosahedral nanoparticle with  $n$  shells, the surface population density is computed using the number of vertex, edge, and face atoms,

$$n_{\text{vertex}} = 12, \quad (3.7)$$

$$n_{\text{edge}} = 30(n - 1), \quad (3.8)$$

$$n_{\text{face}} = 10n^2 - 30n + 20. \quad (3.9)$$

The number of shells,  $n$ , is also directly related to the particle edge length ( $a$ ), radius ( $r$ ), and surface area ( $A$ ) of the icosahedral particle,

$$a = \ell n \quad (3.10)$$

$$r = \frac{\ell n \sqrt{10 + 2\sqrt{5}}}{4} \quad (3.11)$$

$$A = \ell^2 n^2 5\sqrt{3} \quad (3.12)$$

where  $\ell$  is the lattice constant.

For ideal cuboctahedra, the edge length ( $a$ ) can be used to determine surface areas for the eight triangular (111) faces and six square (100) faces,

$$A_{(111)} = 2\sqrt{3}a^2 \quad (3.13)$$

$$A_{(100)} = 6a^2 \quad (3.14)$$

In addition, cuboctahedra have twenty-four edges (CN = 7, length =  $a$ ), and twelve vertices (CN = 5). An approximate radius of the cuboctahedral particles can be

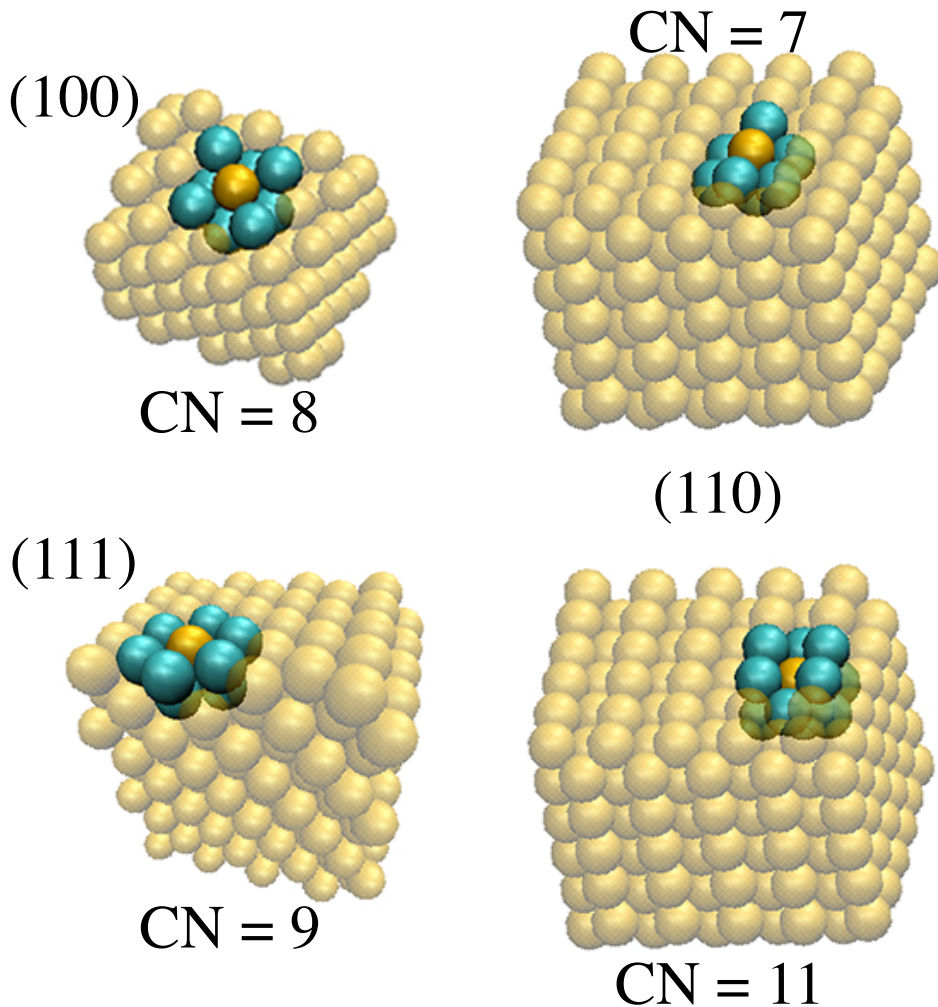


Figure 3.3. Locations of undercoordinated atoms on common gold facets. The dark gold atoms indicate atoms of a particular coordination number, cyan atoms denote the first nearest neighbors of these atoms, and the partially transparent lattice illustrates the location of the atoms in the larger gold structure. (111) surfaces (lower left) display atoms with CN=9, while (100) surfaces (upper left) display atoms with CN=8, and (110) surfaces present surface atoms with CN=7 and buried atoms with CN=11.

found by averaging the diameter between parallel square faces and parallel triangular faces,

$$r = \frac{a}{2} \left( \frac{\sqrt{2}}{2} + \frac{\sqrt{6}}{3} \right) \quad (3.15)$$

Table 3.5. Surface densities of the CN=9 and CN=8 sites are computed using the fraction of total surface area in each of the (111) and (100) facets, respectively. For small particles, the edge atoms (CN=7) can dominate, but for larger particles, the ratio of CN=8 and CN=9 atoms is constant.

Reducing the number of metallic interactions allows the surface atoms to vibrate at different frequencies than the interior atoms, populating a portion of the spectrum that overlaps with collective motions of the solvent molecules. This mechanism may explain the enhanced interfacial thermal conductance of the (100) facet relative to the (111) facet. However, it does not explain why the (110) facet displays an intermediate conductance even though the surface atoms have a lower coordination number than the (100) facet. To answer this question, it is important to consider the surface density of the undercoordinated atoms as well as the vibrational freedom allowed by the undercoordination. In Table 3.6 the density of the solvent-accessible undercoordinated surface atoms for the three facets is shown. Although the (110) facet displays 7- and 11-coordinated atoms to the solvent, the CN = 11 have vibrational dynamics that are essentially equivalent to the bulk gold (Fig. 3.4), and the surface density of these atoms is significantly lower than the surface density displayed by the (111) and (100) facets.

It is therefore likely that not only the undercoordination of surface atoms, but also the density of these undercoordinated atoms plays a role in thermal conductance. In the nanoparticles, surface atoms that are in physical contact with the solvent have a range of coordination numbers from 5 – 9, but only CN = 6 – 9 appear with high probability. The surface coordination densities have been calculated for all of the samples, and the undercoordination density is distinct for the spheres, icosahedra, and cuboctahedra (See Fig. 3.5).

The icosahedral particles display three coordination environments: the vertices

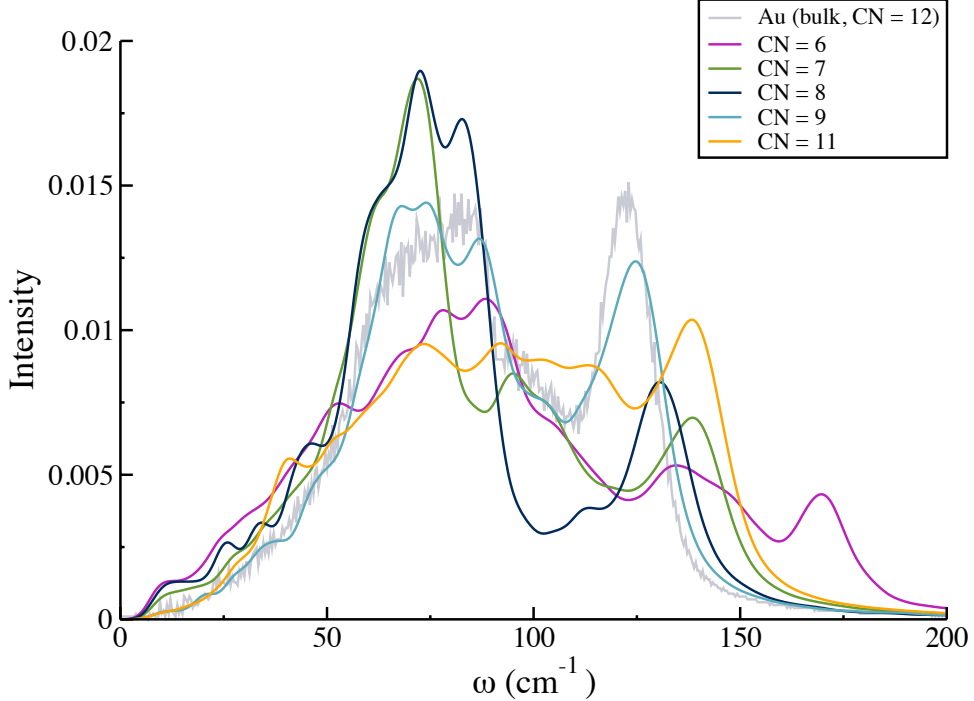


Figure 3.4. The normalized low frequency density of states (DOS) of the surface atoms with the coordination number of 6, 7, 8, 9 and 11, corresponding to the vertices of the icosahedra, Au(110), Au(100), Au(111) and subsurface Au(110), respectively. Note that CN=11 atoms near a surface are found adjacent to atoms with lower coordination (e.g. CN=7), so the high frequency peak at  $138\text{ cm}^{-1}$  is present for both CN=11 and CN=7. Low frequency contributions at  $\sim 70\text{ cm}^{-1}$  are enhanced for surface atoms with CN=7, 8, and 9.

have a CN = 6, while the triangular (111) faces of the particle have a CN = 9, and the edges connecting the faces have CN = 8. As the radius of the icosahedral particles increases, the surface is dominated by the triangular facets, so the surface density of the CN = 9 rises. For perfect icosahedra, the ideal surface densities are shown as dashed lines in Fig. 3.5.

For the simulated systems at 250K, surface vibrational motion leads to coordination numbers that are lower than one would expect for an ideal icosahedron. This is evident in the populations of the CN = 9, which is 20-50% lower than the ideal case.

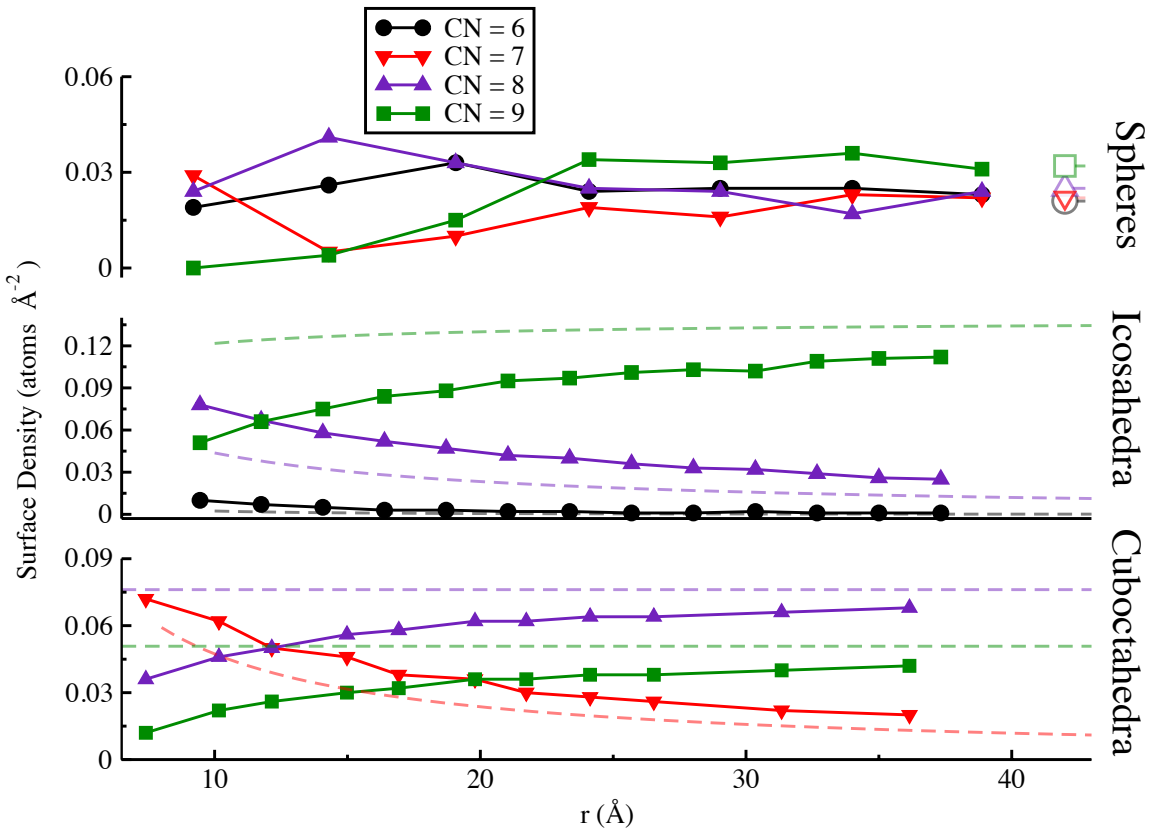


Figure 3.5. The coordination number of surface atoms as a function of particle size. Filled data points are sampled from simulations, while the dashed lines correspond to ideal icosahedral and cuboctahedral solids. In the spherical case, the large radius limits are shown with open symbols. The large radius limit for the spheres approaches a constant density for all undercoordinated sites, while for the icosahedra, the 9-coordinated (111) facet dominates. In larger cuboctahedra, the relative fraction of 8- and 9-coordinated surface atoms is largely independent of particle size.

TABLE 3.6

The density of undercoordinated gold atoms at the surface of a facet.

Facet	CN	Surface Density (atoms Å <sup>-2</sup> )
(111)	9	0.1394
(100)	8	0.1214
(110)	7	0.0877
	11	0.0877

In the spherical particles, the surface density of undercoordinated atoms stabilizes above  $r = 25$  Å. However, the densities of the undercoordinated atoms never approach any of the flat facet values (as is the case in the icosahedra). The large radius limit of the spheres are estimated by averaging the surface densities for ideal spheres of radii 95–100 Å. These are shown with open symbols in the upper panel of Fig. 3.5.

The cuboctahedral particles approach the ideal solid surface densities as the radius of the particle increases. Beyond a radius of 15 Å the cuboctahedra are no longer dominated by edge atoms and flat facets form the majority of the surface. After this transition the surface densities quickly stabilize to nearly-ideal cuboctahedral structures.

### 3.3.3 Phonon Spectra

By selecting specific groups of atoms while computing the vibrational power spectrum (Eq. 3.4) the role of undercoordination on surface vibrational motion can be explored. For thermal transport, the regions of interest are the nanoparticle atoms in direct physical contact with the solvent, and those solvent molecules that form the

first solvation shell, i.e.  $< 5\text{\AA}$  from the gold surface.

Under the QSC potential, the bulk gold vibrational power spectrum displays two broad peaks, one at  $\sim 60\text{--}80 \text{ cm}^{-1}$ , and another sharper peak at  $\sim 125 \text{ cm}^{-1}$ . The vibrational densities of states for the four outer layers of the nanoparticles are shown in Fig. 3.7. The surface layers for all particles are dominated by the low frequency portion of the spectrum ( $< 70 \text{ cm}^{-1}$ ) and display small morphology-dependent features at higher frequencies ( $140 \text{ cm}^{-1}$ ). The low-frequency peak appears at significantly lower frequencies than in the bulk, and the higher frequency contribution is significantly broadened. Spheres and cuboctahedra recover bulk-like densities of states relatively close to the surface – only the surface and second shell are significantly altered from the bulk gold density of states. In the spheres, the higher frequency contribution ( $\sim 150 \text{ cm}^{-1}$ ) resembles the vibrational density of states for undercoordinated atoms with CN=8 or 7 (see Fig. 3.4).

### 3.3.4 A Brief Aside on Local Orientational Ordering

The icosahedra still have perturbed spectra even four layers into the particles. Icosahedral particles grow around a core with  $I_h$  symmetry, and the local environment around the atoms deviates significantly from perfect FCC ordering. The local bond orientational order can be described using the method of Steinhardt *et al.*[98] The local bonding environment,  $\bar{q}_{\ell m}$ , for each atom in the system is determined by averaging over the spherical harmonics between that atom and each of its neighbors,

$$\bar{q}_{\ell m} = \sum_i Y_{\ell}^m(\theta_i, \phi_i) \quad (3.16)$$

where  $\theta_i$  and  $\phi_i$  are the relative angular coordinates of neighbor  $i$  in the laboratory frame. A global average orientational bond order parameter,  $\bar{Q}_{\ell m}$ , is the average over each  $\bar{q}_{\ell m}$  for all atoms in the system. To remove the dependence on the laboratory

coordinate frame, the third order rotationally invariant combination of  $\bar{Q}_{\ell m}$ ,  $\hat{w}_\ell$ , is utilized here.[98, 99]

For  $\ell = 4$ , the ideal face-centered cubic (FCC) local structures exhibit  $\hat{w}_4$  values near -0.159. Because  $\hat{w}_4$  exhibits an extreme value for fcc structures, it is ideal for measuring local FCC ordering. The spatial distribution of  $\hat{w}_4$  local bond orientational order parameters,  $p(\hat{w}_4, r)$ , can provide information about the location of individual atoms that are central to local FCC ordering.

The fraction of FCC-ordered gold atoms at a given radius in the nanoparticle,

$$f_{\text{fcc}}(r) = \int_{-\infty}^{w_c} p(\hat{w}_4, r) d\hat{w}_4 \quad (3.17)$$

is described by the distribution of the local bond orientational order parameters,  $p(\hat{w}_4, r)$ , and  $w_c$ , a cutoff for the peak  $\hat{w}_4$  value displayed by fcc structures. As seen in previous chapter,[62]  $w_c$  value of -0.12 was chosen to isolate the fcc peak in  $\hat{w}_4$ .

As shown in Fig. 3.6, the FCC ordering persists in the spheres even quite close to the surface, while the icosahedra have significant populations that deviate from FCC local ordering. The cuboctahedra do not have uniform gold population between 30 and 40 Å, so the fraction of FCC ordering decays starting at 30 Å. Although it cannot be concluded that this is the cause of the differences in the VDOS for the icosahedral particles, it is likely that local ordering in the metal can alter the bulk densities of states.

Comparison of the vibrational density of states of all the gold atoms displays some important differences between the icosahedral structures and the FCC-based spheres and cuboctahedra (Fig. 3.8). Icosahedral particles have non-FCC ordering deep into the particle, and this manifests as a shift in phonon population from the broad low-frequency region to the higher frequency peak, even for the largest of the particles that were studied. For comparison, the largest spheres and icosahedra have

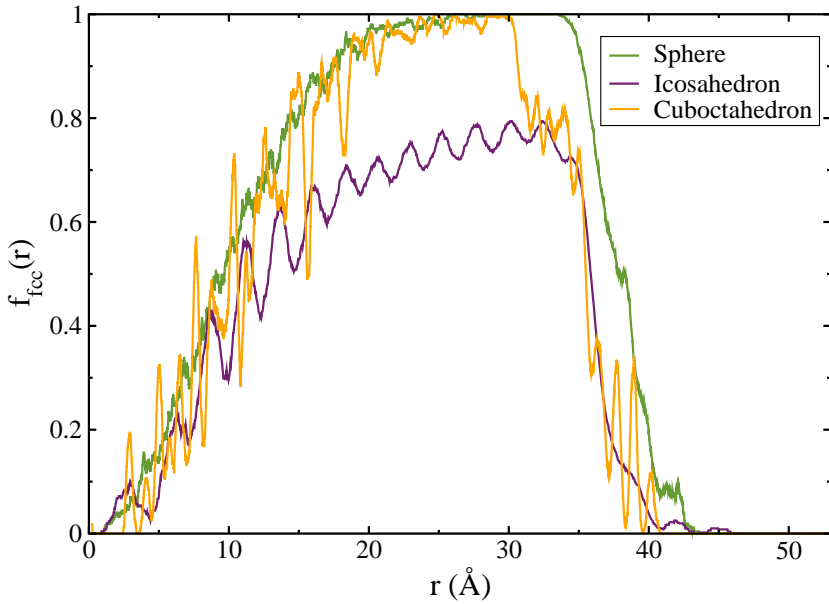


Figure 3.6. The fraction of FCC-like local environments as a function of radius from the center of 40 Å nanoparticles. The spheres and cuboctahedra are originally cut from a FCC lattice, so the local ordering persists even close to the surface. Icosahedra are constructed as shells surrounding a perfectly icosahedral central core of 13 atoms. Non-FCC ordering persists throughout these simulations.

only slight differences in their “bulk” phonon density of states.

At the surfaces of the particles, the differences are nearly all in the higher frequency portion of the spectrum ( $> 100\text{cm}^{-1}$ ), indicating that the surface undercoordination primarily alters high-frequency transmission into the solvent. This suggests roles for bulk crystalline ordering as well as surface undercoordination in any model for the interfacial thermal conductance.

Except in the case of the icosahedra, vibrational power spectra that include all gold atoms in the nanoparticles do not show significant dependence on particle radius (see Fig. 3.9. This suggests that mismatch models (like AMM or DMM) that use

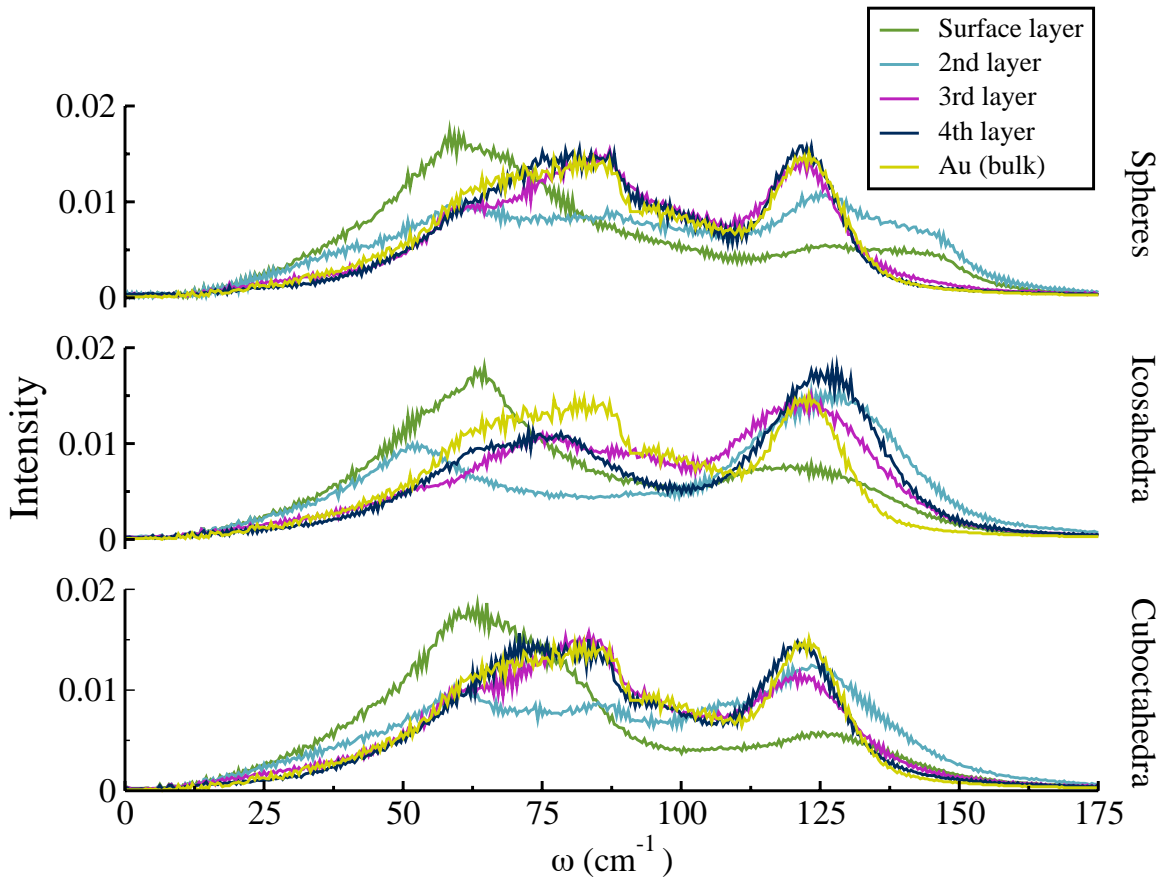


Figure 3.7. The projected vibrational density of states (Eq. 3.4) for individual layers in the largest gold nanoparticles (top: spheres, middle: icosahedra, bottom: cuboctahedra). In all systems, the surface layer (green) is significantly enhanced at low frequencies and is shifted down by  $\sim 20 \text{ cm}^{-1}$ . The Au (bulk) curve shown for comparison is from a perfect FCC lattice in periodic boundary conditions.

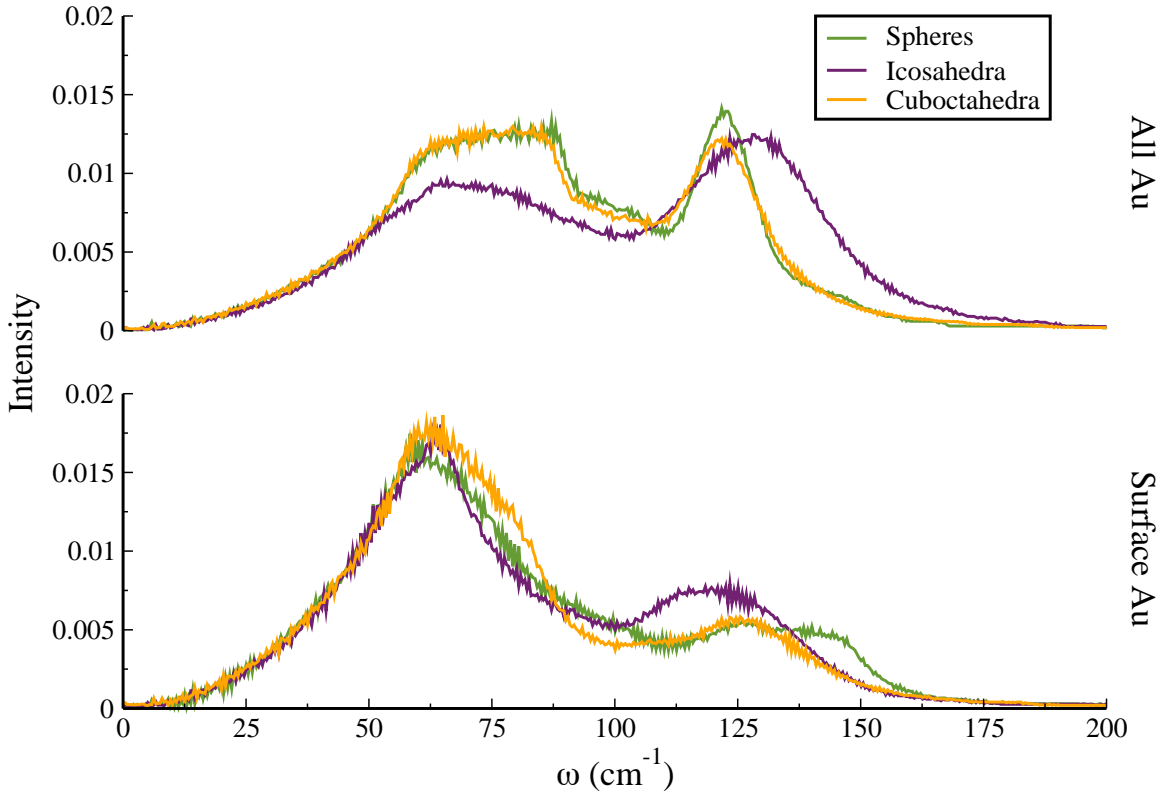


Figure 3.8. The projected vibrational density of states for all gold atoms (top panel) shows that the phonons in FCC-like nanoparticles (spheres, cuboctahedra) have similar frequency representation, while the non-FCC structures (icosahedra) have significantly altered “bulk” spectra. For surface atoms (bottom panel), the differences in surface undercoordination appear at higher frequencies. These spectra were computed for the largest particles in each of the different morphologies.

only bulk properties will not be able to capture the surface behavior that is relevant to heat transfer at the nanoscale.

Solvent vibrational densities of states are remarkably similar for the icosahedral and spherical particles, even for solvent that is within 5 Å of the interface (Fig. 3.9). While the solvent VDOS in the icosahedral and spherical systems shows only small changes as a function of particle size, the solvent in the cuboctahedral systems appears to shift to lower frequencies with increasing particle radius. The gold VDOS in all systems displays a shift from the low frequency peak,  $70\text{ cm}^{-1}$ , to a peak at  $125\text{ cm}^{-1}$  as the particle radii increases and there is a significant difference between the two FCC structures and the icosahedra spectra. The FCC structures increase in intensity at  $125\text{ cm}^{-1}$  with increasing particle radius, while the icosahedra VDOS shows a shift in population from low frequencies to the higher frequency peak. Note that the gold shown in Fig. 3.9 includes all layers of the particles.

Due to the similarity in solvent VDOS, a model for interfacial thermal transport in these systems would need to include the lattice structure of the particle and the quantity and solvent accessibility of specific kinds of undercoordinated metal atoms.

### 3.3.5 A Simple Model for Bare Nanoparticle Conductance

The vibrational densities of states suggest the bare metallic nanoparticles exhibit different bulk phonon frequencies that depend on crystalline packing, and different surface spectra that depend on surface undercoordination. Both of the bulk and surface frequencies can effect thermal transport, so a simple model in terms of a linear combination of surface densities of undercoordinated atoms can be explored,

$$G \approx a \text{ CN}_6 + b \text{ CN}_7 + c (1 + c' \delta_{\text{ico}}) \text{ CN}_8 + d (1 + d' \delta_{\text{ico}}) \text{ CN}_9 \quad (3.18)$$

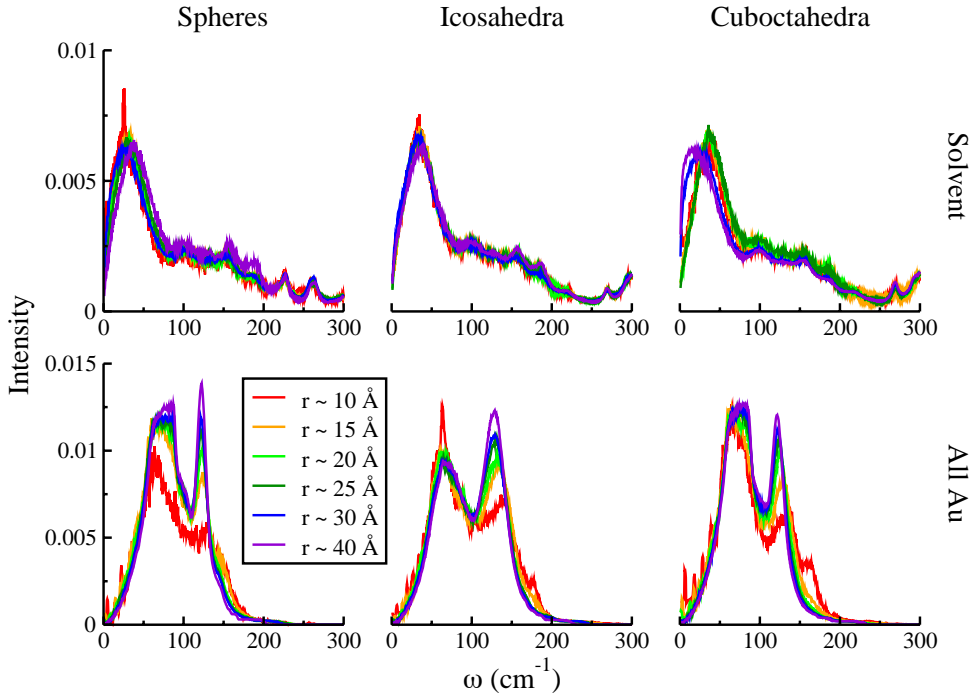


Figure 3.9. The normalized low frequency density of states (DOS) of the interfacial solvent and the gold particle for the icosahedral and spherical systems.

where,  $a-d$  are coordination transport coefficients with the units of  $10^{-20}$  MW/K and  $\text{CN}_n$  have surface density units ( $1/\text{\AA}^2$ ) for surface atoms with coordination number  $n$ . The delta function,  $\delta_{\text{ico}}$  is set to unity for icosahedral structures, and zero for FCC-like nanoparticles. The coefficients  $c'$  and  $d'$  are weighting factors that recognize the differences in the bulk density of states in the icosahedral particles. Fitting the six parameters was done using a simple ordinary least squares model with data from all simulated particles.

With Eq. (3.18) it should be possible to predict the interfacial thermal conductance for bare gold nanoparticles in hexane based only on a structural analysis of the surface for coordination densities and the interior of the particle for crystalline structure. The predicted (and simulated) values of the thermal conductance are given

TABLE 3.7

Parameters of the Model in Eq. (3.18).

$a$	$b$	$c$	$c'$	$d$	$d'$
858.9405	183.9062	291.7960	-0.5943	369.6250	-0.2498

in Fig. 3.10. With a coefficient of determination ( $R^2$ ) value of 0.656, this fit does not predict  $G$  with a high degree of certainty, but it does suggest the large role that undercoordinated surface atoms play in conductance. Coefficients used in Eq. (3.18) are given in Table 3.7.

The coefficients provide some information about the thermal transport capabilities of each type of undercoordinated surface atom. These fits suggest that severely undercoordinated atoms (CN=6) transfer the largest amount of heat per atom, although their population in all systems is low.

It is also important to note that this fit considers the two different types of particles when finding the best fits for the most populous surface atoms (CN=8, CN=9). If the system is FCC-like the weight of the CN = 8 and CN = 9 are 2.464 and 1.333 times larger than their contributions from icosahedral cores.

Since the coefficients are related to the amount of energy transferred per atom type, these atoms on the FCC-like structures transfer a larger amount than in the icosahedral structure. This is likely due to differences in the underlying “bulk” densities of states.

### 3.4 Conclusions

The primary observation of this work is that particle morphology has a significant effect on interfacial thermal conductance from bare particles to the surrounding

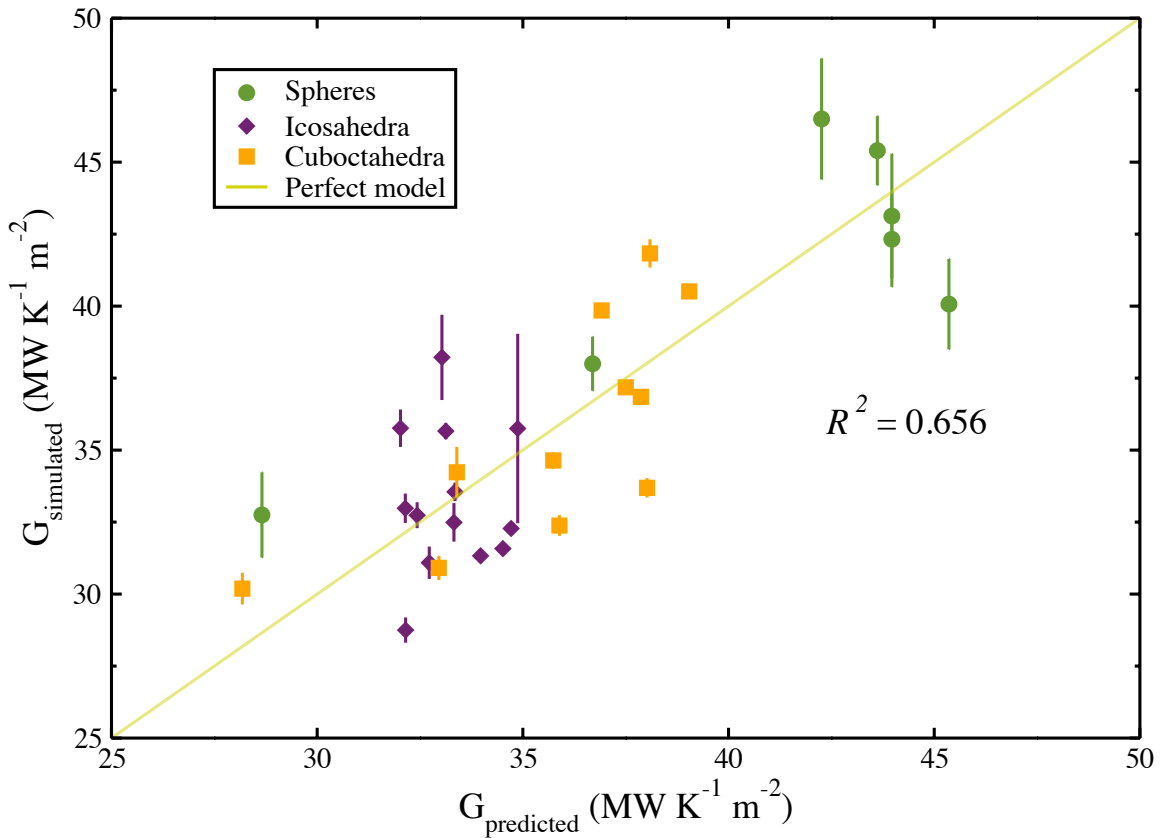


Figure 3.10. Structurally-predicted thermal conductance values from Eq. (3.18) compared with the simulated thermal conductance values. Error bars indicate the standard error computed using five replica simulations.

solvent. In particular, spherical and cuboctahedra particles have a size-dependent interfacial thermal conductance, while icosahedral particles conduct heat to the surrounding solvent only slightly better than the flat (111) facets.

This work explored one explanation for this difference in terms of the density of undercoordinated sites on the surfaces of these three particle morphologies. Nanospheres, because they are carved out of an underlying FCC lattice, expose significantly undercoordinated atoms ( $CN = 6 - 8$ ) to the solvent. For very small spheres, microfacets of (111), (100), and (110) dominate the surface, but for larger particles, the density of undercoordinated atoms becomes a significant fraction of the exposed atoms. In large icosahedral particles, the particles are dominated by (111) faces, and the  $CN = 9$  atoms dominate the surface. Similarly, in large cuboctahedral particles, the (111) and (100) facets are both present, and the  $CN = 9$  and  $CN = 8$  atoms share the particle surface in a 2:3 ratio. Surface atom undercoordination leads directly to changes in the surface vibrational density of states, particularly at frequencies around  $\sim 150\text{ cm}^{-1}$ . The linear model suggests that differences in surface atom undercoordination (particularly for atoms that are undercoordinated relative to a flat facet) may be largely responsible for thermal conductivity trends in this work.

This is not a complete explanation for the conductance values, however, as the large icosahedral particles exhibit  $G$  values above the planar (111) facet, and large cuboctahedra have  $G$  values above *both* the (111) and (100) facets. Edge and vertex atoms in these clusters may play an outsized role, and collective low-frequency modes of the particles may also be important, as the underlying “bulk” density of states also depends on particle morphology.

## CHAPTER 4

### A PREDICTION OF THE THERMAL CONDUCTIVITY OF $\text{Au}_{144}\text{PET}_{60}$ NANOARRAYS

#### 4.1 Introduction

Thiolated gold nanocluster have been studied in great detail both experimentally and theoretically.[116–119] The electronic,[120, 121] optical,[122] and catalytic properties;[123, 124] with respect to size range of the cluster and ligand identity pose promising features to make them building blocks for nanotechnology applications.[125–128] Additionally, nanocrystal arrays, close-packed structures of nanoparticles from a colloidal solution, have been proposed as alternatives for expensive single-crystal semiconductors materials in transistors,[129] memory devices,[130] solar cells,[131–133] and thermoelectrics.[65, 134–136]

One of the first theoretical studies of nanocrystal arrays was performed by Luedtke and Landman which examined small clusters with alkanethiol ligands on a graphite surface and in superlattices.[137] A more recent experimental study by Liu *et al.* presented the effect of surface chemistry on the thermal conductivity of a nanocrystal array.[60] The study by Liu *et al.* varied nanocrystal core size, the binding group of the ligand and the ligand length. The primary finding was that with a decrease to the ligand length or an increase to the core size the material thermal conductivity increased. The volume fraction of the insulating material, the ligand, is reduced in both of those cases.

Similar results have been seen in theoretical studies of nanocrystal arrays by Ong *et al.*[67] and Zanjani *et al.*[59] with respect to core diameter. In particular Ong *et*

*al.* found that in nanocrystal arrays vibrational states are able to elastically couple across the interfaces, with a thermal conductivity that is dependent on the density of the ligand layer.[67] The coupling was further studied through varying the core atomic mass and finding the relationship with the interfacial thermal conductivity.

The study by Zanjani *et al.* on gold nanocrystals with hexylthiol capping ligands varied core size and ligand density.[59] The phonon dispersion of the superlattice structures were obtained and the thermal conductivity of the nanocrystal arrays displayed the same trends as Liu *et al.* observed, an increase in thermal conductivity of the array with an decreased volume percentage of the ligand layer.[60]

All the nanoparticles previously studied contain  $N > 500$  atoms. Recent work by Pohjolainen *et al.* provides structures and force field parameters based upon crystal structures for thiolated gold nanoclusters found in a matching crystallography study of the clusters in arrays.[138] The provided structures contain individual particles as well as nanoarrays, with the largest of the parameterized structures contains 144 Au atoms. All of the characterized nanoclusters have a staple motif ligand that was shown to be thermally stable in this model. Many of the parameters were taken from work from Banerjee *et al.* that looked at  $\text{Au}_{25}$  and  $\text{Au}_{38}$  nanoclusters.

The staple motif in these nanoclusters present an interesting idea for thermal transport. The staple motif has three gold atoms (for the largest particle), two of the gold atoms in the staple are in direct contact with the core of the particle, while the remaining atom is within the ligand layer, bonded to sulfur atoms. Based upon previous work on the thermal properties due to under-coordination of gold atoms the surface,[73] the gold atoms within the staple motif could present interesting properties. For this reason we have looked at single particles and arrays of  $\text{Au}_{144}\text{PET}_{60}$  cluster in two solvents and fit to the Hasselman and Johnson equation for thermal conductivity of composite materials.[139]

#### 4.1.1 Theory

Hasselman and Johnson is first proposed a predictive formula for the effective thermal conductivity of a composite material using known material properties.[139] The following equation is the original formulation of the Hasselman and Johnson equation:

$$\lambda_e = \lambda_s \left( \frac{\lambda_p(1+2\alpha) + 2\lambda_s + 2v_p[\lambda_p(1-\alpha) - \lambda_s]}{\lambda_p(1+2\alpha) + 2\lambda_s - v_p[\lambda_p(1-\alpha) - \lambda_s]} \right) \quad (4.1)$$

where  $\lambda_e$  is the effective thermal conductivity of the composite material,  $\lambda_p$  and  $\lambda_s$  are the particle and solvent thermal conductivities,  $v_p$  is the volume fraction of the nanoparticles, and  $\alpha$  is the interfacial term. The interfacial term is a dimensionless term that is composed of the thermal boundary resistance over the radius of the particle. The thermal boundary resistance in this work is taken to be

$$\alpha = \frac{R_{TBR}}{r_p} = \frac{\lambda_s}{Gr_p} \quad (4.2)$$

where  $G$  is the interfacial thermal conductivity from the particle to the solvent, and  $r_p$  is the radius of the particle. Modifications to the Hasselman and Johnson equation have been made by Minnich *et al.* to include an interface density for the spherical particles and a more formal volume fraction of the nanoparticles.[140]

Each portion of Eq. 4.1 can be calculated in order to predict a composite material thermal conductivity. The volume fraction of the particles can be found through geometric means using the information about the particles in the array. The thermal conductivity of the solvent,  $\lambda_s$ , can be found through simulations of bulk solvent. Similarly,  $\lambda_p$  can be calculated from bulk simulations of the core material of the particle. The most difficult piece is the  $\alpha$  term, where the interfacial thermal conductivity of the particles is the primary value of importance. The interfacial thermal conductance of the nanoclusters investigated in this work were found using the same method as Stocker *et al.* for nanospheres.[62]

Typically modelling work of heat conduction of nanoarrays consider only one method for thermal transport: conduction. This work is a purely classical approximation of nanoarrays and does not consider electron effects (such as polarization of the gold surface and radiation). While convection could be seen through classical simulations the time scales involved would take extensive simulations and result in an expensive study. Additionally, the solvent between the particles in the arrays could display altered diffusion coefficients due to confinement and change in temperature. Any coupling in these systems between the gold particles could only be seen through a classical means and the electronic contributions are not considered.

## 4.2 Computational Details

Nanoarrays of  $\text{Au}_{144}\text{PET}_{60}$  solvated with either toluene or dichloromethane were simulated using reverse nonequilibrium molecular dynamics (RNEMD). Individual components of the system: single particles in each solvent, pure solvent, and liquid gold; simulations were also prepared and simulated using RNEMD. The following sections describe the potentials used for the interactions in the system as well as how the systems were created and prepared.

### 4.2.1 Force Fields

In the particle systems and the liquid gold simulations, the gold–gold interactions are calculated using the quantum Sutton-Chen (QSC) model.[26] Within the  $\text{Au}_{144}\text{PET}_{60}$  particle there are three distinct gold atom types defined:  $\text{Au}_{\text{body}}$ ,  $\text{Au}_{\text{surface}}$ , and  $\text{Au}_{\text{ligand}}$ . The gold interior to the particle, the icosahedral core, is defined as an  $\text{Au}_{\text{body}}$  atom. The other two gold atom types are within the ligand staple motif and are bonded to sulfur atoms.  $\text{Au}_{\text{surface}}$  is the gold in the staple motif that is in direct contact with the surface of the particle.  $\text{Au}_{\text{surface}}$  is treated with QSC for the interactions with  $\text{Au}_{\text{body}}$  but with a Lennard-Jones potential for  $\text{Au}_{\text{ligand}}$ , which

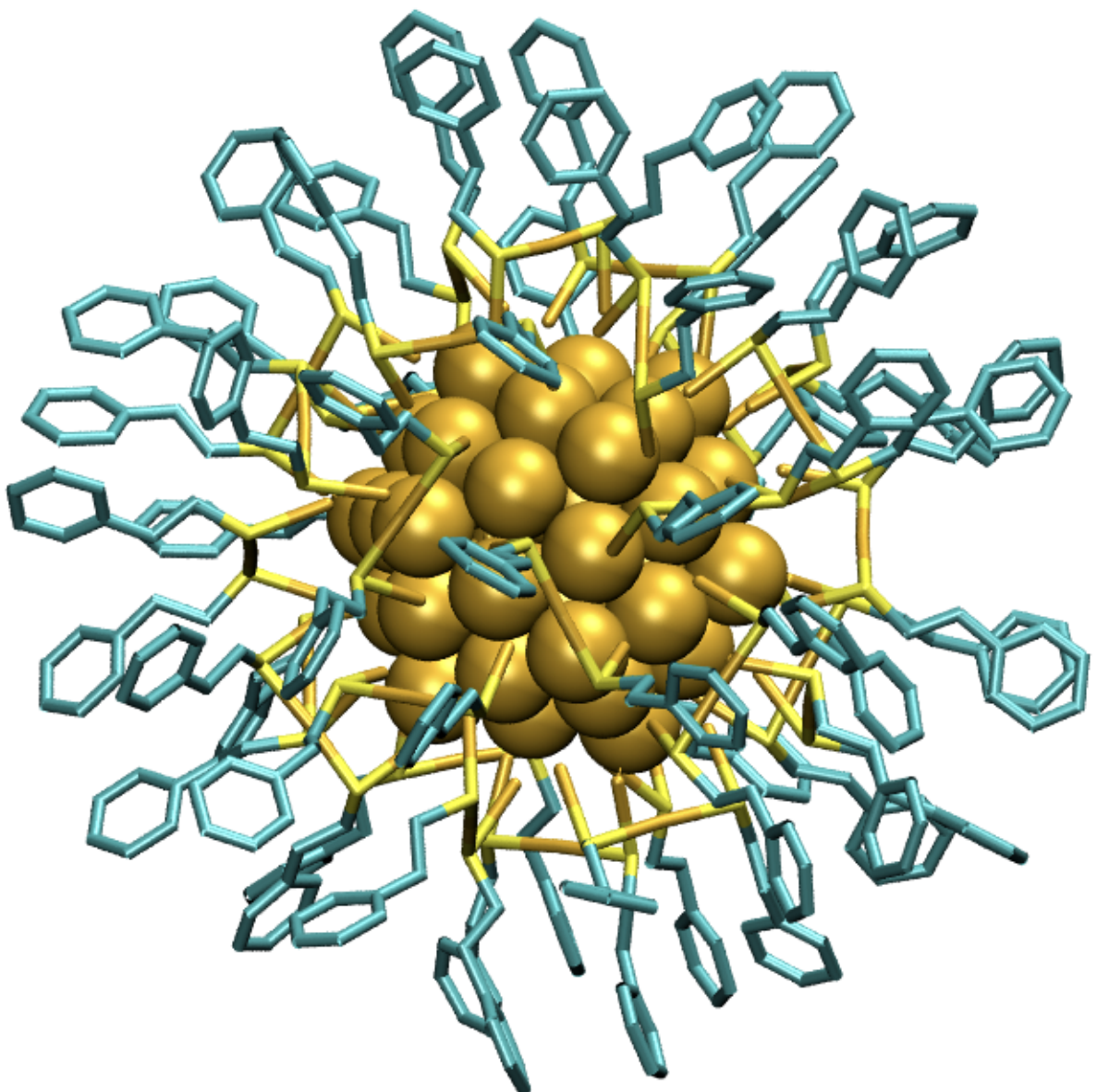


Figure 4.1. A single  $\text{Au}_{144}\text{PET}_{60}$  cluster with the icosahedral core atoms rendered as spheres. All atoms in the ligand staple motif are displayed as stick like structures for clarity of the particle structure.

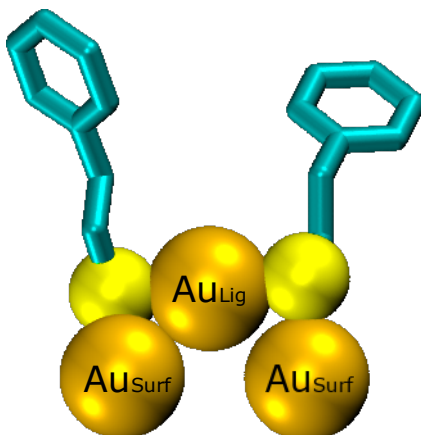


Figure 4.2. The Au and S atoms in the staple motif are depicted with spheres, while the PET R groups are shown as stick like structures for clarity of the staple structure. The  $\text{Au}_{\text{surf}}$  atoms sit directly on the icosahedral core of the nanocluster, while the  $\text{Au}_{\text{lig}}$  atom is slightly out from the gold surface and bonded to the sulfur atoms in two PET ligands.

is further from the surface of the particle and bonded between two sulfur atoms.  $\text{Au}_{\text{ligand}}$  is treated as a Lennard-Jones atom type with parameters from Pohjolainen *et. al.*[138] All parameters for the staple motif use parameters from Pohjolainen *et. al.*[138] and Banerjee *et al.*[141] in addition to parameters from TraPPE-UA[2, 3] which can be found in Table 4.1.

TABLE 4.1

Composition of a single nanoparticle and non-bonded interactions  
parameters for the interaction with gold.

Sites	atoms	mass	$\sigma_{ii}$	$\epsilon_{ii}$	$\sigma_{\text{Au}-i}$	$\epsilon_{\text{Au}-i}$	source
		(amu)	(Å)	(kcal/mol)	(Å)	(kcal/mol)	
Au <sub>body</sub>	54	196.97			parameters from QSC		
Au <sub>surface</sub>	60	196.97			parameters from QSC		
Au <sub>ligand</sub>	30	196.97	2.629	5.2899	2.629	5.2899	Refs. [138] and [141]
S	60	32.0655	4.45	0.2504	2.40	8.465	Refs. [5] ( $\sigma$ ) and [6] ( $\epsilon$ )
CH <sub>2</sub>	120	14.03	3.95	0.09141	3.54	0.1749	Refs. [2], [6] and [5]
Char	360	13.02	3.695	0.1004	3.4625	0.1680	Refs. [3] and [6]

The solvent models, dichloromethane and toluene, and the organic ligands use parameters from united atom models. Dichloromethane is modeled with Lennard-Jones atoms type and charges are taken from Meyer *et. al.*[142] and the intramolecular parameters use harmonic force constants from OPLS-AA.[115] Toluene is modeled as a rigid body in a trans conformation using parameters from TraPPE-UA.[3] Within the ligand staple motif, the carbon atoms were treated with TraPPE-UA,[2–4] while the sulfur used parameters from TraPPE-UA[4] and bonds, bends, and torsions for the staple from Pohjolainen.[138]

Non-bonded interactions between the staple motif and icosahedral core of the particles are modeled through parameters derived from adsorption studies of thiolates on Au surfaces. The S—Au non-bonded parameters are adopted from work from Luedtke and Landman,[5] where thiolates are absorbed on Au(111) surfaces .

Other interactions between Au and non-metal atoms in the staple ligand are adapted from an adsorption study by Vlugt *et. al.*,[6] of alkyl thiols on gold surfaces. The parameters are from a pair-wise Lennard-Jones potential for the interaction between Au and  $\text{CH}_x$  and S based upon the Hautman and Klein potential for Au(111) surfaces.[7] The non-bonded interactions between gold atoms and toluene solvent use parameters from the same work. Au and dichloromethane interactions use the aforementioned work from Vlugt for the central carbon and the Au-Cl interactions was found through Johnson mixing rules.[143]

#### 4.2.2 Simulation Protocol

The gold particle simulations are started from crystal structures provided in work from Pohjolainen *et. al.*[138] The crystal structures were thermalized to 250K then solvated using packmol[97] with either dichloromethane or toluene molecules that were also equilibrated to 250K. The amount of solvent was chosen such that packing

TABLE 4.2

Harmonic bond parameters for different components in the simulated systems. The first part of the table are the atoms in the staple motif within the nanoparticle. The latter sections are the solvents: toluene and dichloromethane, respectively.

$i$	$j$	$r_0$ (Å)	$k_{\text{bond}}$ ( kcal/mole/Å <sup>2</sup> )	source
Au <sub>surf</sub>	S	2.41	150	Ref. [138]
Au <sub>lig</sub>	S	2.33	150	Ref. [138]
S	CH <sub>2</sub>	1.820	444	Refs. [4] and [92]
CH <sub>2</sub>	CH <sub>2</sub>	1.540	536	Refs. [2] and [92]
Char	CH <sub>2</sub>	1.540	536	Refs. [3] and [92]
Char	Char	1.40	938	Refs. [3] and [92]
Char	Char	1.40	938	Refs. [3] and [92]
Char	CH <sub>3</sub>	1.540	536	Refs. [3] and [92]
Cl	CH <sub>2</sub>	1.40	938	Ref. [142]

TABLE 4.3

Bend angle parameters for a harmonic potential. The central atom in the bend is atom  $j$ . The table is structured with the particle staple motif in the first section, followed by the solvents: toluene and dichloromethane.

$i$	$j$	$k$	$\theta_0$ (°)	$k_{\text{bend}}$ (kcal/mol/rad $^2$ )	source
Au <sub>surf</sub>	S	Au <sub>lig</sub>	91.3	460.24	Ref. [141]
S	Au <sub>lig</sub>	S	172.24	240.24	Ref. [141]
Au <sub>surf</sub>	S	CH <sub>2</sub>	111.6	146.37	Ref. [141]
Au <sub>lig</sub>	S	CH <sub>2</sub>	106.8	146.37	Ref. [141]
S	CH <sub>2</sub>	CH <sub>2</sub>	114.0	124.20	Ref. [4]
CH <sub>2</sub>	CH <sub>2</sub>	CChar	114.0	124.20	Ref. [4]
CH <sub>2</sub>	CChar	CChar	120.0	140.0	Refs. [3] and [92]
CChar	CChar	CChar	120.0	126.0	Refs. [3] and [92]
CChar	CChar	CH <sub>3</sub>	120.0	140.0	Refs. [3] and [92]
CChar	CChar	CChar	120.0	126.0	Refs. [3] and [92]
Cl	CH <sub>2</sub>	Cl	111.8	155.39	Ref. [? ]

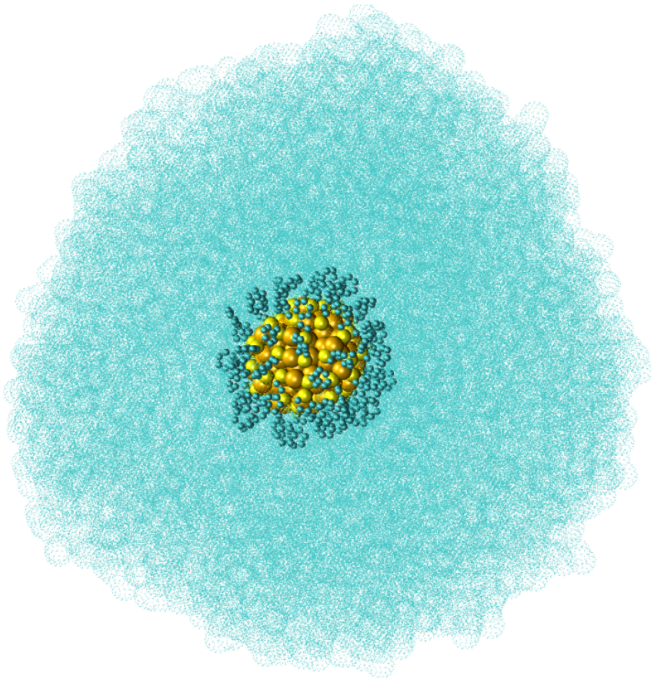


Figure 4.3. A single  $\text{Au}_{144}\text{PET}_{60}$  cluster in a solvent cloud of dichloromethane.

sphere was at least 3x the radius of the particle and that the solvent would maintain bulk density near the interface (see Table 4.5 for exact packing). At least 7 separate configurations of the nanoparticles were found before the random packing of each solvent.

Solvated particles were then brought to 250K using the Langevin Hull ensemble.[1] Once equilibrated with thermal coupling to the bath for at least 1 ns, the system was simulated without the coupling for 1 ns. The particle systems were simulated using RNEMD for 1 ns where a thermal flux was applied to find the resulting temperature gradient.

Pure solvent simulations were prepared through a simple ‘fcc’ builder using the bulk solvent density. Random seeds were used to create five separate simulations for three different simulation box lengths. These simulations were equilibrated to 250K using the canonical (NVT) ensemble for at least 1 ns followed by further relaxation

in the (NPT) ensemble for 1 ns. Finally, the pure solvent systems underwent at least 1 ns in the microcanonical (NVE) ensemble before undergoing a RNEMD simulation for 10 ns.

The pure gold systems followed the same protocol as the dichloromethane and toluene systems, except the temperature for the pure gold system is 1500K, above the melting point of bulk gold. After equilibration, the relevant thermal flux was applied for 3 ns. To achieve a similar temperature gradient across the three box sizes (for all bulk simulations), the applied thermal flux was adjusted, see Table 4.4. Depending on the size of the system, more time might be needed to allow a steady state temperature gradient to develop, all systems were ran to the longest time scale needed to achieve a steady state.

The average temperature of the system remained at 250K for the pure solvent, single nanoparticle, and nanoarray systems; and 1500K for the liquid gold simulations. In the pure solvent, single nanoparticle, and nanoarray systems this temperature preserved the solvent cloud close to the bulk density near the interface of the particle. Additionally, thermal coupling to the external temperature bath for the single nanoparticle systems was removed to avoid thermal interference with the imposed flux.

TABLE 4.4

Composition of the pure liquid simulations with box dimensions and average lambda values with standard error from 5 simulations.

System	atoms	$L_x$ (Å)	$L_y$ (Å)	$L_z$ (Å)	applied flux	time (ns)	$\lambda_{ave}$
Dichloromethane	2816	60.16	60.16	82.73	1E-7	10	$0.0263 \pm 7.0\text{E-}4$
	5632	60.16	60.16	169.1	5E-8	10	$0.0390 \pm 2.0\text{E-}3$
	8448	60.16	60.16	253.35	5E-8	10	$0.0595 \pm 4.6\text{E-}3$
Toluene	1764	62.3	62.3	80.1	1E-7	10	$0.1036 \pm 4.0\text{E-}3$
	3528	62.3	62.3	160.2	5E-8	10	$0.1147 \pm 1.0\text{E-}2$
	5292	62.3	62.3	240.5	5E-8	10	$0.1062 \pm 6.3\text{E-}3$
Gold	5040	32.03	30.82	106.4	6.5E-6	3	$0.3407 \pm 1.0\text{E-}2$
	10080	32.03	30.82	212.8	6.5E-6	3	$0.3800 \pm 1.9\text{E-}2$
	15120	32.03	30.82	319.26	6.5E-6	3	$0.3645 \pm 2.0\text{E-}2$

TABLE 4.5

Composition of solvated nanoparticles for interfacial thermal conductivity simulations.

	Dichloromethane	Toluene
atoms	4807	12075
packing radius ( $\text{\AA}$ )	52	85
average $\rho_{sim}^{r>20\text{\AA}} \text{ (g/cm}^3)$	1.33	1.74
$\rho_{solv}^{bulk} \text{ (g/cm}^3)$	1.33	0.87

The nanoarrays use eight different particle geometries, packed within the 2 particle x 2 particle x 2 particle array, with a center of mass to center of mass distance of 30  $\text{\AA}$ . These arrays were thermalized to 250K, then solvated with either toluene or dichloromethane with random seeds to create five different configurations of the solvent using packmol.[97] Solvated arrays were equilibrated at 250K in the canonical ensemble then further equilibrated for at least 1 ns in the microcanonical ensemble. These simple structures were replicated in the z-direction to create multiples of the unit cell, up to a 2x2x8 particle array, then equilibrated at 250K in the canonical ensemble and at least 1 ns in the microcanonical ensemble.

After equilibration the arrays were simulated with a thermal flux for at least 10 ns or until a steady state was reached. Similar to the bulk boxes, to achieve a similar temperature gradient across the box, the applied thermal flux was adjusted for the different array sizes.

All simulations were carried out using the open source molecular dynamics package OpenMD.[95] Thermal conductivity and interfacial thermal conductivity were calculated using methods described in works by Kuang *et. al.* for periodic systems,[56] and Stocker *et. al.* for non-periodic systems.[58]

TABLE 4.6  
Composition of nanoarray systems.

System	Au <sub>144</sub> PET <sub>60</sub>	DCM	Toluene	L <sub>x</sub> (Å)	L <sub>y</sub> (Å)	L <sub>z</sub> (Å)
2x2x2	8	1100	450	61	61	61
2x2x4	16	2200	900	61	61	122
2x2x6	24	3300	1350	61	61	183
2x2x8	32	4400	1800	61	61	244

#### 4.2.3 Calculating thermal conductivity

Thermal conductivity is related to the applied flux through the following:

$$\lambda = \frac{J_z}{\frac{\partial T}{\partial z}} = \frac{J_z}{m} \quad (4.3)$$

where  $J_z$  is the applied thermal flux and  $\frac{\partial T}{\partial z}$  is the slope from the temperature gradient that develops in the simulation. The thermal gradient created from the applied flux in a box of solvent is shown in Fig. 4.4. The red and blue bins are the hot and cold bins, respectively. The slope of the temperature gradient,  $m$ , is  $\frac{\partial T}{\partial z}$ .

In addition to finding the thermal conductivity of a material at different box lengths, the infinite box length thermal conductivity of the material is extrapolated using the following equation:

$$\frac{1}{\lambda_\infty} = \frac{1}{\lambda_L} + \frac{C}{L} \quad (4.4)$$

where  $C$  is a constant and  $L$  is the length of the simulation box in the z-direction.[68]

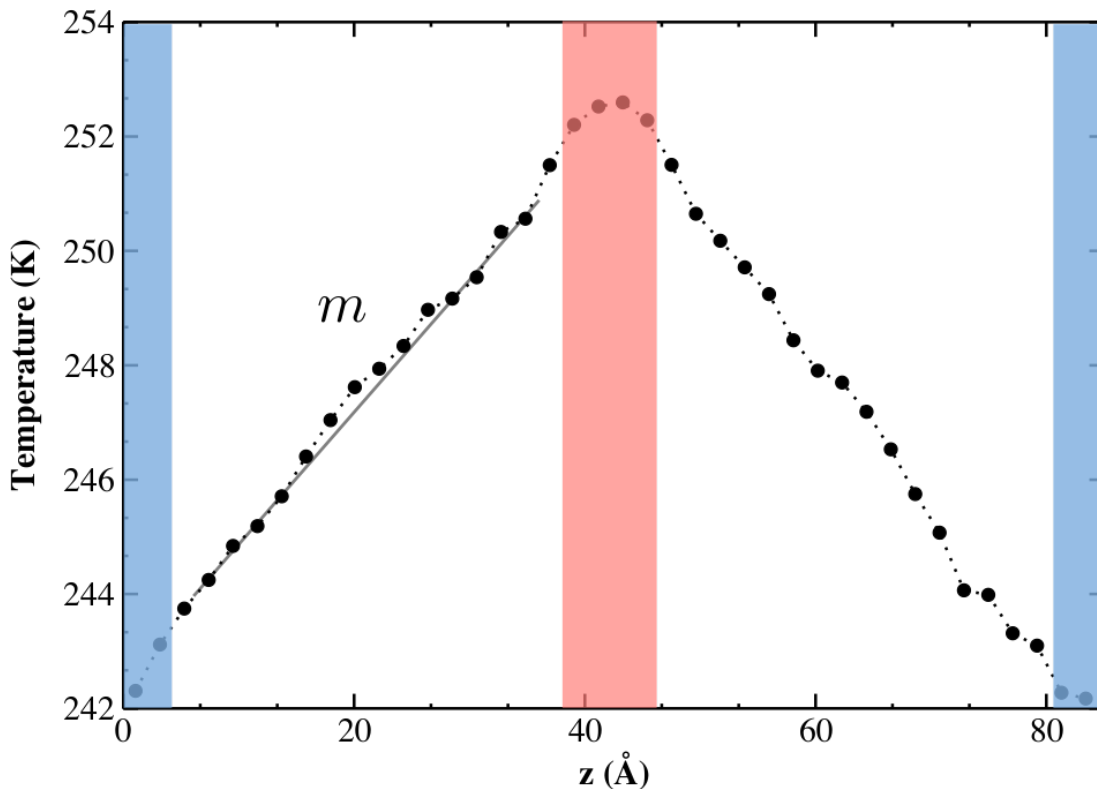


Figure 4.4. This figure is an example of the thermal gradient that develops in a bulk solvent system with a moderate flux. The red region is the “hot” bin and the two blue regions are the “cold” bins. The slope,  $m$ , that measures the temperature gradient is related to the thermal conductivity of the material,  $\lambda$ .

### 4.3 Results and Discussion

A prediction of the Hasselman and Johnson equation for a simple array of  $\text{Au}_{144}\text{PET}_{60}$  particles was found through simulating each components of the equation. The bulk gold conductivity is compared to a previous study looking at gold particles in an array. Ultimately, as found in previous work by Zanjani *et al.*[59] and Ong *et al.*[67], the volume fraction of the array is the essential piece to the predictive equation. While the interface is of a smaller importance to the prediction of the thermal conductivity of the material, the comparison of how the two solvents affect heat transport out of the nanoclusters confirms previous finding about solvent penetration being of paramount importance to thermal transport. In the following sections each of the individual components of the Hasselman and Johnson equation, as well as a prediction will be presented. Additionally, thermal conductivity of the arrays will be discussed in comparison to the predicted results.

#### 4.3.1 Bulk Solvent and Bulk Gold Conductivity

For the bulk dichloromethane and toluene solvent simulations, both where projected to a infinite thermal conductivity using Eq 4.4. As seen in Fig. 4.5, the box length dependent thermal conductivity is necessary for dichloromethane solvent. While the projection to an infinite box size using Eq. 4.4 is not supported by the data for toluene and liquid gold.

The thermal conductivity of the dichloromethane from the projection to an infinite box and the thermal conductivity average of the toluene boxes are shown in Fig. 4.6. The thermal conductivity of dichloromethane is extrapolated to be  $0.1084 \pm 0.0021 \text{ W/mK}$  and the conductivity of toluene is averaged to be  $0.1082 \pm 0.0054 \text{ W/mK}$ . If composition of the array is primarily solvent, the Hasselman and Johnson equation will give nearly the same conductivity for the array due to the solvents having matching  $\lambda$ 's. It is important to note that the applied flux was small enough

to not change the density of the solvent across the simulation box due to the ‘hot’ and ‘cold’ bins.

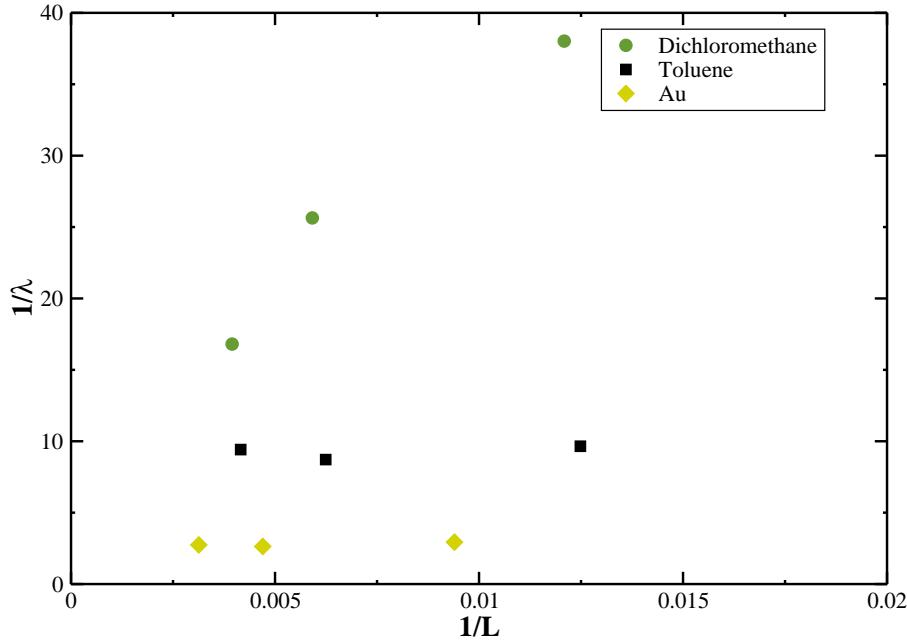


Figure 4.5. Parameters to Eq. 4.4 for bulk simulations of dichloromethane (green circles), toluene (black squares), and liquid gold (yellow diamonds). The y-axis,  $\lambda$  is in units of W/mK. The x-axis,  $L$  is in Å.

The bulk gold simulations are essential to finding  $\lambda_p$  from Eq. 4.1. Previous work from Ong *et al.*[67] used bulk gold thermal conductivity of  $1.8 \pm 0.3$  W/mK from simulations of a bulk ‘fcc’ gold at 300 K for simulations of a gold nanocrystal array. Their value will be compared to the conductivity of a bulk gold simulation

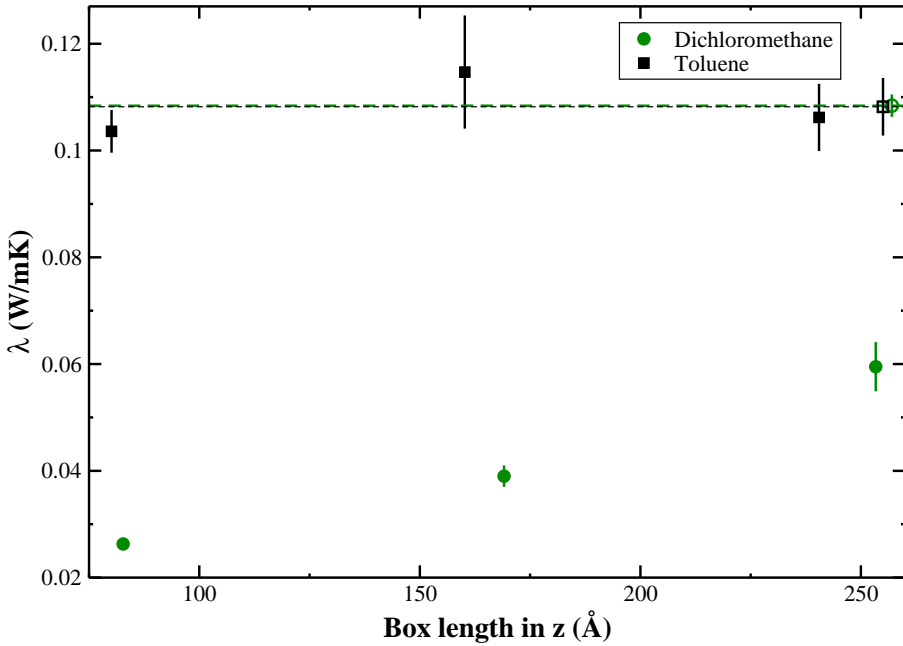


Figure 4.6. Bulk solvent  $\lambda$  as a function of simulation box length in  $z$  displays the trend in dichloromethane with increasing box size. The dashed lines and open symbols are the projected  $\lambda_\infty$  for dichloromethane and the average value for toluene.

at 1500 K, pass the melting point of the gold in QSC. QSC has a size dependent melting temperature and previous particles of slightly larger radius have been shown to display liquid like structures.[62] Experimentally, particles with  $N < 219$  have been seen with an approximate melting temperature of 500 K.[111] Additionally, it was proposed through extrapolating melting temperatures vs. diameter, that the  $\text{Au}_{144}\text{PET}_{60}$  cluster (with a diameter of  $\approx 18$  Å) would melt at approximately 600 K.[144] Hence the high temperature simulations of 100 Å, 200 Å, and 300 Å box length in  $z$  were computed and displayed a  $\lambda_p = 0.3787 \pm 0.02$  W/mK. The lower conductivity makes intuitive sense; when the gold melts the ballistic phonons traveling

through the gold lattice are disrupted and the transmission of the phonons decreases.

#### 4.3.2 Interfacial Thermal Conductivity

Experimentally difficult and computational complicated, the interfacial thermal conductance,  $G$ , for the particles was found in the two solvents. In an attempt to force the interfacial density of toluene in these single particle to more closely match the experimental bulk density, the solvent outside of the interfacial is about twice the density of bulk toluene. This was not an issue with the dichloromethane systems. Across the staple motif the thermal conductivity in the toluene was  $11.37 \pm 0.66$  MW/m<sup>2</sup>K, while in dichloromethane  $G = 74.73 \pm 4.28$  MW/m<sup>2</sup>K.

#### 4.3.3 Prediction of Array Thermal Conductivity

Along with the components of the equation for bulk thermal conductivity, there is a geometric feature,  $v_p$ , the partial volume of the  $\text{Au}_{144}\text{PET}_{60}$  particles in the array. The partial volume is approximated through the effective radius of the particles, which is taken from the average of the radius for only the gold atoms and the radius of the total particle. This approximations gives a partial volume of 22.5%. A total particle volume which includes all the ligand layer, allows for solvent to penetrate into the particle and would overestimate the volume fraction of the particles for a  $v_p = 47.7\%$ .

Using the parameters found,  $\lambda_s$ ,  $\lambda_p$ ,  $G$ , and  $v_p$ , the Hasselman and Johnson equation can be used to predict the thermal conductivity of the array. Using the bulk gold thermal conductivity reported by Ong *et al.* for gold at 300 K and the value calculated here for 1500 K, the array thermal conductivity can be found in Table 4.7. As seen in previous work,[59, 60, 67] the volume fraction of the particles is the main determining factor of the thermal conductivity. With the small  $v_p$ ,  $\lambda_s$  dominates  $\lambda_e$ , thus there is a similar conductivity for the array across solvent (since  $\lambda_s$  is nearly the

	$\lambda_p^{1500K}$	$\lambda_p^{300K}$
$\lambda_e^{DCM}$	0.1184	0.1256
$\lambda_e^{Toluene}$	0.1182	0.1254

TABLE 4.7

The Hasselman and Johnson prediction for thermal conductivity of the  $\text{Au}_{144}\text{PET}_{60}$  array using the gold thermal conductivity at 1500 K and 300 K. The array prediction for dichloromethane and toluene using the bulk thermal conductivity of each solvent.

same for the bulk thermal conductivity) and  $\lambda_p$ .

#### 4.3.4 Simulations of Array

Preliminary results of the smallest constructed array display behavior that indicate that Eq. 4.1 might be missing a more complex component of the system. The smallest system (2x2x2) in dichloromethane was simulated to find  $\lambda = 0.0307 \pm 0.009$  W/mK. This is far below the predicted value of 0.1184 W/mK, but the dichloromethane bulk solvent displayed box length dependent thermal conductivity. Therefore, it is possible that with larger arrays in dichloromethane, a box length dependent thermal conductivity will be seen. Additionally, it is possible that the dichloromethane in the arrays behaves differently than the bulk fluid and might have thermal properties more similar to a confined liquid.

#### 4.4 Conclusions

While there is still more that needs to be explained in the nanoarrays of the  $\text{Au}_{144}\text{PET}_{60}$  particles, interesting results have been found in the predictive Hasselman and Johnson model. To use the model, each component of the nanoarray was simulated to find the relevant thermal quantity. As found in previous works, the main component of the Eq. 4.1 is  $v_p$ . The geometric arrangement of the array is the most important aspect contributing to the thermal conductance of the material.

In finding the component pieces of Eq. 4.1, interest results were found for the pure liquid simulations and the interfacial thermal conductivity of the particle. The two solvents not having agreeing box length dependent behavior brings interesting questions about the density dependent thermal conductivity of liquids. Similarly, the immense difference for  $G$  between the two solvent interfaces with the particle, brings about questions of what most important ligand–solvent design.

## CHAPTER 5

### CONCLUSION

In this dissertation applications of Reverse Non-Equilibrium Molecular Dynamics and the Langenvin Hull method were applied to gold nanoparticle systems. Gold nanoparticle systems have well characterized optical properties, but less explored thermal properties, which are typically important after the electronic excitation. The simulations in previous chapters explored the effect of ligand rigidity, gold particle morphology, and staple motif effects in nanoarrays through molecular dynamics.

Understanding how the capping agent, or ligand, on gold nanoparticles interacts with the particle and solvent environment is essential to predicting behavior of nanoparticles in a given system. The effect of adding rigidity to the ligand layer, changed the penetration accessibility of the interfacial solvent. With a more rigid ligand, generally the solvent has an increased penetration in the ligand layer. This lead to a stronger vibrational overlap of the ligand and solvent, and thus a better thermal transport. Additionally, the addition of the ligand layer aids interfacial thermal conductivity. The sulfur on the thiolate ligand acts as a strong conduit for heat from the particle to the solvent.

Though the ligand layer is experimentally interesting and has promising characteristics for tailoring a nanoparticle for desired thermal and optical properties, a bare particle gives insight to how the morphology of the gold particle affects thermal transport. From simulations of spheres, cuboctahedra, and icosahedra; the surface of the gold particle is essential to thermal transport from bare particles. Furthermore, work in chapter 3 displayed that the underlying lattice carries important information

on the available low frequency phonon modes.

In an effort examine both the ligand and undercoordination of gold atoms at the surface within the same system, chapter 4 investigates the effect of the staple motif on  $\text{Au}_{144}\text{PET}_{60}$  nanoclusters. The nanoparticles were examined in two different solvents; one polar and one non-polar; in single particle systems and in arrays. While the array systems have inconclusive results, the single particle systems display interesting behavior in respect to the ligand/solvent interaction. While the staple motif might have increased the conductivity through the undercoordinated gold atoms in the ligand, the solvent ultimately was the limiting piece of the system. Additionally, the solvent thermal conductivity due to the partial volume becomes the dominating factor in the predictive equation for thermal conductivity through an array of  $\text{Au}_{144}\text{PET}_{60}$  particles.

In the future, work on more biologically relevant systems would be an interesting avenue to explore. With a new polarizable metal model (DR-EAM), the gold substrate would be able to more appropriately interact with polar molecules. Thus, a good starting system would be a gold slab displaying (111) facets in water.

To systematically determine how polarization affects thermal conductivity in a simple gold/water system, each of the components should be tested individually. Therefore the following systems would be examined:  $\text{Au}(\text{EAM})/\text{H}_2\text{O}(\text{TIP-4P})$ ,  $\text{Au}(\text{EAM})/\text{H}_2\text{O}(\text{TIP-4P-fq})$ ,  $\text{Au}(\text{DR-EAM})/\text{H}_2\text{O}(\text{TIP-4P})$ , and  $\text{Au}(\text{DR-EAM})/\text{H}_2\text{O}(\text{TIP-4P-fq})$ . If the polarization of the gold and water effects the the interfacial thermal conductivity of the system, moving forward with biologically relevant systems would be the next course of action. Various interesting ligands such as: thiolated PEG, citrate, Cetyl trimethylammonium bromide(CTAB), and different carboxylic acid moieties; could be tested on planar and spherical systems. The differences in these could then be identified to tailor nanoparticles for different thermal needs.

In addition to the further work needed in the gold nanoparticle systems, the

trend in pure solvents would be an interesting avenue to explore. In chapter 4, the two solvents (dichloromethane and toluene) had very different thermal conductivity values at the three box lengths simulated but had the same infinite box length bulk thermal conductivity. Dichloromethane, with a density of  $\approx 2x$  that of toluene, had a clear box length dependence, while toluene did not. It would be interesting to follow these simulations with a range of different common solvents, with known thermal conductivities, and look not only at the box dependences but a normal mode analysis. In the more dense fluids it is possible that the imaginary frequencies would be more heavily populated, leading to higher bulk thermal conductivities.

The work presented in this work has shown significant progress in identifying the trends that are important for controlling the thermal properties of gold nanoparticles. Moving forward, work with polarizable force fields, biologically relevant ligands and capping agents, and elucidating trends in solvent thermal conductivity would move nanoparticle design forward.

## BIBLIOGRAPHY

1. Vardeman, C. F.; Stocker, K. M.; Gezelter, J. D. The Langevin Hull: Constant pressure and temperature dynamics for nonperiodic systems. *J. Chem. Theory Comput.* **2011**, *7*, 834–842.
2. Martin, M. G.; Siepmann, J. I. Transferable potentials for phase equilibria. 1. United-atom description of n-alkanes. *J. Phys. Chem. B* **1998**, *102*, 2569–2577.
3. Wick, C. D.; Martin, M. G.; Siepmann, J. I. Transferable potentials for phase equilibria. 4. United-atom description of linear and branched alkenes and alkylbenzenes. *J. Phys. Chem. B* **2000**, *104*, 8008–8016.
4. Lubna, N.; Kamath, G.; Potoff, J. J.; Rai, N.; Siepmann, J. I. Transferable potentials for phase equilibria. 8. United-atom description for thiols, sulfides, disulfides, and thiophene. *J. Phys. Chem. B* **2005**, *109*, 24100–24107.
5. Luedtke, W. D.; Landman, U. Structure and thermodynamics of self-assembled monolayers on gold nanocrystallites. *J. Phys. Chem. B* **1998**, *102*, 6566–6572.
6. Schapotschnikow, P.; Pool, R.; Vlugt, T. J. Selective adsorption of alkyl thiols on gold in different geometries. *Comput. Phys. Commun.* **2007**, *177*, 154 – 157.
7. Hautman, J.; Klein, M. L. Simulation of a monolayer of alkyl thiol chains. *J. Chem. Phys.* **1989**, *91*, 4994–5001.
8. Chen, G. *Nanoscale Energy Transport and Conversion*; Oxford University Press: New York, 2005.
9. Goldstein, H.; Poole, C.; Safko, J. *Classical Mechanics*, 3rd ed.; Addison Wesley: San Francisco, 2001.
10. Kittel, C. *Introduction to Solid State Physics*; John Wiley and Sons: New York, 2005.
11. Hsieh, W.-P.; Lyons, A. S.; Pop, E.; Keblinski, P.; Cahill, D. G. Pressure tuning of the thermal conductance of weak interfaces. *Phys. Rev. B* **2011**, *84*, 184107.
12. Stoner, R. J.; Maris, H. J. Kapitza conductance and heat flow between solids at temperatures from 50 to 300 K. *Phys. Rev. B* **1993**, *48*, 16373–16387.

13. Monachon, C.; Weber, L.; Dames, C. Thermal boundary conductance : A materials science perspective. *Annu. Rev. Mater. Res.* **2016**, *8*, 1–31.
14. Little, W. A. The transport of heat between dissimilar solids at low temperatures. *Can. J. Phys.* **1959**, *37*, 334–349.
15. Graff, K. F. *Wave Motion in Elastic Solids*; Dover: New York, 1975.
16. Prasher, P. E., Ravi S. Phelan Prediction of thermal boundary resistance. *J. Heat Transfer* **2000**, *123*, 105–112.
17. Prasher, R. Acoustic mismatch model for thermal contact resistance of van der Waals contacts. *Applied Physics Letters* **2009**, *94*, 041905.
18. Lyeo, H.-K.; Cahill, D. G. Thermal conductance of interfaces between highly dissimilar materials. *Phys. Rev. B* **2006**, *73*, 144301.
19. Swartz, E. T.; Pohl, R. O. Thermal boundary resistance. *Rev. Mod. Phys.* **1989**, *61*, 605–668.
20. Reddy, P.; Castelino, K.; Majumdar, A. Diffuse mismatch model of thermal boundary conductance using exact phonon dispersion. *Appl. Phys. Lett.* **2005**, *87*, 211908.
21. Beechem, T.; Graham, S.; Hopkins, P.; Norris, P. Role of interface disorder on thermal boundary conductance using a virtual crystal approach. *Appl. Phys. Lett.* **2007**, *90*, 054104.
22. Hopkins, P. E.; Duda, J. C.; Petz, C. W.; Floro, J. A. Controlling thermal conductance through quantum dot roughening at interfaces. *Phys. Rev. B* **2011**, *84*, 035438.
23. Hopkins, P. E.; Duda, J. C.; Norris, P. M. Anharmonic phonon interactions at interfaces and contributions to thermal boundary conductance. *J. Heat Transfer* **2011**, *133*, 062401.
24. Stevens, R. J.; Smith, A. N.; Norris, P. M. Measurement of thermal boundary conductance of a series of metal-dielectric interfaces by the transient thermoreflectance technique resistance of van der Waals contacts. *J. Heat Transfer* **2005**, *127*, 315–322.
25. Leach, A. *Molecular Modeling: Principles and Applications*, 2nd ed.; Pearson Educated Limited: Harlow, England, 2001.
26. Qi, Y.; Çağın, T.; Kimura, Y.; Goddard III, W. A. Molecular-dynamics simulations of glass formation and crystallization in binary liquid metals: Cu-Ag and Cu-Ni. *Phys. Rev. B* **1999**, *59*, 3527–3533.

27. Foiles, S. M.; Baskes, M. I.; Daw, M. S. Embedded-atom-method functions for the fcc metals Cu, Ag, Au, Ni, Pd, Pt, and their alloys. *Phys. Rev. B* **1986**, *33*, 7983–7991.
28. Kohanoff, J.; Caro, A.; Finnis, M. An isothermal-isobaric Langevin thermostat for simulating nanoparticles under pressure: Application to Au clusters. *ChemPhysChem* **2005**, *6*, 1848–1852.
29. Baltazar, S. E.; Romero, A. H.; Rodriguez-Lopez, J. L.; Terrones, H.; Martonak, R. Assessment of isobaric-isothermal (NPT) simulations for finite systems. *Comp. Mat. Sci.* **2006**, *37*, 526–536.
30. Heyes, D. M. Transport coefficients of Lennard-Jones fluids: A molecular-dynamics and effective-hard-sphere treatment. *Phys. Rev. B* **1988**, *37*, 5677–5696.
31. Massobrio, C.; Ciccotti, G. Lennard-Jones triple-point conductivity via weak external fields. *Phys. Rev. A* **1984**, *30*, 3191–3197.
32. Helfand, E. Transport coefficients from dissipation in a canonical ensemble. *Phys. Rev.* **1960**, *119*, 1–9.
33. Viscardy, S.; Servantie, J.; Gaspard, P. Transport and helfand moments in the Lennard-Jones fluid. II. thermal conductivity. *J. Chem. Phys.* **2007**, *126*, 184513.
34. Che, J.; Cagin, T.; Deng, W.; III, W. A. G. Thermal conductivity of diamond and related materials from molecular dynamics simulations. *J. Chem. Phys.* **2000**, *113*, 6888–6900.
35. Kinaci, A.; Haskins, J. B.; Çağın, T. On calculation of thermal conductivity from Einstein relation in equilibrium molecular dynamics. *J. Chem. Phys.* **2012**, *137*, 014106.
36. Backer, J. A.; Lowe, C. P.; Hoefsloot, H. C. J.; Iedema, P. D. Poiseuille flow to measure the viscosity of particle model fluids. *J. Chem. Phys.* **2005**, *122*, 154503.
37. Hess, B. Determining the shear viscosity of model liquids from molecular dynamics simulations. *J. Chem. Phys.* **2002**, *116*, 209–217.
38. Picalek, J.; Kolafa, J. Shear viscosity of ionic liquids from non-equilibrium molecular dynamics simulation. *Mol. Simul.* **2009**, *35*, 685–690.
39. Vasquez, V. R.; Macedo, E. A.; Zabaloy, M. S. Lennard-Jones viscosities in wide ranges of temperature and density: Fast calculations using a steady-state periodic perturbation method. *Int. J. Thermophys.* **2004**, *25*, 1799–1818.

40. Evans, D. J. Homogeneous NEMD algorithm for thermal conductivity – Application of non-canonical linear response theory. *Phys. Lett. A* **1982**, *91*, 457–460.
41. Erpenbeck, J. J. Shear viscosity of the hard-sphere fluid via nonequilibrium molecular dynamics. *Phys. Rev. Lett.* **1984**, *52*, 1333–1335.
42. Evans, D. J. Thermal conductivity of the Lennard-Jones fluid. *Phys. Rev. A* **1986**, *34*, 1449–1453.
43. Vogelsang, R.; Hoheisel, G.; Luckas, M. Shear viscosity and thermal conductivity of the Lennard-Jones liquid computed using molecular dynamics and predicted by a memory function model for a large number of states. *Mol. Phys.* **1988**, *64*, 1203–1213.
44. Maginn, E. J.; Bell, A. T.; Theodorou, D. N. Transport diffusivity of methane in silicalite from equilibrium and nonequilibrium simulations. *J. Phys. Chem.* **1993**, *97*, 4173–4181.
45. Schelling, P. K.; Phillipot, S. R.; Kebinski, P. Comparison of atomic-level simulation methods for computing thermal conductivity. *Phys. Rev. B* **2002**, *65*, 144306.
46. Berthier, L.; Barrat, J. L. Nonequilibrium dynamics and fluctuation-dissipation relation in a sheared fluid. *J. Chem. Phys.* **2002**, *116*, 6228–6242.
47. Evans, D. J.; Searles, D. J. The fluctuation theorem. *Adv. Phys.* **2002**, *51*, 1529–1585.
48. Jiang, H.; Myshakin, E. M.; Jordan, K. D.; Warzinski, R. P. Molecular dynamics simulations of the thermal conductivity of methane hydrate. *J. Phys. Chem. B* **2008**, *112*, 10207–10216.
49. Müller-Plathe, F. A simple nonequilibrium molecular dynamics method for calculating the thermal conductivity. *J. Chem. Phys.* **1997**, *106*, 6082–6085.
50. Müller-Plathe, F. Reversing the perturbation in nonequilibrium molecular dynamics: An easy way to calculate the shear viscosity of fluids. *Phys. Rev. E* **1999**, *59*, 4894–4898.
51. Kuang, S.; Gezelter, J. D. Velocity shearing and scaling RNEMD: A minimally perturbing method for simulating temperature and momentum gradients. *Mol. Phys.* **2012**, *110*, 691–701.
52. Zhang, M.; Lussetti, E.; de Souza, L. E. S.; Müller-Plathe, F. Thermal Conductivities of Molecular Liquids by Reverse Nonequilibrium Molecular Dynamics. *J. Phys. Chem. B* **2005**, *109*, 15060–15067.
53. Tenney, C. M.; Maginn, E. J. Limitations and recommendations for the calculation of shear viscosity using reverse nonequilibrium molecular dynamics. *J. Chem. Phys.* **2010**, *132*, 014103.

54. Patel, H. A.; Garde, S.; Kebelinski, P. Thermal resistance of nanoscopic liquid-liquid interfaces: dependence on chemistry and molecular architecture. *Nano Lett.* **2005**, *5*, 2225–2231.
55. Shenogina, N.; Godawat, R.; Kebelinski, P.; Garde, S. How wetting and adhesion affect thermal conductance of a range of hydrophobic to hydrophilic aqueous interfaces. *Phys. Rev. Lett.* **2009**, *102*, 156101.
56. Kuang, S.; Gezelter, J. D. Simulating interfacial thermal conductance at metal-solvent interfaces: The role of chemical capping agents. *J. Phys. Chem. C* **2011**, *115*, 22475–22483.
57. Stocker, K. M.; Gezelter, J. D. Simulations of heat conduction at thiolate-capped gold surfaces: the role of chain length and solvent penetration. *J. Phys. Chem. C* **2013**, *117*, 7605–7612.
58. Stocker, K. M.; Gezelter, J. D. A method for creating thermal and angular momentum fluxes in nonperiodic simulations. *J. Chem. Theory Comput.* **2014**, *10*, 1878–1886.
59. Zanjani, M. B.; Lukes, J. R. Phonon dispersion and thermal conductivity of nanocrystal superlattices using three-dimensional atomistic models. *J. Appl. Phys.* **2014**, *115*.
60. Liu, M.; Ma, Y.; Wang, R. Y. Modifying thermal transport in colloidal nanocrystal solids with surface chemistry. *ACS Nano* **2015**, *9*, 12079–12087.
61. Wilhelmsen, Ø.; Trinh, T. T.; Kjelstrup, S.; Erp, T. S. V.; Bedeaux, D. Heat and mass transfer across interfaces in complex nanogeometries. *Phys. Rev. Lett.* **2015**, *114*, 065901.
62. Stocker, K. M.; Neidhart, S. M.; Gezelter, J. D. Interfacial thermal conductance of thiolate-protected gold nanospheres. *J. Appl. Phys.* **2016**, *119*, 025106.
63. Tascini, A. S.; Armstrong, J.; Chiavazzo, E.; Fasano, M.; Asinari, P.; Bresme, F. Thermal transport across nanoparticle-fluid interfaces: the interplay of interfacial curvature and nanoparticle-fluid interactions. *Phys. Chem. Chem. Phys.* **2017**, *19*, 3244–3253.
64. Wilson, O.; Hu, X.; Cahill, D.; Braun, P. Colloidal metal particles as probes of nanoscale thermal transport in fluids. *Phys. Rev. B* **2002**, *66*, 224301.
65. Ong, W.-L.; Rupich, S. M.; Talapin, D. V.; McGaughey, A. J. H.; Malen, J. A. Surface chemistry mediates thermal transport in three-dimensional nanocrystal arrays. *Nat. Mater.* **2013**, *12*, 410–415.
66. Kuang, S.; Gezelter, J. D. Simulating interfacial thermal conductance at metal-solvent interfaces: The role of chemical capping agents. *J. Phys. Chem. C* **2011**, *115*, 22475–22483.

67. Ong, W.-L.; Majumdar, S.; Malen, J. A.; McGaughey, A. J. H. Coupling of organic and inorganic vibrational states and their thermal transport in nanocrystal arrays. *J. Phys. Chem. C* **2014**, *118*, 7288–7295.
68. Hannah, D. C.; Gezelter, J. D.; Schaller, R. D.; Schatz, G. C. Reverse non-equilibrium molecular dynamics demonstrate that surface passivation controls thermal transport at semiconductor-solvent interfaces. *ACS Nano* **2015**, *9*, 6278–6287.
69. Park, J.; Cahill, D. G. Plasmonic sensing of heat transport at solid-liquid interfaces. *J. Phys. Chem. C* **2016**, *120*, 2814–2821.
70. Pandey, H. D.; Leitner, D. M. Influence of thermalization on thermal conduction through molecular junctions: Computational study of PEG oligomers. *J. Chem. Phys.* **2017**, *147*, 084701.
71. Park, J.; Huang, J.; Wang, W.; Murphy, C. J.; Cahill, D. G. Heat transport between Au nanorods, surrounding liquids, and solid supports. *J. Phys. Chem. C* **2012**, *116*, 26335–26341.
72. Ge, Z.; Cahill, D. G.; Braun, P. Thermal Conductance of Hydrophilic and Hydrophobic Interfaces. *Phys. Rev. Lett.* **2006**, *96*, 186101.
73. Neidhart, S. M.; Gezelter, J. D. Thermal transport is influenced by nanoparticle morphology: A molecular dynamics study. *J. Phys. Chem. C* **2017**, *acs.jpcc.7b12362*.
74. Ge, Z.; Cahill, D. G.; Braun, P. V. AuPd metal nanoparticles as probes of nanoscale thermal transport in aqueous solution. *J. Phys. Chem. B* **2004**, *108*, 18870–18875.
75. Wang, Z.; Carter, J. A.; Lagutchev, A.; Koh, Y. K.; Seong, N.-H.; Cahill, D. G.; Dlott, D. D. Ultrafast flash thermal conductance of molecular chains. *Science* **2007**, *317*, 787–790.
76. Schmidt, A. J.; Alper, J. D.; Chiesa, M.; Chen, G.; Das, S. K.; Hamad-Schifferli, K. Probing the gold nanorod-ligand-solvent interface by plasmonic absorption and thermal decay. *J. Phys. Chem. C* **2008**, *112*, 13320–13323.
77. Juvé, V.; Scardamaglia, M.; Maioli, P.; Crut, A.; Merabia, S.; Joly, L.; Del Fatti, N.; Vallée, F. Cooling dynamics and thermal interface resistance of glass-embedded metal nanoparticles. *Phys. Rev. B* **2009**, *80*, 195406.
78. Alper, J.; Hamad-Schifferli, K. Effect of ligands on thermal dissipation from gold nanorods. *Langmuir* **2010**, *26*, 3786–3789.
79. Harikrishna, H.; Ducker, W. A.; Huxtable, S. T. The influence of interface bonding on thermal transport through solid–liquid interfaces. *Appl. Phys. Lett.* **2013**, *102*, 251606.

80. Cahill, D. G.; Ford, W. K.; Goodson, K. E.; Mahan, G. D.; Majumdar, A.; Maris, H. J.; Merlin, R.; Phillpot, S. R. Nanoscale thermal transport. *J. Appl. Phys.* **2003**, *93*, 793–818.
81. Losego, M. D.; Grady, M. E.; Sottos, N. R.; Cahill, D. G.; Braun, P. V. Effects of chemical bonding on heat transport across interfaces. *Nat. Mater.* **2012**, *11*, 502–506.
82. Soussi, J.; Volz, S.; Palpant, B.; Chalopin, Y. A detailed microscopic study of the heat transfer at a water gold interface coated with a polymer. *Appl. Phys. Lett.* **2015**, *106*.
83. Ge, Z.; Cahill, D. G.; Braun, P. V. Thermal conductance of hydrophilic and hydrophobic interfaces. *Phys. Rev. Lett.* **2006**, *96*, 186101.
84. Kikugawa, G.; Ohara, T.; Kawaguchi, T.; Torigoe, E.; Hagiwara, Y.; Matsumoto, Y. A molecular dynamics study on heat transfer characteristics at the interfaces of alkanethiolate self-assembled monolayer and organic solvent. *J. Chem. Phys.* **2009**, *130*, 074706.
85. Tian, Z.; Marconnet, A.; Chen, G. Enhancing solid-liquid interface thermal transport using self-assembled monolayers. *Appl. Phys. Lett.* **2015**, *106*, 211602.
86. Henz, B. J.; Hawa, T.; Zachariah, M. R. Mechano-chemical stability of gold nanoparticles coated with alkanethiolate SAMs. *Langmuir* **2008**, *24*, 773–783.
87. Badia, A.; Singh, S.; Demers, L.; Cuccia, L.; Brown, G. R.; Lennox, R. B. Self-assembled monolayers on gold nanoparticles. *Chem. Eur. J.* **1996**, *2*, 359–363.
88. Badia, A.; Gao, W.; Singh, S.; Demers, L.; Cuccia, L.; Reven, L. Structure and chain dynamics of alkanethiol-capped gold colloids. *Langmuir* **1996**, *12*, 1262–1269.
89. Badia, A.; Demers, L.; Dickinson, L.; Morin, F. G.; Lennox, R. B.; Reven, L. Gold-sulfur interactions in alkylthiol self-assembled monolayers formed on gold nanoparticles studied by solid-state NMR. *J. Am. Chem. Soc.* **1997**, *119*, 11104–11105.
90. Badia, A.; Cuccia, L.; Demers, L.; Morin, F.; Lennox, R. B. Structure and dynamics in alkanethiolate monolayers self-assembled on gold nanoparticles: A DSC, FT-IR, and Deuterium NMR Study. *J. Am. Chem. Soc.* **1997**, *119*, 2682–2692.
91. Badia, A.; Lennox, R. B.; Reven, L. A dynamic view of self-assembled monolayers. *Acc. Chem. Res.* **2000**, *33*, 475–481.
92. Jorgensen, W. L.; Maxwell, D. S.; Tirado-Rives, J. Development and testing of the OPLS all-atom force field on conformational energetics and properties of organic liquids. *J. Am. Chem. Soc.* **1996**, *118*, 11225–11236.

93. Becke, A. D. Density-functional thermochemistry. III. The role of exact exchange. *J. Chem. Phys.* **1993**, *98*, 5648–5652.
94. Lee, C.; Yang, W.; Parr, R. G. Development of the Colle-Salvetti correlation-energy formula into a functional of the electron density. *Phys. Rev. B* **1988**, *37*, 785–789.
95. Gezelter, J. D. et al. OpenMD, an Open Source Engine for Molecular Dynamics. Available at: <http://openmd.org> (Version 2.5, accessed August 20, 2017).
96. Meineke, M. A.; Vardeman, C. F.; Lin, T.; Fennell, C. J.; Gezelter, J. D. OOPSE: An object-oriented parallel simulation engine for molecular dynamics. *J. Comp. Chem.* **2005**, *26*, 252–271.
97. Martínez, L.; Andrade, R.; Birgin, E. G.; Martínez, J. M. PACKMOL: A package for building initial configurations for molecular dynamics simulations. *J. Comput. Chem.* **2009**, *30*, 2157–2164.
98. Steinhardt, P. J.; Nelson, D. R.; Ronchetti, M. Bond-orientational order in liquids and glasses. *Phys. Rev. B* **1983**, *28*, 784–804.
99. Vardeman, C. F.; Gezelter, J. D. Simulations of laser-induced glass formation in Ag-Cu nanoparticles. *J. Phys. Chem. C* **2008**, *112*, 3283–3293.
100. Segal, D.; Nitzan, A.; Hänggi, P. Thermal conductance through molecular wires. *J. Chem. Phys.* **2003**, *119*, 6840–6855.
101. Young, D. A.; Maris, H. J. Lattice-dynamical calculation of the Kapitza resistance between fcc lattices. *Phys. Rev. B* **1989**, *40*, 3685–3693.
102. Schmidt, A. J.; Collins, K. C.; Minnich, A. J.; Chen, G. Thermal conductance and phonon transmissivity of metal-graphite interfaces. *J. Appl. Phys.* **2010**, *107*, 104907.
103. Shin, S.; Kaviany, M.; Desai, T.; Bonner, R. Roles of atomic restructuring in interfacial phonon transport. *Phys. Rev. B* **2010**, *82*, 081302.
104. Meng, F.; Elsahati, M.; Liu, J.; Richards, R. F. Thermal resistance between amorphous silica nanoparticles. *J. Appl. Phys.* **2017**, *121*, 194302.
105. Schmidt, A. J.; Collins, K. C.; Minnich, A. J.; Chen, G. Thermal conductance and phonon transmissivity of metal-graphite interfaces. *J. Appl. Phys.* **2010**, *107*.
106. Norris, P. M.; Le, N. Q.; Baker, C. H. Tuning phonon transport : From interfaces to nanostructures. *J. Heat Transfer* **2013**, *135*, 1–13.

107. Han, H.; Schlawitschek, C.; Katyal, N.; Stephan, P.; Gambaryan-Roisman, T.; Leroy, F.; Müller-Plathe, F. Solid–liquid interface thermal resistance affects the evaporation rate of droplets from a surface: A study of perfluorohexane on chromium using molecular dynamics and continuum theory. *Langmuir* **2017**, *33*, 5336–5343.
108. Giri, A.; Braun, J. L.; Hopkins, P. E. Implications of interfacial bond strength on the spectral contributions to thermal boundary conductance across solid, liquid, and gas interfaces: A molecular dynamics study. *J. Phys. Chem. C* **2016**, *120*, 24847–24856.
109. Bhanushali, S.; Jason, N. N.; Ghosh, P.; Ganesh, A.; Simon, G. P.; Cheng, W. Enhanced thermal conductivity of copper nanofluids: The effect of filler geometry. *ACS Appl. Mater. Interfaces* **2017**, *9*, 18925–18935.
110. Yadav, H. O. S.; Chakravarty, C. Thiolated gold nanoparticle solvation in near-critical fluids: The role of density, temperature, and topology. *J. Chem. Phys.* **2017**, *146*, 174902.
111. Ercolessi, F.; Andreoni, W.; Tosatti, E. Melting of small gold particles: Mechanism and size effects. *Phys. Rev. Lett.* **1991**, *66*, 911–914.
112. Myshlyavtsev, A. V.; Stishenko, P. V. Relative stability of icosahedral and cuboctahedral metallic nanoparticles. *Adsorption* **2013**, *19*, 795–801.
113. Saucedo, H. E.; Garzón, I. L. Structural determination of metal nanoparticles from their vibrational (phonon) density of states. *J. Phys. Chem. C* **2015**, *119*, 10876–10880.
114. Wang, Y.; Teitel, S.; Dellago, C. Melting and equilibrium shape of icosahedral gold nanoparticles. *Chem. Phys. Lett.* **2004**, *394*, 257–261.
115. Jorgensen, W. L. In *The Encyclopedia of Computational Chemistry*; v. R. Schleyer, *et al.*, P., Ed.; John Wiley & Sons: New York, 1998; Vol. 3; pp 1986–1989.
116. Häkkinen, H. The gold–sulfur interface at the nanoscale. *Nat. Chem.* **2012**, *4*, 443.
117. Sardar, R.; Funston, A. M.; Mulvaney, P.; Murray, R. W. Gold Nanoparticles: Past, Present, and Future. *Langmuir* **2009**, *25*, 13840 – 13851.
118. Jin, R. Quantum sized, thiolate-protected gold nanoclusters. *Nanoscale* **2010**, *2*, 343–362.
119. Tsukuda, T. Toward an atomic-level understanding of size-specific properties of protected and stabilized gold clusters. *Bull. Chem. Soc. Jpn.* **2012**, *85*, 151–168.

120. Lopez-Acevedo, O.; Clayborne, P. A.; Häkkinen, H. Electronic structure of gold, aluminum, and gallium superatom complexes. *Phys. Rev. B* **2011**, *84*, 1–6.
121. Walter, M.; Akola, J.; Lopez-Acevedo, O.; Jadzinsky, P. D.; Calero, G.; Ackerson, C. J.; Whetten, R. L.; Gronbeck, H.; Hakkinen, H. A unified view of ligand-protected gold clusters as superatom complexes. *Proc. Natl. Acad. Sci.* **2008**, *105*, 9157–9162.
122. Cui, M.; Zhao, Y.; Song, Q. Synthesis, optical properties and applications of ultra-small luminescent gold nanoclusters. *Trends Anal. Chem.* **2014**, *57*, 73–82.
123. Chen, X.; Häkkinen, H. Protected but accessible: Oxygen activation by a calixarene-stabilized undecagold cluster. *J. Am. Chem. Soc.* **2013**, *135*, 12944–12947.
124. Lopez-Acevedo, O.; Kacprzak, K. A.; Akola, J.; Häkkinen, H. Quantum size effects in ambient CO oxidation catalysed by ligand-protected gold clusters. *Nat. Chem.* **2010**, *2*, 329–334.
125. Dong, A.; Chen, J.; Ye, X.; Kikkawa, J. M.; Murray, C. B. Enhanced thermal stability and magnetic properties in NaCl-Type FePt-MnO binary nanocrystal superlattices. *Journal of the American Chemical Society* **2011**, *133*, 13296–13299.
126. Podsiadlo, P.; Krylova, G.; Lee, B.; Critchley, K.; Gosztola, D. J.; Talapin, D. V.; Ashby, P. D.; Shevchenko, E. V. The role of order, nanocrystal size, and capping ligands in the collective mechanical response of three-dimensional nanocrystal solids. *J. Am. Chem. Soc.* **2010**, *132*, 8953–8960.
127. Shevchenko, E. V.; Talapin, D. V.; Kotov, N. A.; O'Brien, S.; Murray, C. B. Structural diversity in binary nanoparticle superlattices. *Nature* **2006**, *439*, 55–59.
128. Talapin, D. V.; Lee, J.-S.; Kovalenko, M. V.; Shevchenko, E. V. Prospects of Colloidal Nanocrystals for Electronic and Optoelectronic Applications. *Chem. Rev.* **2010**, *110*, 389–458.
129. Talapin, D. V.; Murray, C. B. PbSe nanocrystal solids for n- and p-channel thin film field-effect transistors. *Science* **2005**, *310*, 86–9.
130. Sun, S.; Murray, C. B. Synthesis of monodisperse cobalt nanocrystals and their assembly into magnetic superlattices. *J. Appl. Phys.* **1999**, *85*, 4325–4330.
131. Tang, J.; Kemp, K. W.; Hoogland, S.; Jeong, K. S.; Liu, H.; Levina, L.; Furukawa, M.; Wang, X.; Debnath, R.; Cha, D.; Chou, K. W.; Fischer, A.; Amasian, A.; Asbury, J. B.; Sargent, E. H. Colloidal-quantum-dot photovoltaics using atomic-ligand passivation. *Nat. Mater.* **2011**, *10*, 765–771.

132. Gur, I.; Fromer, N. a.; Geier, M. L.; Alivisatos, A. P. Air-stable all-inorganic nanocrystal solar cells processed from solution. *Science* **2005**, *310*, 462–466.
133. Ehrler, B.; Walker, B. J.; Böhm, M. L.; Wilson, M. W.; Vaynzof, Y.; Friend, R. H.; Greenham, N. C. In situ measurement of exciton energy in hybrid singlet-fission solar cells. *Nature Commun.* **2012**, *3*.
134. Kovalenko, M. V.; Spokoyny, B.; Lee, J. S.; Scheele, M.; Weber, A.; Perera, S.; Landry, D.; Talapin, D. V. Semiconductor nanocrystals functionalized with antimony telluride zintl ions for nanostructured thermoelectrics. *J. Am. Chem. Soc.* **2010**, *132*, 6686–6695.
135. Wang, R. Y.; Feser, J. P.; Lee, J. S.; Talapin, D. V.; Segalman, R.; Majumdar, A. Enhanced thermopower in PbSe nanocrystal quantum dot superlattices. *Nano Lett.* **2008**, *8*, 2283–2288.
136. Ko, D. K.; Murray, C. B. Probing the fermi energy level and the density of states distribution in PbTe nanocrystal (Quantum Dot) solids by temperature-dependent thermopower measurements. *ACS Nano* **2011**, *5*, 4810–4817.
137. Luedtke, W. D.; Landman, U. Structure, dynamics, and thermodynamics of passivated gold nanocrystallites and their assemblies. *J. Phys., Chem.* **1996**, *100*, 13323–13329.
138. Pohjolainen, E.; Chen, X.; Malola, S.; Groenhof, G.; Häkkinen, H. A unified AMBER-compatible molecular mechanics force field for thiolate-protected gold nanoclusters. *J. Chem. Theory Comput.* **2016**, *12*, 1342–1350.
139. Hasselman, D.; Johnson, L. F. Effective thermal conductivity of composites with interfacial thermal barrier resistance. *J. Compos. Mater* **1987**, *21*, 508–515.
140. Minnich, A.; Chen, G. Modified effective medium formulation for the thermal conductivity of nanocomposites. *Appl. Phys. Lett.* **2007**, *91*, 1–4.
141. Banerjee, S.; Montgomery, J. A.; Gascón, J. A. A QM/MM approach for the study of monolayer-protected gold clusters. *J. Mater Sci.* **2012**, *47*, 7686–7692.
142. Meyer, A.; Allinger, N. Conformational analysis—CX: Applications of the molecular mechanics method to organic halides. *Tetrahedron* **1978**, *31*, 1971 – 1978.
143. Johnson, R. A. Alloy models with the embedded-atom method. *Phys. Rev. B* **1989**, *39*, 12554.
144. Buffat, P.; Borel, J. P. Size effect on the melting temperature of gold particles. *Phys. Rev. A* **1976**, *13*, 2287–2298.